UNIVERSIDADE DE SÃO PAULO
ESCOLA DE ENGENHARIA DE SÃO CARLOS

Marlon Sproesser Mathias

Computational study of the hydrodynamic stability of gaps and cavities in a subsonic compressible boundary layer

São Carlos

2021

Marlon Sproesser Mathias

Estudo computacional da estabilidade hidrodinâmica de cavidades em uma camada limite compressível subsônica

Tese apresentada à Escola de Engenharia de São Carlos da Universidade de São Paulo, para obtenção do título de Doutor em Ciências - Programa de Pós-Graduação em Engenharia Mecânica.

Área de concentração: Aeronáutica

Supervisor: Prof. Dr. Marcello Augusto Faraco de Medeiros

VERSÃO CORRIGIDA

São Carlos

2021

AUTORIZO A REPRODUÇÃO TOTAL OU PARCIAL DESTE TRABALHO, POR QUALQUER MEIO CONVENCIONAL OU ELETRÔNICO, PARA FINS DE ESTUDO E PESQUISA, DESDE QUE CITADA A FONTE.

Ficha catalográfica elaborada pela Biblioteca Prof. Dr. Sérgio Rodrigues Fontes da EESC/USP com os dados inseridos pelo(a) autor(a).

Mathias, Marlon Sproesser
M431c Computational study of the hydrodynamic stability of gaps and cavities in a subsonic compressible boundary layer / Marlon Sproesser Mathias; orientador Marcello Augusto Faraco de Medeiros. São Carlos, 2021.

Tese (Doutorado) - Programa de Pós-Graduação em Engenharia Mecânica e Área de Concentração em Aeronáutica -- Escola de Engenharia de São Carlos da Universidade de São Paulo, 2021.

1. Gap. 2. Open Cavity. 3. Compressible flow. 4. Global stability. 5. Direct Numerical Simulation. 6. Wave packets. I. Título.

Eduardo Graziosi Silva - CRB - 8/8907

FOLHA DE JULGAMENTO

Candidato: Engenheiro **MARLON SPROESSER MATHIAS.**

Título da tese: "Estudo computacional da estabilidade hidrodinâmica de cavidades em uma camada limite compressível subsônica".

Data da defesa: 07/12/2021.

Comissão Julgadora	**Resultado**
Prof. Associado **Marcello Augusto Faraco de Medeiros** **(Orientador)** (Escola de Engenharia de São Carlos – EESC/USP)	**Approved**
Prof. Dr. **Vassilis Theofilis** (Aerospace Engineering/University of Liverpool)	**Approved**
Prof. Dr. **Ardeshir Hanifi** (KTH Royal Institute of Technology)	**Approved**
Prof. Titular **Gherhardt Ribatski** (Escola de Engenharia de São Carlos – EESC/USP)	**Approved**
Prof. Dr. **André Valdetaro Gomes Cavalieri** (Instituto Tecnológico de Aeronáutica/ITA)	**Approved**

Coordenador do Programa de Pós-Graduação em Engenharia Mecânica:
Prof. Associado **Adriano Almeida Gonçalves Siqueira**

Presidente da Comissão de Pós-Graduação:
Prof. Titular **Murilo Araujo Romero**

Acknowledgements

Gostaria de agradecer a todos que tornaram este trabalho possível e contribuíram em seu desenvolvimento, direta ou indiretamente.

À minha namorada e melhor amiga, Ana Carolina, que sempre me apoiou e esteve ao meu lado. À minha família, João Carlos, Sônia e Marcel, que me apoiaram nesta etapa e nas que a precederam.

Ao meu orientador, Marcello, pelas produtivas conversas e pela orientação que se iniciou com minha IC e continuou até este momento. Aos colegas de laboratório, Ana Elisa, Andrés, Christian, Daniel, Elmer, Fernando, Felipe, Filipe, Giovanni, Juan, Matheus, Pedro e Victor, pela companhia no desenvolvimento do trabalho e pelas conversas relacionadas, ou não, à pesquisa. Aos amigos da pós-graduação no Departamento de Engenharia Aeronáutica.

Ao professores Poti, Sávio e Vassilis, que deram valiosas dicas para a continuação da pesquisa.

À Fundação de Amparo à Pesquisa do Estado de São Paulo (FAPESP), pelo apoio financeiro por meio do projeto número 2018/04584-0. Além do Air Force Office of Scientific Research (AFOSR), projeto FA9550-18-1-0112; da University of Liverpool, pelo acesso ao Cluster Barkla; ao Centro de Ciências Matemáticas Aplicadas a Industria (CeMEAI-USP), pelo acesso ao Cluster Euler (FAPESP 2013/07375-0); e ao Laboratório Nacional de Computação Científica (LNCC), pelo acesso ao Supercomputador Santos Dumont.

E a todos os demais que, de alguma forma, contribuíram para este trabalho.

"Apesar de [redacted]
amanhã há de ser outro dia"
Chico Buarque

ABSTRACT

MATHIAS, M. S. **Computational study of the hydrodynamic stability of gaps and cavities in a subsonic compressible boundary layer**. 2021. 160p. Tese (Doutorado) - Escola de Engenharia de São Carlos, Universidade de São Paulo, São Carlos, 2021.

We study the effect of small cavities, or other discontinuities, on the laminar to turbulent flow transition over a flat plate. Understanding the transition mechanism is of significant importance for the reduction of drag in an aerodynamic project, which impacts the fuel consumption of aircrafts, for example. Predicting the correct region in which the transition to turbulence occurs is still a challenge, especially when accounting for parameters such as surface imperfections or manufacturing tolerances. Ideally, aircraft designers would balance the costs of manufacturing smoother surfaces with their aerodynamic benefits. We use two different computational tools in this work. First, a Direct Numerical Simulation (DNS) code is used to simulate the flow, either just by itself or in conjunction with controlled disturbances designed to model a natural transition. The second tool is a Linear Stability Theory (LST) code which can compute the linear stability modes of a given base flow, this algorithm is of the time-stepping type, for which we analyze the sources of errors and develop guidelines for obtaining optimum results. Both tools were designed to capture a wide spectrum of oscillations, even at very low amplitudes, which is essential for such modeling, as the natural transition is triggered by the interaction of multiple modes of different frequencies that are several orders of magnitude smaller than the base flow. There are many previous works that study either the natural transition on a flat plate or the flow disturbances caused by discontinuities on the surface, but the interaction between those two phenomena is still open for investigation. We study two different scenarios: when the cavity is much larger than the incoming boundary layer; and when they are of comparable magnitudes. Similar conclusions are reached in both cases. Increasing the Mach number has a mostly destabilizing effect on the 2D modes of the cavity. Greater ratios between cavity size and the incoming boundary layer thickness also increase the instability. We then compare the linear stability results to non-linear simulations. We also conclude that, even though 2D modes are usually more linearly unstable, the presence of 3D modes is essential for an accurate simulation of the flow. Moreover, we compare our results to experimental works and conclude that when both 2D and 3D modes are unstable in a small open cavity, it may cause a bypass transition in the boundary layer.

Keywords: Gap. Open Cavity. Compressible flow. Global stability. Direct Numerical Simulation. Wave packets.

RESUMO

MATHIAS, M. S. **Estudo computacional da estabilidade hidrodinâmica de cavidades em uma camada limite compressível subsônica**. 2021. 160p. Tese (Doutorado) - Escola de Engenharia de São Carlos, Universidade de São Paulo, São Carlos, 2021.

Estudamos o efeito de pequenas cavidades, ou outras descontinuidades, na transição de um escoamento do regime laminar para o turbulento sobre uma placa plana. Entender o mecanismo de transição para turbulência é de grande importância para a redução de arrasto em um projeto aerodinâmico, o que impacta, por exemplo, o consumo de combustível de um avião. Prever corretamente a região da transição para turbulência ainda é um desafio, especialmente ao considerar parâmetros como imperfeições da superfície ou tolerâncias de manufatura. Idealmente, os projetistas de um avião devem balancear os custos de fabricar superfícies mais lisas com seus benefícios. Duas ferramentas computacionais são usadas. Primeiro, um código de Simulação Numérica Direta (DNS) é usado para simular e escoamento, tanto sozinho quanto somado de perturbações criadas para simular a transição natural. A segunda ferramenta é um código de estabilidade linear (LST) que calcula os modos do escoamento, este algoritmo é do tipo time-stepping e analisamos suas fontes de erros e desenvolvemos diretrizes para obtenção resultados ótimos. Ambas as ferramentas foram projetadas para capturar um amplo espectro de oscilações, mesmo com amplitudes baixas, o que é essencial para tal modelagem pois a transição natural depende da interação de múltiplos modos com diferentes frequências e de amplitudes muitas ordens de grandeza menores que o escoamento. Existem muitos trabalhos anteriores que estudam a transição natural em uma placa plana ou os distúrbios causados por descontinuidades na superfície, mas a interação entre esses dois fenômenos ainda está aberta para investigação. Estudamos dois cenários diferentes: quando a cavidade é muito maior do que a camada limite; e quando são de magnitudes comparáveis, chegando a conclusões semelhantes. O aumento do número de Mach tem um efeito geralmente desestabilizador nos modos 2D da cavidade. Razões maiores entre o tamanho da cavidade e a espessura da camada limite também aumentam a instabilidade. Em seguida, comparamos os resultados de estabilidade linear com simulações não lineares. Também concluímos que, embora os modos 2D sejam geralmente mais linearmente instáveis, a presença de modos 3D é essencial para uma simulação precisa do escoamento. Por fim, comparamos nossos resultados com trabalhos experimentais e concluímos que quando modos 2D e 3D são instáveis em uma pequena cavidade aberta, ela pode causar uma transição de by-pass na camada limite.

Palavras-chave: Cavidade pequena. Cavidade aberta. Escoamento compressível. Estabilidade global. Direct Numerical Simulation. Pacotes de onda.

LIST OF FIGURES

Figure 1.1 – Illustration of the open cavity flow. 28

Figure 1.2 – Neutral stability curves for a $L/D = 2$ and $D/\delta^*_{LE} = 10.2$ open cavity as a function of Mach and Reynolds. 29

Figure 2.1 – The various regions of a boundary layer transition. 34

Figure 2.2 – Illustration of TS waves evolution before transition to turbulence. . . 35

Figure 2.3 – Typical routes from receptivity to turbulent breakdown. 36

Figure 2.4 – Schlieren image of the cavity flow showing its acoustic output. 37

Figure 2.5 – Cavity acoustic directivity at Mach 0.05 and Mach 0.1. 39

Figure 2.6 – Cavity acoustic directivity at Mach 0.1 for various frequencies. 39

Figure 2.7 – Effect of the gap on the transition location. 42

Figure 3.1 – Example of mesh generated using two attractor points at both ends of a cavity. 46

Figure 3.2 – Domain, mesh and boundary conditions of the flow simulation. The useful domain is marked in gray, while the buffer zone is green. One in every 10 nodes of the mesh is shown in black. The blue line represents wall boundaries, while the red line is a free-slip wall condition. 47

Figure 3.3 – Modified wave number for various numerical differentiation schemes. . 49

Figure 3.4 – Close-up of the corner nodes in the domain and the regions considered for derivatives. 51

Figure 3.5 – Spectral function for the tenth order low-pass filter. 55

Figure 3.6 – Scheme of a three-dimensional domain decomposed for a grid of 3x4 processes. 58

Figure 3.7 – Flowchart to obtain derivatives of the decomposed domain. 59

Figure 3.8 – Flowchart of the DNS. The top line of each frame identifies the task, while the bottom line shows which file contains it. 61

Figure 3.9 – Flowchart of the simulation routine of the DNS. The top line of each frame identifies the task, while the bottom line shows which file contains it. 62

Figure 3.10 – Speed-up obtained for different numbers of processors for our 2D and 3D test cases. 64

Figure 3.11 – Mesh spacing (top) and relative spacing change (bottom) for X (left) and Y (right) in a gap case. Buffer zones are represented by the dashed lines and are not fully shown for clarity. 66

Figure 3.12 – Time series of stream-wise velocity (U) at three probes as the domain evolves from the initial condition towards a base flow for three different SFD strategies: only at the buffer zones (blue), at the buffer zones and at the gap trailing edge (red) and at the whole domain (yellow). Note that the time scale is changed after $t = 2000$ for better visualization of the initial transient phase. 68
Figure 3.13 – Maximum residual of each variable towards a base flow. 69
Figure 4.1 – (Top) Number of Arnoldi iterations (M) and total integration time (τM) as a function of integration time τ for two values of C. (Bottom) Fraction of time spent in each part of the procedure. 79
Figure 4.2 – (Top) Streamwise velocity of the base flow (contours every 10% of the free-flow, from -30% to 90%) and velocity field inside the cavity. (Bottom) Maximum residue of each variable as the flow evolves to the steady state. 81
Figure 4.3 – (Left) Eigenspectrum of the base flow, with the unstable Rossiter modes (Rn) and the least stable stationary mode (S1) indicated, (Right) Density contours for the Rossiter modes 1 to 3 and the Stationary mode 1. 82
Figure 4.4 – Real part of the R2 eigenvalue as a function of ε for different values of τ. Dashed lines represent first-order accurate Fréchet derivative, and full lines, second-order accurate. (Left) Absolute value. (Right) Difference to the reference case. 83
Figure 4.5 – Real part of the S1 eigenvalue as a function of ε for different values of τ. Dashed lines represent first-order accurate Fréchet derivative, and full lines, second-order accurate. (Left) Absolute value. (Right) Difference to the reference case. 84
Figure 4.6 – Values of ε_{opt} and the corresponding E_B as a function of ε_S and N for 1st, 2nd and 4th order accuracy Fréchet approximations. 86
Figure 4.7 – (Left) Lower limit for τ according to equation 4.21. The dashed line represents the product $\tau M = 2500$, which was used in this work. (Right) Upper limit for τ according to equation 4.22. 88
Figure 4.8 – Real part of the R2 eigenvalue as a function of τ for selected values of ε. Dashed lines represent the first-order accurate Fréchet derivative, while full lines represent the second-order accurate derivative. (Left) Absolute value. (Right) Difference to the reference case. 89
Figure 4.9 – Real part of the S1 eigenvalue as a function of τ for selected values of ε. Dashed lines represent the first-order accurate Fréchet derivative, while full lines represent the second-order accurate derivative. (Left) Absolute value. (Right) Difference to the reference case. 89

Figure 4.10 – (Left) Evolution of each mode in the flow as it is simulated starting from the base flow without the introduction of any disturbance other than the discretization error. Modes R1 to R3 and S1 are highlighted. Solution projections on the 100th least stable are shown as thin gray lines. (Right) Snapshots of the density fluctuation at $\tau = 5$, 10, and 20. 90

Figure 4.11 – Evolution of each mode in the flow as it is simulated from different starting conditions. Modes R1 to R3 and S1 are highlighted. Modes up to the 100th least stable are shown as thin gray lines. Vertical lines depict the upper limits of τ, as given by equation 4.24. 91

Figure 4.12 – Estimate of the error in $A\zeta$ as a function of τ for select values of ε, (Left) using equation 4.29 and (Right) using equation 4.30 with values corresponding to mode S1. The solid lines represent second order accurate Fréchet derivative approximation and the dashed lines, first order approximation. 93

Figure 4.13 – (Left) Values of E_A for mode R2 when the real part of its eigenvalue is changed. (Center) Values of E_A for mode S1 when the real part of the leading eigenvalue is changed. (Right) Values of E_A for mode S1 when the real part of its eigenvalue is changed. 94

Figure 4.14 – Estimate of the error in $A\zeta$ as a function of τ for select values of ε, using equation 4.30 for modes R2 (Left) and S1 (Right). The solid lines represent the case with renormalization and dashed lines, without. 95

Figure 4.15 – Difference in the real part of the eigenvalue corresponding to modes R2 (Left) and S1 (Right) as a function of τ for $\varepsilon = 10^{-7}$ and second order accurate Fréchet derivative. The black line is the reference case, with no renormalization and the colored lines represent different intervals of renormalization. 96

Figure 4.16 – Estimate of the error in $A\zeta$ as a function of τ for select values of ε, using equation 4.30 for a hypothetical flow with the least stable eigenvalues given by $\sigma_1 = -0.1$, $\sigma_2 = -0.12$, $\sigma_1 = -0.2$. The solid lines represent the case with renormalization and dashed lines, without. 96

Figure 4.17 – Isocontours of $\log_{10}$(Error) of the real part of the R2 mode, using $\varepsilon = 10^{-6}$. The full gray lines represent a constant computational cost of 5 minutes, 10 minutes, 30 minutes and 1 hour from left to right. The dashed gray lines indicate constant $t = \tau M$. (Left) First order accurate Fréchet derivative. (Right) Second order accurate Fréchet derivative. 98

Figure 4.18 – Isocontours of $\log_{10}$(Error) of the real part of the S1 mode, using $\varepsilon = 10^{-6}$. The full gray lines represent a constant computational cost of 5 minutes, 10 minutes, 30 minutes and 1 hour from left to right. The dashed gray lines indicate constant $t = \tau M$. (Left) First order accurate Fréchet derivative. (Right) Second order accurate Fréchet derivative. 98
Figure 4.19 – Error of the first four eigenvalues as computational time is increased. $\tau = 0.1, 1, 10$, $\varepsilon = 10^{-6}$. Note that the time scale for mode S1 is different than that of modes R1 to R3. 100
Figure 4.20 – Isocontours of $\log_{10}$(Error) of the eigenfunction of R2 for (Left) first-order accurate Fréchet derivative and (Right) second-order derivative. 101
Figure 4.21 – Isocontours of $\log_{10}$(Error) of the eigenfunction of S1 for (Left) first-order accurate Fréchet derivative and (Right) second-order derivative. 101
Figure 4.22 – Weight of each disturbance ζ_i in the eigenfunctions of modes R1, R2, R3 and S1. 102
Figure 5.1 – Eigenfunctions of Rossiter mode linear approximations at $Re_D = 1000$, $D/\theta = 100$ and $Ma = 0.5$, at an arbitrary phase. (Left) Contours of pressure for mode 2. Black lines indicated level zero. (Right) Contours of wall-normal velocity for modes 1 to 5. 107
Figure 5.2 – Eigenvalues from the D/θ ratio sweep ($Re_D = 1000$, $Ma = 0.5$). (Left) Eigenspectrum. (Right) Real and imaginary parts of Rossiter mode eigenvalues. 107
Figure 5.3 – Mixing layer integrated spatial amplification factor compared to the global instability results. The asterisks indicate the global modes eigenvalues of Rossiter modes and the dots are other eigenvalues, they refer to the scale on the right-hand side of the frame. 108
Figure 5.4 – Eigenvalues from the first Mach number sweep ($Re_D = 1149$, $D/\theta = 29.7$). (Left) Eigenspectrum. (Right) Real and imaginary parts of Rossiter mode eigenvalues. 110
Figure 5.5 – Eigenvalues from the second Mach number sweep ($Re_D = 1000$, $D/\theta = 100$). (Left) Eigenspectrum. (Right) Real and imaginary parts of Rossiter mode eigenvalues. 110
Figure 5.6 – Location of probes for the analysis of sound emission. Gray contours indicate dilatation fluctuations of the second Rossiter mode at $Ma = 0.6$, full line for positive contours and dashed line for negative ones. Colored contours indicate vorticity fluctuations. The black line indicates region of evaluation of sound source magnitude. Red and green lines indicate regions of evaluation of the magnitude of the pressure fluctuations. 111

Figure 5.7 – Acoustic energy transfer (ET_{AC}) as a function of Mach number for the linear approximation of Rossiter modes 1 (blue) and 2 (red). The dashed and dashed-dotted lines represent Ma^3 and Ma^2 respectively. 112

Figure 5.8 – Frequency predictions of Rossiter modes (blue) and standing wave modes (orange) compared to the global mode results (circles). The circle radius is proportional to the distance from neutral stability, the solid circles represent instability while hollow circles represent stability. 113

Figure 5.9 – Eigenvalues from the span-wise wave number sweep ($Re_D = 1000$, $D/\theta = 100$, $L/D = 2$, $Ma = 0.5$). (Left) Spectra in the complex plane. (Right) Real and imaginary parts of the eigenvalues of the Rossiter and centrifugal modes. 114

Figure 5.10 – Most unstable eigenmodes from the 3D LST analysis. (Left) $\beta = \pi/4$, isosurfaces of density. (Right) $\beta = 2\pi$, isosurfaces of span-wise velocity. 115

Figure 5.11 – Comparison between 2D and 3D simulations of the $Re_D = 1000$, $D/\theta = 100$, $L/D = 2$, $Ma = 0.5$ case. (Left) Time series of pressure at the trailing edge. (Right) Spectrum. The vertical lines mark angular velocities predicted by the linear stability analysis for each Rossiter mode (R1 through R3) and centrifugal mode (C2 and C3). 116

Figure 5.12 – Most unstable mode at each β for the first three cases defined in table 5.1. Each colored region represents a different type of mode. . . 117

Figure 5.13 – Time series of pressure fluctuation for the cases defined in table 5.1. Blue and orange curves represent different span-wise positions. 118

Figure 5.14 – Spectra of cases `R`, `C` and `R+C 1`. The linear predictions of angular velocities of each mode are also marked. 118

Figure 5.15 – Most unstable linear mode for cases `R+C 1`, `R+C 2` and `R+C 3` for various values of β. 119

Figure 5.16 – Comparison between 2D and 3D simulations of case `R+C 3` ($Re_D = 1500$, $D/\theta = 100$, $L/D = 2$, $Ma = 0.5$). (Left) Time series of pressure at the trailing edge. The dashed lines were measured at another span-wise position. (Right) Spectrum. The vertical lines mark angular velocities predicted by the linear stability analysis for each Rossiter mode (R1 through R3). 119

Figure 5.17 – Snapshots of wall-normal velocity for the 2D simulation of cases `R+C 2` and `R+C 3` and the 3D simulation of case `R+C 3`. The snapshots of the 3D simulation were taken at an arbitrary span-wise position. . . . 120

Figure 5.18 – (Top) Velocity profiles of the mean flow. (Middle) Mixing layer thickness for different situations of case `R+C 3` (Bottom) Total spatial amplification of each mixing layer as a function of ω. 121

Figure 5.19 – Spectrum of pressure at the trailing edge as a function of time for case `R+C 3` ($Re_D = 1500$, $D/\theta = 100$, $L/D = 2$, $Ma = 0.5$) for (Left) the 2D simulation, (Center) the 3D simulation and (Right) the filtered 3D simulation. LST-predicted frequencies for Rossiter modes are also shown. 122

Figure 5.20 – Spectrum of wall-normal velocity inside the cavity as a function of time for case `R+C 3` ($Re_D = 1500$, $D/\theta = 100$, $L/D = 2$, $Ma = 0.5$) for (Left) the 2D simulation, (Center) the 3D simulation and (Right) the filtered 3D simulation. LST-predicted frequencies for Rossiter modes are also shown. 122

Figure 5.21 – Comparison between 2D and 3D simulations of case `R+C 3` ($Re_D = 1500$, $D/\theta = 100$, $L/D = 2$, $Ma = 0.5$). (Left) Time series of wall-normal velocity in the cavity. The dashed lines were measured at another span-wise position. (Right) Spectrum. The vertical lines mark angular velocities predicted by the linear stability analysis for each Rossiter mode (R1 through R3). 123

Figure 5.22 – Temporal and span-wise spectrum for the limit cycle of `R+C 3` ($Re_D = 1500$, $D/\theta = 100$, $L/D = 2$, $Ma = 0.5$). (Left) Pressure at the cavity trailing edge (Right) Wall-normal velocity inside the cavity. 124

Figure 5.23 – Spectrum of (Left) pressure and (Right) velocity of case `R+C 3` ($Re_D = 1500$, $D/\theta = 100$, $L/D = 2$, $Ma = 0.5$), beginning with the 2D limit cycle, then with 3D effects turned on and off at $t = 0$ and $t = 250$, respectively. Expected frequencies for Rossiter modes are also shown. 124

Figure 5.24 – Spectrum of (Top) pressure at the trailing edge and (Bottom) wall-normal velocity inside the cavity as a function of time for case `R+C 3` ($Re_D = 1500$, $D/\theta = 100$, $L/D = 2$, $Ma = 0.5$) for various span-wise domain lengths. Expected frequencies for Rossiter modes are also shown. 125

Figure 5.25 – Comparison between 2D and 3D simulations of case `R+C 2` ($Re_D = 1000$, $D/\theta = 100$, $L/D = 2$, $Ma = 0.5$). (Left) Time series of wall-normal velocity inside the cavity. The dashed lines were measured at another span-wise position. (Right) Spectrum. The vertical lines mark angular velocities predicted by the linear stability analysis for each Rossiter mode (R1 through R3) and centrifugal mode (C2 and C3). 126

Figure 5.26 – Spectrum of wall-normal velocity inside the cavity as a function of time for case `R+C 2` ($Re_D = 1000$, $D/\theta = 100$, $L/D = 2$, $Ma = 0.5$) for (Left) the 2D simulation, (Center) the 3D simulation and (Right) the filtered 3D simulation. Expected frequencies for Rossiter modes are also shown. 126

Figure 5.27 – Temporal and span-wise spectrum for the limit cycle of R+C 2 ($Re_D = 1000$, $D/\theta = 100$, $L/D = 2$, $Ma = 0.5$). (Left) Pressure at the cavity trailing edge (Right) Wall-normal velocity inside the cavity. 127
Figure 6.1 – Mesh for the gap simulation with $Re_{\delta_0^*} = 600$, $L/\delta_0^* = 10$, $D/\delta_0^* = 5$, $Ma = 0.5$. 132
Figure 6.2 – Baseflow at the gap for $Re_{\delta_0^*} = 600$, $L/\delta_0^* = 10$, $D/\delta_0^* = 5$, $Ma = 0.5$. Each contour represents 20% of the free-flow velocity. 132
Figure 6.3 – Global stability results for $Re_{\delta_0^*} = 600$, $L/\delta_0^* = 10$, $D/\delta_0^* = 5$, $Ma = 0.5$. (Left) Eigenvalues map with the first Rossiter mode highlighted. (Right) Real part of the eigenfunctions of the first Rossiter mode: (Top) Stream-wise velocity and (Bottom) Density. 133
Figure 6.4 – Eigenvalues obtained with the regular mesh compared to those obtained with the refined mesh. 133
Figure 6.5 – Eigenfunction of stream-wise velocity of the mode at $\sigma = -0.0175 \pm 0.155i$. 134
Figure 6.6 – Eigenvalues obtained with various values of χ in the SFD filter. . . . 135
Figure 6.7 – Boundary layer displacement and momentum thickness with and without the gap for the following parameters: $Re_{\delta_0^*} = 600$, $L = 10$, $D = 5$, $Ma = 0.5$ 136
Figure 6.8 – (Left) Temporal evolution of the wave packet with and without the gap. (Right) Spectrum of the wave packet at each probe. 136
Figure 6.9 – Density (Top) and stream-wise velocity (Bottom) fluctuations at times $t = 250$ (Left) and $t = 500$ (Right). Red and blue areas represent positive and negative oscillations of the flow, respectively. Black and white lines represent the positive and negative oscillations predicted by the global stability analysis, note that the phase and levels were shifted to match the flow's. 137
Figure 6.10 – (Left) Effect of the Mach number on the eigenmodes. (Right) Effect of gap length on the eigenmodes. 139
Figure 6.11 – Amplification rate of the leading mode for the parameters $L = 10$, $D = 5$, $Ma = 0.5$ and $Re_{\delta_0^*} = 400$, 600, 1000 at various span-wise wave numbers 139
Figure 6.12 – Centrifugal modes I, II and III for $Re_{\delta_0^*} = 1000$, $L = 10$, $D = 5$ and $Ma = 0.5$. $\beta = 3/4\pi$, $\pi/2$ and $\pi/4$, respectively. (Left) Stream-wise velocity. (Right) Span-wise velocity. 140
Figure 6.13 – Types of instabilities found for various combinations of gap length and depth, at $Re_{\delta_0^*} = 600$ and $Ma = 0.5$. The numbers beside the markers indicate which types of unstable centrifugal modes were found, in decreasing order of amplification rate. 141

Figure 6.14 – Isosurfaces of (Left) stream-wise and (Right) span-wise velocity fluctuations at two different times (Top and Bottom) for the $Re_{\delta_0^*}$, $L = 10$, $D = 5$ and $Ma = 0.5$ case. Only a quarter of the span-wise domain is shown for clarity. 142
Figure 6.15 – (Top) Temporal series of pressure at the trailing edge of the gap at two different span-wise positions, at opposite phases for the $Re_{\delta_0^*}$, $L = 10$, $D = 5$ and $Ma = 0.5$ case. (Bottom) Spectrum of the limit cycle. . . 143
Figure 6.16 – Temporal and span-wise spectrum for the limit cycle of the $Re_{\delta_0^*}$, $L = 10$, $D = 5$ and $Ma = 0.5$ case. 143
Figure 6.17 – Boundary layer displacement and momentum thickness of the base flow and of the limit cycle $Re_{\delta_0^*} = 600$, $L = 10$, $D = 5$, $Ma = 0.5$ . . . 144

LIST OF TABLES

Table 3.1 – DNS execution time for different numbers of parallel processes, two-dimensional case. 63
Table 3.2 – DNS execution time for different numbers of parallel processes, three-dimensional case. 64
Table 4.1 – Estimated coefficients of computational cost, in seconds 78
Table 5.1 – Cases defined to investigate the interaction of Rossiter and centrifugal modes 117

LIST OF SYMBOLS

L	Cavity length
D	Cavity depth
Re	Reynolds number
Ma	Mach number
δ^*	Boundary layer displacement thickness
θ	Boundary layer momentum thickness
t	Time
x	Stream-wise direction
y	Wall-normal direction
z	Span-wise direction
u	Stream-wise velocity component
v	Wall-normal velocity component
w	Span-wise velocity component
ρ	Fluid density
e	Fluid internal energy
p	Fluid pressure
$\boldsymbol{U_0}$	Base flow
$\boldsymbol{u}$	Flow disturbance
σ	Eigenvalue of a flow mode ($\sigma = \sigma_r + i\sigma_i$)
σ_r	Temporal growth of a flow mode
σ_i	Angular velocity a flow mode
ω	Angular velocity
β	Span-wise wavenumber

CONTENTS

1 INTRODUCTION 27

1.1 Motivation 27

1.2 Problem description 28

1.3 Objectives 30

1.4 Summary of this work 30

2 REVIEW 33

2.1 Flow instability 33

2.2 Cavity instability 36

2.2.1 Motivation 36

2.2.2 Cavity instability and acoustic modes 37

2.2.3 Gaps 40

3 DIRECT NUMERICAL SIMULATION 43

3.1 Numerical methods 44

3.1.1 Governing equations 44

3.1.2 Meshing and domain 45

3.1.3 Boundary and initial conditions 46

3.1.4 Spatial derivatives 47

3.1.5 Time integration 52

3.1.6 Anti-aliasing filtering 53

3.1.7 Artificial damping 54

3.2 Implementation 57

3.2.1 Domain decomposition and parallel execution 58

3.2.2 Linear system solver 59

3.2.3 Flowchart 60

3.3 Performance 63

3.4 Strategies for mesh generation 65

3.5 Obtaining a base flow 66

4 LINEAR STABILITY THEORY 71

4.1 Introduction 71

4.2 Methods 73

4.2.1 Linear stability computations 73

4.2.2 Initial disturbance 77

4.2.3 Computational cost 77

4.3 Baseline results of the studied case . . . 80
4.4 Order of accuracy of the Fréchet derivative and disturbance magnitude . . . 82
4.5 Effect of integration time length . . . 87
4.6 Krylov span dimension and optimization of the total computational time . . . 96
4.7 Rate of convergence of eigenfunctions and eigenvalues . . . 100
4.8 Conclusion . . . 102

5 LARGE OPEN CAVITIES . . . 105
5.1 Introduction . . . 105
5.2 Two-dimensional results . . . 106
5.2.1 Influence of the boundary layer thickness . . . 106
5.2.2 Influence of the Mach number . . . 109
5.3 Three-dimensional global stability . . . 114
5.4 Non-linear effects . . . 115
5.5 Conclusion . . . 128

6 EFFECTS OF GAPS ON BOUNDARY LAYER TRANSITION . . . 131
6.1 Introduction . . . 131
6.2 Mesh and domain independence . . . 131
6.2.1 Mesh independence . . . 133
6.2.2 Domain independence . . . 134
6.3 Effects of the gap on the boundary layer thickness and spatial stability . . . 135
6.4 Two-dimensional global stability . . . 138
6.5 Three-dimensional global stability . . . 139
6.6 Direct Numerical Simulation of three-dimensional modes . . . 142
6.7 Conclusion . . . 144

7 DISCUSSION AND FINAL REMARKS . . . 147
7.1 Direct Numerical Simulation . . . 147
7.2 Linear Stability Analysis . . . 147
7.3 Cavities . . . 148
7.4 Gaps . . . 149
7.5 Suggestion for future works . . . 149

BIBLIOGRAPHY . . . 151

Chapter 1

Introduction

1.1 Motivation

In the aeronautical industry, a good prediction of the turbulent transition location is of significant importance as it affects the aircraft drag and therefore, its fuel consumption. This effect is both direct, due to the increased surface friction of turbulent flows, and indirect, due to changes in the pressure field.

Reneaux (2004) estimates that fuel corresponds to about 22% of the operational cost of an airline and that a 1% reduction in drag would correspond to increasing the payload of an Airbus A320-sized aircraft in about 1.6 ton or 10 passengers. However, current drag prediction methods may err with margins higher than 1%. For instance, Tinoco et al. (2018) summarize the data from the Sixth AIAA CFD Drag Prediction Workshop, in which eighteen participant groups used state-of-the-art CFD codes to predict drag for a standard transonic aircraft model, their results fall within a 10 Drag Counts margin, corresponding to about 4% of the total drag of the reference model.

Taking an Airbus A320 as reference, Marec (2001) concludes that the friction drag is around 50% of the total drag, of which 25% comes from the wings. If the laminar flow region can be increased, it will directly reduce those numbers, especially in longer routes.

The flow on a real surface is subject to its imperfections, which may affect its stability and change the location of the transition from laminar to turbulent. A robust model of the turbulent transition - including the effects of small surface imperfections such as rivets, panel junctions, dents or even dust - may aid designers in creating new and more efficient aerodynamic solutions.

These figures show that improvement in this area would be greatly beneficial for the industry and that better transition predictions would positively impact both fuel

consumption and operational costs.

The use of Natural Laminar Flow designs, or NLF, requires lower tolerances in manufacturing in both surfaces' shapes and junctions. The lack of better models for the effect of such imperfections leads designer to overshoot tolerances, which impacts costs of manufacturing and maintenance. Improving turbulent transition models would allow designers to reduce this kind of overhead.

1.2 Problem description

Figure 1.1 illustrates a flat plate with a cavity. There is a uniform flow coming from the left-hand side, a boundary layer is formed on the flat plate and there is a rectangular cavity in this plate after a certain distance. The geometry is considered uniform and infinite in the span-wise direction, as is the downstream to the cavity.

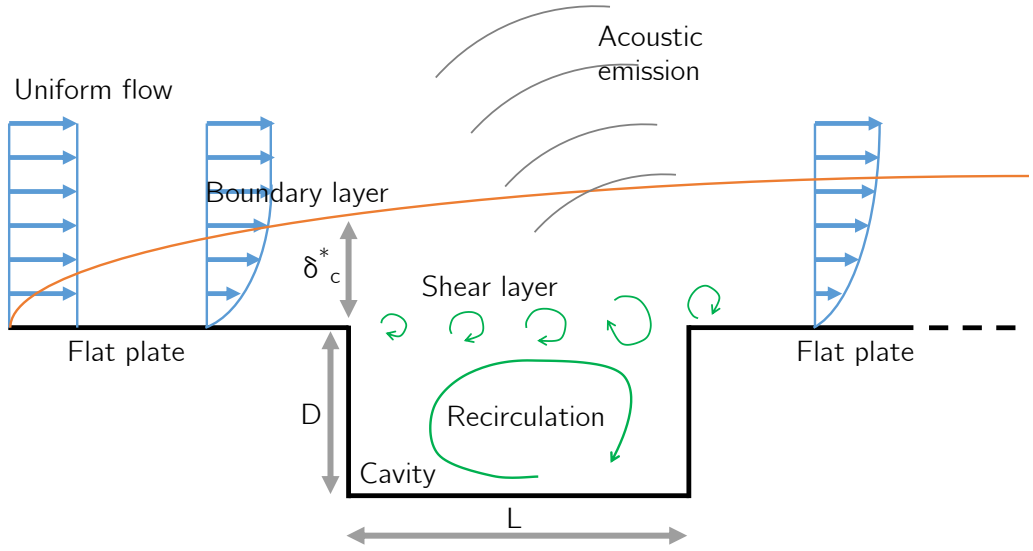

Figure 1.1 – Illustration of the open cavity flow.

All values in this study are non-dimensional and the parameters to be chosen are:

- L/D - Cavity aspect ratio (length by depth)
- δ^*_{LE} - Boundary layer displacement thickness at the cavity leading edge
- Re - Reynolds number
- Ma - Mach number

Depending on these parameters, the flow might be either stable or unstable. A stable flow will develop into a permanent regime, while an unstable flow will develop into an oscillating regime.

Figure 1.2 brings a diagram with neutral stability curves by Brès and Colonius (2008) for a fixed cavity aspect ratio of $L/D = 2$ and a boundary layer thickness given by $D/\delta^*_{LE} = 10.2$. At low Mach numbers, increasing the Reynolds number triggers three-dimensional instabilities, while two-dimensional instabilities tend to appear first if the Mach number is higher. For this length to depth ratio, flows above a Re_D of roughly 1300 are 3D unstable. The minimum Re for a 2D unstable flow is reduced as the Mach number increases, becoming lower than the 3D instability threshold above around Mach 0.4. These disturbances eventually saturate to become large oscillations in the flow. Some of their runs are indicated in this diagram. Two types of unstable modes may be present in an open cavity: Rossiter modes, which are essentially two-dimensional and centrifugal modes, which are three-dimensional.

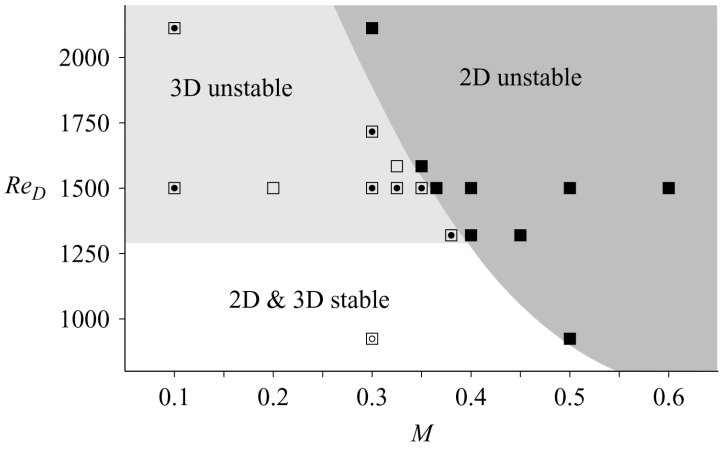

Figure 1.2 – Neutral stability curves for a $L/D = 2$ and $D/\delta^*_{LE} = 10.2$ open cavity as a function of Mach and Reynolds. The symbols indicate results by Brès and Colonius (2008), filled markers indicated unstable cases, squares for two-dimensional and circles for three-dimensional. (BRÈS; COLONIUS, 2008)

In stable scenarios, a steady flow is reached. In these cases, a known disturbance may be added upstream of the cavity so that we can measure its influence on the spatial instability of the boundary layer.

A computational model of this geometry is created and used to study the flow stability. Both two and three-dimensional cases are considered. The simulation is always compressible, even at low Mach numbers. In a three-dimensional case, the flow is periodic in the span-wise direction.

Two types of cavities are investigated in this work. First, we simulate larger cavities so that the types of modes present can be better understood. The instability modes of large cavities are mostly independent on those of the boundary layer. Nonetheless, the thickness of the incoming boundary layer plays a key role in determining the instability of the cavity.

Later, we studied small cavities, also called gaps, with depths no more than one order of magnitude larger than the boundary layer displacement thickness. In the case of gaps, their instability modes may interact with those of the boundary layer. In some cases, incoming TS waves may be amplified by the gap, even if the gap itself is globally stable, which would cause the transition to happen earlier. Unstable gaps may function as a source of disturbances for the downstream boundary layer or even cause a by-pass transition, depending on the type of oscillations.

It was found that both large cavities and gaps are subject to the same types of instability modes, which justifies them being studied together.

1.3 Objectives

The general objective of this work is to investigate the instability of open cavities and gaps in a boundary layer. More specifically, we wish to clarify the following points:

- How does each parameter affect the linear stability of an open cavity?
- What is the underlying physics of the effect of each parameter on the instability?
- To which extent can the linear analysis predict the non-linear regime?
- What are the effects of a gap on the instability of the boundary layer?

Moreover, due to the extensive use of a Linear Stability Theory calculation procedure to obtain the global modes of the flow, we also worked on optimizing the use of this technique so that it can be used more quickly and reliably.

1.4 Summary of this work

After this introduction and the bibliographic review in Chapter 2, we present the flow solver used in this work in Chapter 3, which is of the Direct Numerical Solver (DNS) kind. It brings details on its underlying numerical methods and their implementation, as well as code performance data and strategies for the generation of efficient meshes and techniques for accelerating the convergence towards a base flow. An entirely new DNS code was developed for this study, albeit based on previous experience in the group.

The Linear Stability Theory (LST) algorithm used in this work is shown in Chapter 4, which also brings a detailed study on the accuracy of such implementation and on the optimization of computational parameters used in the method. This development constitutes a contribution of this work.

Chapter 5 explores the physics of open cavity flows, using both DNS and LST codes. These flows are defined by a large ratio between the cavity dimensions and the thickness of the incoming boundary layer. Similarly, Chapter 6 explores the physics of boundary layers over gaps, which are small cavities, close in size to the boundary layer thickness, and that can impact the transition to turbulence either by amplifying TS waves or by causing a by-pass transition.

Chapter 7 summarizes the conclusions and suggests further research topics in this theme.

Chapter 2

Review

2.1 Flow instability

Flow transition from laminar to turbulent regimes has been largely studied for the past century. Despite great advances in these last decades, it remains an open problem.

Among the first studies for this phenomenon, Osbourne Reynolds' work stands out. His first publication in this matter (REYNOLDS, 1883) classifies two types of flow: "Direct" and "Sinuous", referring to both the flow surface and the shape of a colored marker he would add to the water. His following publication (REYNOLDS, 1894) brought a new, non-dimensional parameter that relates to the transition location, accounting for the flow velocity, the fluid's viscosity and a characteristic length, taken as the tube diameter. This would later be known as the Reynolds number.

Prandtl (1904) brought the concept of the boundary layer above a flat plate, already mentioning the phenomenon of transition from laminar to turbulent flow and boundary layer separation. His students continued his work, Walter Tollmien and Hermann Schlichting were among them. (SCHLICHTING; GERSTEN, 2000)

Earlier, Rayleigh (1879) studied the stability of a parallel, inviscid flow, concluding that a necessary condition for instability was the existence of an inflection point in the velocity profile. Orr (1909) and Sommerfeld (1908) derived the equation used to determine the stability modes of a parallel, viscous flow. It would, later, be known as the Orr-Sommerfeld equation. Tietjens (1925) has investigated the transition in a boundary layer, concluding the viscosity would play a destabilizing role.

Tollmien (1929) (translated in (TOLLMIEN, 1932)) and Schlichting (1933) have studied the effects of a small perturbation in a Blasius profile by modeling them as waves that are attenuated or amplified, depending on the flow stability, known today as the

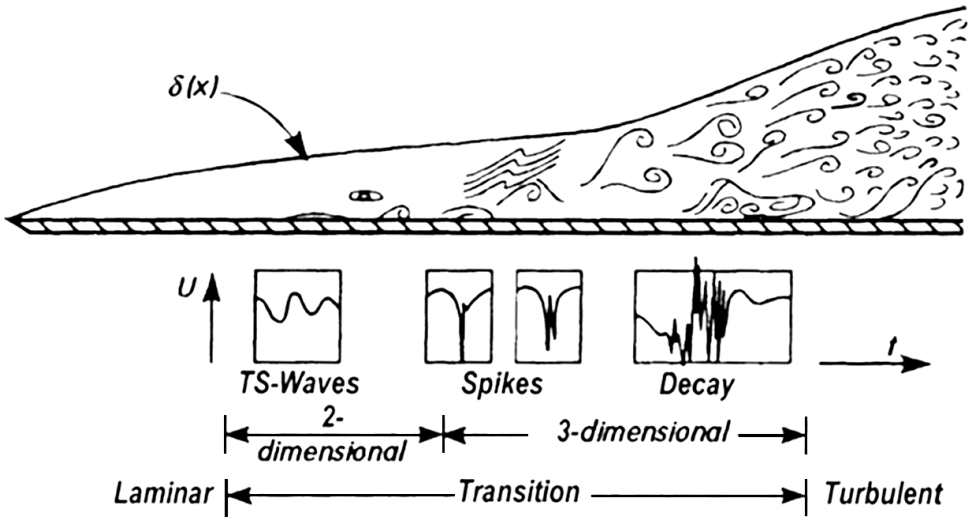

Figure 2.1 – The various regions of a boundary layer transition. (SCHLICHTING; GERSTEN, 2000)

Tollmien-Schlichting (TS) waves. In summary, Tollmien has drawn the critical stability curve in the Reynolds number versus wave number plane; and Schlichting has computed the amplification levels in this plane.

For the next decade, this theory could not be reproduced due to the high turbulence in the wind tunnels of the time. Finally, Schubauer and Skramstad (1947) were able to use a low turbulence wind tunnel and successfully observe the amplification of periodic waves just upwind of the transitional region in a boundary layer, soon followed by Liepmann (1943). These observations matched Tollmien and Schlichting's theory.

Schubauer and Skramstad (1947) used a vibrating ribbon in the boundary layer to generate controlled TS waves and observed the spatial evolution of their amplitude, as illustrated in Fig. 2.2. This image also shows the stability diagram from the Orr-Sommerfeld equation.

Gaster (1962) has connected the effects of temporal disturbance growth, which could be predicted theoretically, to the spatial growth, observed experimentally, later proposing the solution of the Orr-Sommerfeld equations for spatial modes (GASTER, 1965).

Ingen (1956) has proposed a method to predict the transition location from the disturbance amplification rates, known as the e^n method. Its idea is to integrate the amplification rate through the boundary layer and to assume transition happens when this integral reaches a certain threshold, represented by the constant e^n. Usually, $e = 9$ is taken as an average value, in flight, greater values may be used.

In either simulations or experiments, an initial disturbance is needed to trigger the transition process. It is either given by ambient noise, which cannot be controlled,

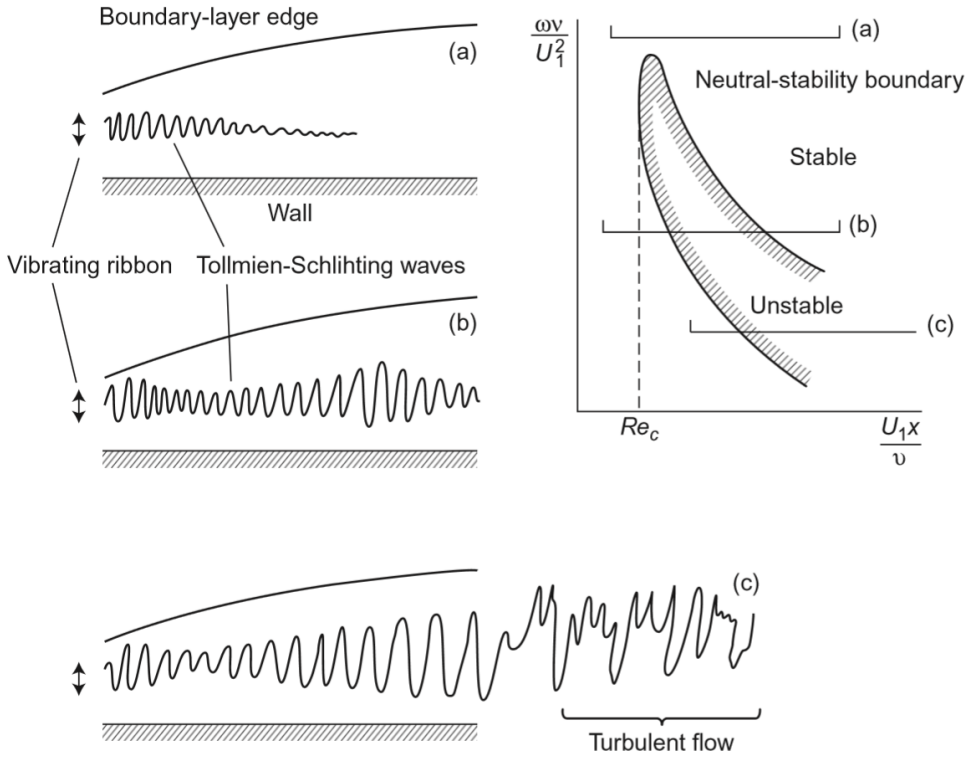

Figure 2.2 – Illustration of TS waves evolution before transition to turbulence. (HOUGHTON et al., 2012)

or by artificially introducing waves to the flow. In those studies that introduce a known wave, usually only a small number of distinct frequencies are present in the signal. In a natural transition, a broad range of frequencies are present in the spectrum. One way of replication this phenomenon is to use wave packets, which have a temporally short wave form with a broad spectrum (MARTINEZ; MEDEIROS, 2016; MARTINEZ, 2016).

Figure 2.3 (MORKOVIN; RESHOTKO; HERBERT, 1994) brings the typical routes of a natural transition, from the receptivity to the turbulent breakdown.

Typically, in a flat plate, routes "a" or "b" are taken, such as what is shown in Fig. 2.1. If large enough disturbances are given, a bypass transition might happen. A cavity with temporally unstable modes may lead to a bypass transition.

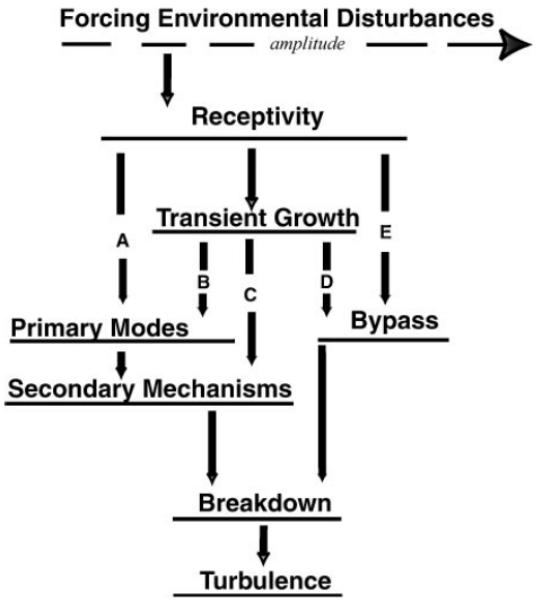

Figure 2.3 – Typical routes from receptivity to turbulent breakdown. (MORKOVIN; RESHOTKO; HERBERT, 1994)

2.2 Cavity instability

2.2.1 Motivation

Initially, open cavity research was motivated by their vibration modes, with special attention given to the frequencies. The concern was whether or not there would be oscillatory modes and what would their frequencies be, as these oscillations could excite modes in the structure, speeding up fatigue. To a smaller extent, there was also some concern on the increased drag caused by the oscillations and in their acoustic emissions. (OWEN, 1958).

Krishnamurty (1956), motivated by the buffeting observed in aircraft cavities such as open cockpits or landing gear doors, performed an experimental campaign and concluded that the minimum cavity size that generates sound is reduced as the Mach number increases and that this size is inversely proportional to the sound frequency observed. He has also reported that sound intensity grows quickly with the Mach number, roughly at its eighth power, as predicted by the existing theories. Acoustic waves were also visualized by Schlieren photography, qualitatively showing the sound directivity, as shown in Fig. 2.4.

At the same time, Roshko (1955) performed experiments to generate more data on open cavity flow and to observe its structures, also looking to understand the relevance of the cavity aspect ratio. His work is focused on the mean flow over the cavity, not on the

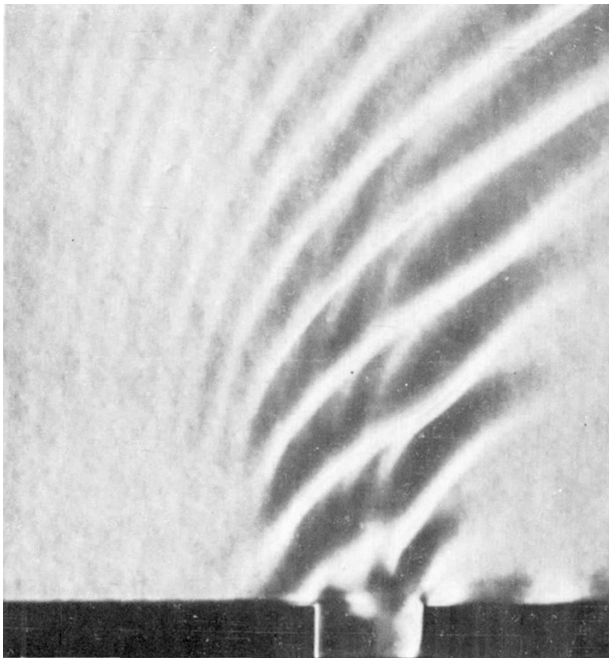

Figure 2.4 – Schlieren image of the cavity flow showing its acoustic output. (KRISHNAMURTY, 1956)

oscillations that, eventually, become sound waves.

McGregor and White (1970) justified research on cavity instability by concluding that, in transonic and supersonic flows, aerodynamic drag in surfaces with cavities is greatly increased if there is an acoustic resonance. Dix and Bauer (2000) point out that pressure fluctuations due to cavities may reach great amplitudes that, besides the acoustic emission, might cause structural fatigue as they are specially correlated waves, causing repetitive stress on some structural points. Outside of the aeronautical scope, other justifications may be found. Kook and Mongeau (2002), for example, were motivated by automotive sunroofs.

More recently, cavity flow control came into the scope of researchers (HOWE, 1997; COLONIUS, 2001; ROWLEY; WILLIAMS, 2006). Control can be either passive, done by features such as grills, spoilers and ramps, or active, by using suction, jets, oscillators and piezoelectric components (CATTAFESTA et al., 2003; WILLIAMS; ROWLEY, 2006; THEOFILIS, 2011).

2.2.2 Cavity instability and acoustic modes

Rossiter (1964) has performed an experimental campaign at subsonic and transonic velocities, resulting in his famous semi-empirical equation, which connects flow parameters, such as Mach number and cavity length to the observed sound frequencies. It is still largely used to this date (COLONIUS, 2001; GLOERFELT, 2009). His equation has some

empirical constants, obtained experimentally.

This equation assumes that the unstable mode that generates sound is triggered by acoustic feedback. In short, when a vortex reaches the cavity's downstream edge, it generates acoustic waves that travel back to the upstream edge, triggering the shear layer modes that generate another vortex.

Rossiter's equation matches well with experimental results, despite a considerable dispersion, especially at lower Mach numbers. The saturation amplitudes of the modes present a much higher dispersion that the frequencies, due to the high sensitivity to disturbances in the shear layer. (COLONIUS, 2001)

Through the years, various corrections and adjustments of empirical values have been suggested to Rossiter's equation. (HELLER; HOLMES; COVERT, 1971; ROCKWELL; NAUDASHER, 1979)

Plumblee, Gibson and Lassiter (1962) have proposed another mode for sound generation in an open cubic cavity, later extended to other geometries by Tam (1976). In this mode, stationary waves normal to the flow receive energy from the shear layer over the cavity, modes are selected depending on their frequencies and this energy is sent back to the flow in acoustic form. In this work, the Navier-Stokes equations were simplified by several hypotheses. After the boundary conditions were applied, the resulting equation predicts the frequencies and modes and depends on no empirical constants, just on two integers, related to the mode number.

East (1966) linked aeroacoustic feedback mechanisms (Rossiter) to acoustic resonance mechanisms (Plumblee), concluding that they may interact with each other, amplifying the sound output if their frequencies match.

Comparing his results to experiments, Tam concluded that they are valid only for cavities with a depth greater than their length and above a certain Mach number, around 0.25. He arguments that in shallow cavities or at lower Machs, the energy absorbed by the standing waves is much less than what is needed to generate sound, damping these waves until they are practically non-existent. This complements East's conclusions.

Block (1976) has also compared both mechanisms experimentally, reaching a similar conclusion. Deeper cavities tend to have stronger acoustic resonance modes while longer ones have stronger aeroacoustic feedback modes. Peaks in sound intensity were also observed when the modes matched in frequency. She has also noted that at higher velocities, only the feedback modes are seen, other modes appear at lower velocities, widening the spectrum. This mode interaction was also discussed by Rockwell and Naudasher (1979), Yamouni, Sipp and Jacquin (2013).

Sarohia (1977), motivated by issues such as the changes in drag caused by cavities, has experimentally swept a range of cavity dimensions and Reynold numbers. In these

experiments, he has found that there is a minimum cavity length that causes it to oscillate, given as a function of incoming boundary layer thickness and Reynolds number. He also notes that when Rossiter modes appear in the cavity, only a single Rossiter mode is present at any given time and that the order of this mode is highly dependent on the length of the cavity.

Howe (2004) identifies the sound generation mechanisms at low Mach numbers, roughly from 0.01 to 0.2. He uses a Green's function for this geometry and analytical models of the sources, treating them as monopoles and dipoles. The monopole source is associated with the net flux of mass entering or leaving the cavity, while the dipole is associated with an unsteady drag force caused by the interaction of the vorticity and the cavity trailing edge, which happens due to the shear layer instability.

Howe concludes that at very low Mach numbers the sound radiation is dominated by the dipole source caused by the unsteady drag force, while at slightly higher Mach numbers, the monopole source takes over. This is illustrated in Fig. 2.5, which compares the directivity at Mach 0.05 and at Mach 0.1.

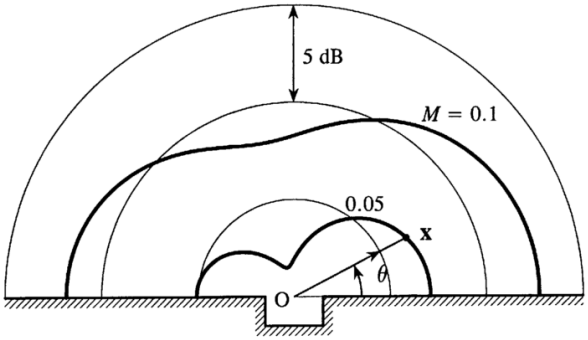

Figure 2.5 – Cavity acoustic directivity at Mach 0.05 and Mach 0.1. (HOWE, 2004)

He also concludes that, at lower frequencies, the emission is dominated by the dipole and, at higher frequencies, by the monopole, as can be seen in Fig. 2.6.

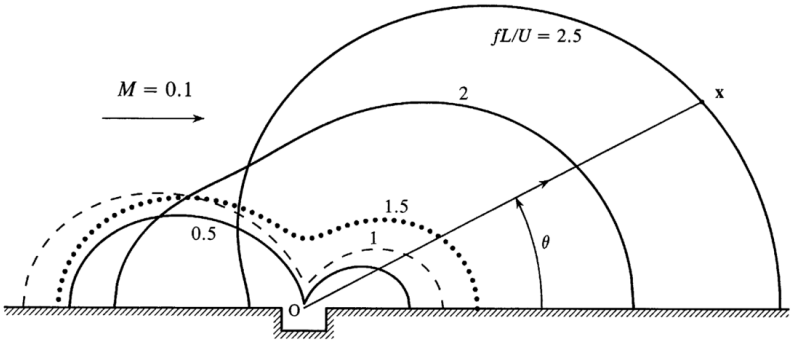

Figure 2.6 – Cavity acoustic directivity at Mach 0.1 for various frequencies. (HOWE, 2004)

Brès and Colonius (2008) performed open cavity simulations with high order finite difference schemes (LELE, 1992) to investigate the interaction between two and three-dimensional modes. Mack and Schmid (2010) have studied the instability in a swept cavity in supersonic flows by using a combination of a DNS and Krylov subspace algorithms.

The acoustic emission of a cavity is strongly linked to its oscillation modes and depends on the existence of unstable eigenvalues. Great advances were achieved in this direction by bi-global instability analysis (THEOFILIS, 2003; BRÈS; COLONIUS, 2008; VICENTE et al., 2014). Eigenvalues in the complex plane can be mapped for the cavity flow, indicating the existence of unstable modes and their respective frequencies. These modes grow until non-linear effects cause them to reach a saturation point.

Yamouni, Sipp and Jacquin (2013) related modes from bi-global stability analysis to Rossiter and standing wave modes in a square cavity. They conclude that interactions between these two phenomena may affect the global mode, causing it to be more unstable when their frequencies match.

Many recent investigations on open cavities focus on the flow stability. Meseguer-Garrido et al. (2014) perform a parametric study of the flow and its instability modes. Liu, Gómez and Theofilis (2016) compare two-dimensional cavities, with an infinite span, to three-dimensional ones, with a finite span, concluding that most effects are shared by both geometries. These last results were obtained for incompressible flows and acoustic analogies might be done from them. A compressible flow would be needed if direct observation of the acoustic field is desired.

A limited number of papers were found in the literature about mid to high subsonic flows over a cavity, such as Brès and Colonius (2008), Yamouni, Sipp and Jacquin (2013), Sun et al. (2016), Sun et al. (2017), which mostly focus on how the Mach number affects the stability. This range of Mach numbers is certainly important for practical reasons as this is where most modern aircraft fly. This work is in the direction of expanding the current knowledge of open cavity flows in this sense, a focus will be given to the effect of the boundary layer thickness over the cavity, about which not much was found.

2.2.3 Gaps

Small geometry elements in a flat plate have also been studied recently, they differ from larger geometries because their effect is strongly related to the boundary layer mechanics. We define a gap as a subset of open cavities in which its dimensions are of the same order of the boundary layer thickness. The flow over a gap may be divided into two different scenarios. One is when the gap is globally unstable, which means that its oscillations are self-sustained. In this case, it acts as a source of disturbances to the flow, and might even cause bypass transition, regardless of incoming disturbances. This

behavior resembles that of larger open cavities, as external disturbances have little effect on the modes inside the gap.

The second scenario is when the gap is globally stable. In this case, the flow upstream to the gap already has some kind of disturbance, which will then interact with the gap. Therefore, the surface imperfection is not the cause of disturbances as is the case with larger cavities, instead it modifies the existing flow instabilities. (CROUCH; NG, 2000; PLOGMANN; WÜRZ; KRÄMER, 2014; PAULA et al., 2017)

Klebanoff and Tidstrom (1972) concludes that the effect of a small two-dimensional imperfection is mostly related to the change in the mean flow and in the boundary layer thickness. A similar conclusion is reached by (WORNER; RIST; WAGNER, 2003), who simulate monochromatic TS waves passing over a small bump in the surface.

Experiments by Wang and Gaster (2005), Crouch, Kosorygin and Ng (2006) lead to empirical relations on how much a step in the flat plate affects the incoming Tollmien-Schlichting waves (TS waves). In terms of the transition n-factor, backward-facing steps have a stronger destabilizing effect on the boundary layer than forward-facing steps, caused by both the increase in its thickness and the laminar recirculation bubble that is created. Crouch mentions that these results are valid up to a step height of 1.5 times the boundary layer displacement thickness.

Paula et al. (2017) has experimentally measured 2D TS waves interacting with a small, localized roughness element. Part of his conclusion is that the roughness may cause the scattering of these waves, which may trigger non-linear interaction between different modes.

Qadri and Schmid (2017) have studied the mechanisms present in small cavities that select and amplify certain frequencies of the disturbances, even if the cavity itself is globally stable.

Gaster (2016) models a series of very sinusoidal bumps, which form a rough region, he concludes that this region amplifies the growth of unstable waves, causing the transition to move upstream. He also concludes that a good model for such flow is separating it in two regions, one governed by the Orr-Sommerfeld equations, above the bumps and one governed by the Stokes equation, in between the bumps.

Crouch, Kosorygin and Sutanto (2020) experimentally measure the change in the transition location of when a gap is present. They note that a bypass transition takes place when either the gaps length or depth are above certain threshold values. Figure 2.7, by Crouch, Kosorygin and Sutanto (2020), shows the movement of the transition to turbulence for gaps of various lengths (w) and depths (d), the value ξ represents the distance from the gap to the transition in comparison to the case without the gap. The dashed lines in the figure correspond to bypass transition data by Beguet et al. (2017). These experiments

were performed at Reynolds numbers similar to those used in Chapter 6 of this work, but at lower Mach numbers.

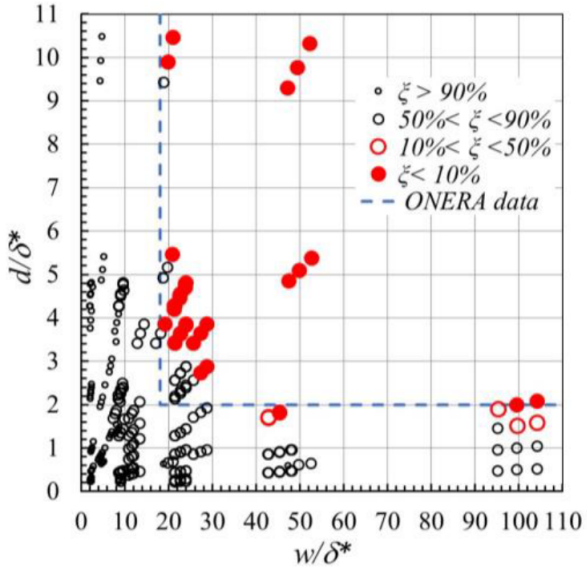

Figure 2.7 – Effect of the gap on the transition location. (CROUCH; KOSORYGIN; SUTANTO, 2020)

Chapter 3

Direct Numerical Simulation

The Direct Numerical Simulation code used in this work was developed as part of this project and is specifically tailored for our needs, in the form of the following requirements:

1. High order of precision both spatially and temporally wise and low rounding error.
2. Ability of accepting any Cartesian geometry, such as cavities and roughness elements or any combination of both.
3. Modularity for the implementation of new features needed for future research topics by the group.
4. Scalability to run in computers ranging from workstations to clusters.
5. Ease of use, including pre- and post-processing phases.

This code is based on previous works by the research group and inherits many of their algorithms but was completely rewritten. (SOUZA; MENDONÇA; MEDEIROS, 2005; SILVA; SOUZA; MEDEIROS, 2010; BERGAMO et al., 2015; MARTINEZ, 2016; MATHIAS; MEDEIROS, 2018)

Besides the studies presented in this thesis, the code is also in use by other members of the research group, such as for the simulation of TS waves passing over a small roughness element (HIMENO; MATHIAS; MEDEIROS, 2019; CARVALHO; MATHIAS; MEDEIROS, 2020; HIMENO; MATHIAS; MEDEIROS, 2020), the acoustic receptivity of roughness elements (SANTOS et al., 2020) and ongoing research on the influence of a small gap on the turbulent transition.

The code is published online on the Github platform at <https://github.com/marlonsmathias/GATT_DNS>. It is licensed under the GPLv3, meaning everyone can

use and modify the code, as long as credits are given and eventual modifications are also under the same license and, therefore, remain open-source.

3.1 Numerical methods

3.1.1 Governing equations

The compressible Navier-Stokes equations are used to model the flow, along with mass and energy conservation equations. A compressible flow can be entirely defined by five variables: density (ρ), internal energy (e) and the three velocity components (u,v,w), in this case. Each variable depends on location (x,y,z) and time (t).

Equations are written in the non-conservative form, which solves for each individual variable mentioned above, simplifying the boundary conditions.

$$\frac{\partial \rho}{\partial t} = -\rho \frac{\partial u_i}{\partial x_i} - \frac{\partial \rho}{\partial x_i} u_i \tag{3.1}$$

$$\frac{\partial u_j}{\partial t} = \frac{\partial u_j}{\partial x_i} u_i - \frac{1}{\rho} \frac{\partial p}{\partial x_j} + \frac{1}{\rho} \frac{\partial \tau_{ij}}{\partial x_i} \tag{3.2}$$

$$\frac{\partial e}{\partial t} = \frac{\partial e}{\partial x_i} u_i - \frac{p}{\rho} \frac{\partial u_i}{\partial x_i} + \frac{1}{\rho} \tau_{ij} \frac{\partial u_j}{\partial x_i} - \frac{1}{\rho} \frac{\partial q_i}{\partial x_i} \tag{3.3}$$

Where the viscous tensor and the heat flux term are:

$$\tau_{ij} = \frac{\mu(T)}{Re} \left(\frac{\partial u_i}{\partial x_j} + \frac{\partial u_j}{\partial x_i} - \frac{2}{3} \delta_{ij} \frac{\partial u_k}{\partial x_k} \right) \tag{3.4}$$

$$q_i = -\frac{\mu}{(\gamma - 1)\, Re\ Pr\ M_\infty^2} \frac{\partial T}{\partial x_i} \tag{3.5}$$

Temperature and pressure, assuming an ideal gas, are given by:

$$T = e\gamma\,(\gamma - 1)\, M_\infty^2, \quad p = (\gamma - 1)\, \rho\ e \tag{3.6}$$

Viscosity is modeled by Sutherland's law:

$$\frac{\mu^*}{\mu_\infty} = \mu(T) = \frac{1 + C}{T + C} T^{\frac{3}{2}} \tag{3.7}$$

Defining $C = \frac{110K}{T_\infty^*}$ and $T_\infty^* = 300K$.

All values are non-dimensional, being normalized by the free flow speed, cavity depth and initial density. Reynolds, Prandtl and Mach numbers are given by:

$$Re = \frac{\rho^*_\infty \, U^*_\infty \, L_0}{\mu^*_\infty}, \quad Pr = \frac{\mu^*_\infty c^*_p}{k^*}, \quad M_\infty = \frac{U^*_\infty}{\sqrt{\gamma \frac{p^*_\infty}{\rho^*_\infty}}} \tag{3.8}$$

Dimensional (denoted with a *) and non-dimensional values are related by the following equations.

$$\rho = \frac{\rho^*}{\rho^*_\infty}, \quad p = \frac{p^*}{p^*_\infty U^{*2}_\infty}, \quad x_i = \frac{x^*_i}{L_0}, \quad T = \frac{T^*}{T^*_\infty}, \quad u_i = \frac{u^*_i}{U^*_\infty}, \quad t = \frac{t^* U^*_\infty}{L_0}, \quad e = \frac{e^*}{U^{*2}_\infty} \tag{3.9}$$

3.1.2 Meshing and domain

The mesh is structured and Cartesian, meaning it can be stored is array format, which simplifies programming and speeds up the execution.

The grid can be stretched so that specific regions of the flow can have a higher density of nodes, such as the leading edge of the flat plate or the corners of the cavity. A stretching function was developed so that grid spacing always changes smoothly.

As a default, the mesh is uniformly spaced. Points and regions we call "attractors" can be added to the domain, those will cause nearby nodes to move towards the attractor, creating a region with greater refinement. Each attractor point has two parameters: strength and size; the former defines the ratio between the most refined nodes and the base spacing of the mesh, and the latter defines the size of the region the attractor affects. Attractor regions are defined by five parameters: region start, start of maximum refinement, end of maximum refinement, region end and refinement strength.

Figure 3.1 illustrates a mesh generated by this scheme. There are 100 nodes in the domain $0 \leq X \leq 10$. Two attractors were used at $X = 3$ and $X = 4$, which in this example could be both corners of a cavity. The strengths are set to 2 and 3; therefore, node concentrations are tripled and quadrupled, respectively. Both attractors are of size 0.5.

After the mesh is generated, a second routine is called to make sure there are mesh nodes right on top of certain geometric features, such as the leading edge or the cavity nodes. This routine finds which node is closest to each feature and slightly and smoothly distorts the mesh to make sure they match.

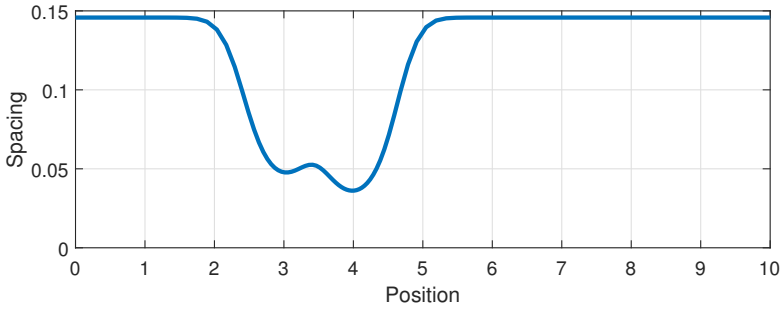

Figure 3.1 – Example of mesh generated using two attractor points at both ends of a cavity.

3.1.3 Boundary and initial conditions

The inflow boundary is defined as a uniform flow at constant temperature and a Neumann condition is placed for the pressure so that its derivative is null in the flow direction. In the outflow, pressure is kept constant, and the second derivative is null for the other variables. The outer flow condition sets the second derivative of all variables to zero.

Walls have no-slip and no-penetration conditions for velocity, the pressure gradient is set to zero in the normal direction and the temperature is fixed. Just downstream of the inflow, there is a free-slip region in the wall, it is necessary to accommodate the flow before the boundary layer starts forming.

Pressure and temperature are not directly available as variables in the code and are computed from the density and energy values. The temperature depends solely on the energy and pressure depends on both density and energy. This way, the boundary conditions routine first changes the energy to observe the temperature conditions and, later, the density to keep the pressure conditions.

Wall corners are points of particular attention for the boundary conditions. The Neumann homogeneous condition for pressure in other points is observed by computing the density at each point of the boundary so that the pressure's derivative is null in the normal direction on the wall. Corner nodes present a problem as walls in distinct directions meet and the density that observes the Neumann condition in one direction might violate it for the other. The pressure in set to the mean of the pressures that meet the boundary condition for each direction.

Open boundaries have the second derivative of all variables set to zero. We also add buffer (or sponge) zones near these boundaries. In these regions, three different techniques are combined to damp oscillations and prevent them from reflecting to the physical domain: The mesh spacing is greatly increased; the spatial derivative accuracy

order is reduced; Selective Frequency Damping is used (see Section 3.1.7). The transition between the physical domain and the buffer zones happens smoothly.

The inlet boundary has the stream-wise velocity set to unity. The energy is set to its free-stream value and the pressure stream-wise derivative is set to zero. The outlet has the pressure fixed at its free-stream value. Figure 3.2 illustrates these conditions and shows the mesh used for the cases of Chapter 4.

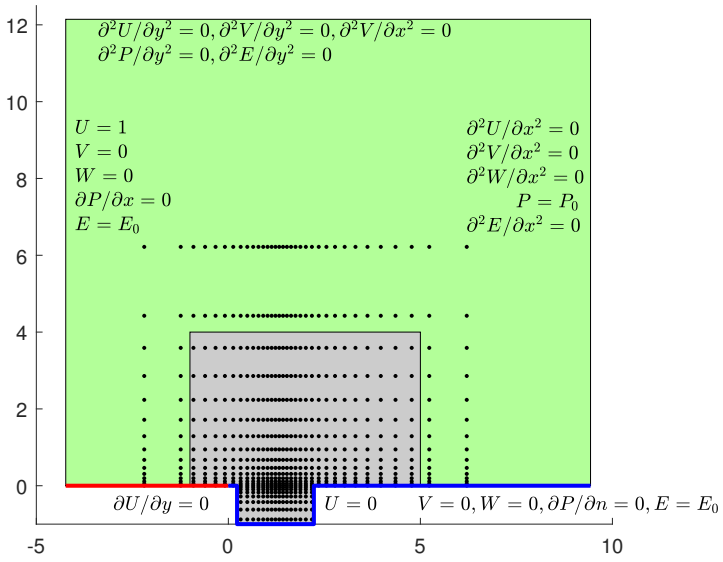

Figure 3.2 – Domain, mesh and boundary conditions of the flow simulation. The useful domain is marked in gray, while the buffer zone is green. One in every 10 nodes of the mesh is shown in black. The blue line represents wall boundaries, while the red line is a free-slip wall condition.

The initial condition is a Blasius boundary layer at constant pressure and temperature. Results from previous runs can also be used as initial condition; Reynolds and Mach numbers and the numerical methods may be changed; the code is also capable of interpolating the flow filed in case a different mesh was used to generate the initial flow. The boundary layer thickness at the cavity is controlled by changing its position with respect to the flat plate leading edge.

3.1.4 Spatial derivatives

Spatial derivatives are computed by a finite differences method chosen before runtime. Explicit second and fourth order methods are implemented, as well as compact fourth order spectral-like and sixth order schemes described by Lele (1992). It is possible to use a distinct differentiation method for the buffer zone, usually of a lower order, the transition from one method to the next happens smoothly.

The following equation must be solved when the derivative is needed:

$$\beta u'_{i-2} + \alpha u'_{i-1} + u'_i + \alpha u'_{i+1} + \beta u'_{i+2} = a\frac{u_{i+1} - u_{i-1}}{2h} + b\frac{u_{i+2} - u_{i-2}}{4h} + c\frac{u_{i+3} - u_{i-3}}{6h} \quad (3.10)$$

α, β, a, b and c are adjustable coefficients, h is the mesh spacing, f_i is the function value at node i and f'_i, its approximated derivative.

If both α and β are null, there is no need to solve a linear system as the derivative is given explicitly. The simplest scheme is the explicit second order, in which $a = 1$ and all other parameters are null. An explicit fourth order scheme has a=4/3 and b=-1/3.

The order of accuracy of a scheme is given by which of the following equations hold true for its coefficients.

$$\text{2nd order:} \quad a + b + c = 1 + 2(\alpha + \beta) \quad (3.11)$$

$$\text{4th order:} \quad a + 2^2 b + 3^2 c = 6\left(\alpha + 2^2\beta\right) \quad (3.12)$$

$$\text{6th order:} \quad a + 2^4 b + 3^4 c = 10\left(\alpha + 2^4\beta\right) \quad (3.13)$$

$$\text{8th order:} \quad a + 2^6 b + 3^6 c = 14\left(\alpha + 2^6\beta\right) \quad (3.14)$$

Despite being able to achieve high orders of formal accuracy, explicit schemes quickly lose precision at higher wave numbers, due to the increased high-order derivatives.

The modified wave number after the derivative is given by:

$$\omega'(\omega) = \frac{a\sin(\omega) + b\sin(2\omega)/2 + c\sin(3\omega)/3}{1 + 2\alpha\cos(\omega) + 2\beta\cos(2\omega)} \quad (3.15)$$

Lele (1992) uses this relation to derive some spectral-like derivative schemes. Ideally, the modified wave number would always match the original wave number.

Besides both explicit schemes, spectral-like derivative routines were implemented for fourth and sixth order accuracies. As an example, for the fourth order scheme, the restrictions are as follow:

1. Fourth order accuracy

2. Tridiagonal system

3. 5-point stencil

4. $\omega'(1.8) = 1.8$

For the first item, equations 3.11 and 3.12 must hold true. For the second and third items, chosen to reduce the computational cost, β=0 and c=0. For the fourth item, equation 3.15 must hold true for ω'=ω=1.8.

Therefore, there are five equations for the five variables, fully defining the system and resulting in α=0.364957272268410, β=0, a=1.57663818151227, b=0.153276363024547 and c=0.

The sixth order spectral-like scheme is done in a similar manner and results in a seven-point stencil in the right-hand side.

Figure 3.3 shows the modified wave number for some numerical schemes. Note how the spectral-like method stays closer to the exact value even at higher wave numbers.

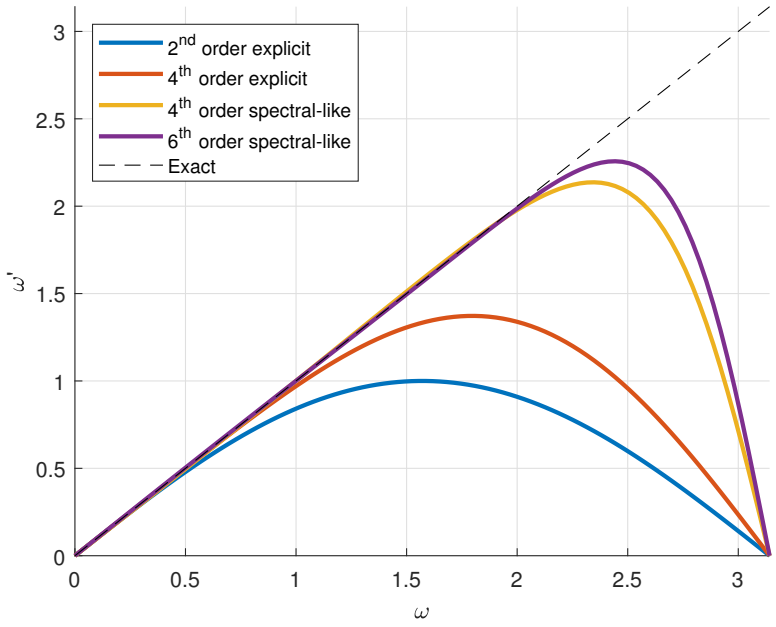

Figure 3.3 – Modified wave number for various numerical differentiation schemes.

Close to the boundaries, the stencil is shifted, and coefficients are adjusted accordingly. In order to avoid using large, decentered stencils, which has caused numeric stability problems, the derivative accuracy order may be decreased. For example, the sixth-order spectral-like scheme uses a seven-point stencil, accounting for the center point and three additional nodes on each side. Therefore, the node at the boundary and the two nodes next to it must have their stencil modified. In this work, we use the fourth-order spectral-like scheme two points removed from the boundary, the fourth-order Padé scheme one point remove from the boundary and a decentered third-order scheme at the wall with

coefficients so that the dissipation error at $\omega = \pi$ is $\pi/2$. In our experience, this scheme has a good stability and does not affect the accuracy of the solution.

It is important to note that these finite difference methods only work for equally spaced meshes. Therefore, the well know chain rule for derivatives must be used, as shown in the following equation.

$$\frac{\partial u}{\partial x} = \frac{\partial u}{\partial \phi}\frac{\partial \phi}{\partial x} \tag{3.16}$$

u is the function value and x is the actual mesh dimension. ϕ is the dimension in an intermediate mesh which corresponds node to node with the actual mesh. This intermediate mesh is equally spaced with $h = 1$. Therefore, both terms on the right-hand side of equation 3.16 can be obtained by standard finite difference methods. Note that the second term only needs to be computed once as it depends only on the mesh.

Once more, both corner nodes presented a challenge for these methods when computing the derivative. Figure 3.4 illustrates the Regions considered. In an inner node, i.e., away from the boundaries, finite differences method uses the nodes around it to approximate the derivative. If no other changes were made to the code, corners nodes 1 and 2 would be considered as inner nodes and, thus, derivatives computed for them would account for both points on the wall and points immersed in the flow, which would not be correct and cause the solution to fail. Because of this, both these nodes only consider values in Region 2 of figure 3.4.

This has solved the problem for both corner nodes and for the region between them. But nodes in Regions 1 and 3 of the figure would still have its derivatives miscalculated, causing discontinuities in the domain close to the corner, which would later cause the simulation to fail. This was solved by considering both the last node in Region 1 and the first node in Region 3 as inner nodes for the finite differences method, which makes the derivative a continuous function again.

In sum, derivatives in Region 2 depend only on values in it. Derivatives in Regions 1 and 3 depend on values both in their respective regions and on values in Region 2. The approach for wall-normal derivatives is analogous.

Equation 3.17 illustrates how the derivatives would be computed close to corner node 1, with index c_1. α, a, b and c are the finite differences coefficients, note that they are different for the corner nodes and more coefficients may be added depending on the derivative scheme chosen. D and f are vectors containing the derivatives and the function

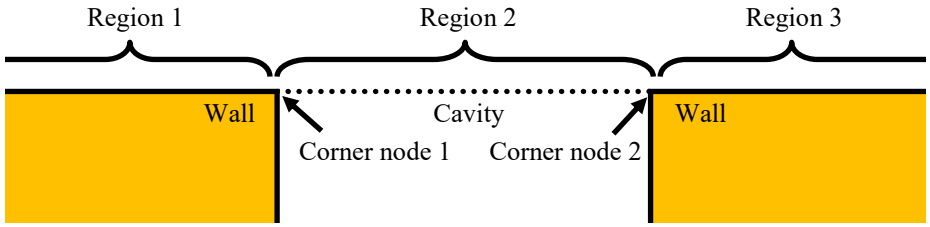

Figure 3.4 – Close-up of the corner nodes in the domain and the regions considered for derivatives.

values for each node, respectively.

$$
\begin{bmatrix}
1 & \alpha & & & & & \dots & 0 \\
\alpha & 1 & \alpha & & & & & \vdots \\
 & \ddots & \ddots & \ddots & & & & \\
 & & \alpha & 1 & \alpha & & & \\
 & & & & 1 & \alpha & & \\
\vdots & & & & \alpha & 1 & \alpha & \\
0 & \dots & & & & \ddots & \ddots & \ddots
\end{bmatrix}
\begin{bmatrix}
D_1 \\ D_2 \\ \vdots \\ D_{c_1-1} \\ D_{c_1} \\ D_{c_1+1} \\ \vdots
\end{bmatrix} =
$$

$$
= \begin{bmatrix}
a & b & c & & & & \dots & 0 \\
-a & 0 & a & & & & & \vdots \\
 & \ddots & \ddots & \ddots & & & & \\
 & & -a & 0 & a & & & \\
 & & & & a & b & c & \\
\vdots & & & & -a & 0 & a & \\
0 & \dots & & & & \ddots & \ddots & \ddots
\end{bmatrix}
\begin{bmatrix}
f_1 \\ f_2 \\ \vdots \\ f_{c_1-1} \\ f_{c_1} \\ f_{c_1+1} \\ \vdots
\end{bmatrix}
\tag{3.17}
$$

These matrices are analogous at to the second corner index, c_2.

As seen above, the linear system for nodes c_1 to c_2 can be decoupled from the others, while nodes from 1 to $c_1 - 1$ and from $c_2 + 1$ to n still depend on the central region. An analogous approach is taken in the wall-normal direction.

The code allows the buffer zones to use different schemes for spatial derivatives, usually lower orders are desired. A smooth cosine-shaped transition happens from the main scheme to the lower order one in this region.

For three-dimensional cases in which a single span-wise wave number is required, the code has a special routine that allows spectral derivatives to be computed in this direction. This is done by using four equally spaced nodes and setting $\alpha = 0$ and $a = \pi/2$ in the matrices of equation 3.17. These coefficients were obtained by setting $\omega' = \omega = \pi/2$ in

equation 3.15. When using this routine, one must make sure that all span-wise oscillations in the domain have the correct wave number, or else the derivatives will be miscalculated. This is especially useful for the global stability analysis, which will be explained in further detail in Chapter 4.

3.1.5 Time integration

Time integration is performed at a fixed time step by either an explicit Euler, a third order or a fourth order Runge-Kutta scheme.

The simplest method is the explicit Euler, shown in the following equation. $\boldsymbol{U}^n$ is the flow state at time step n and $\boldsymbol{f}$ is the time derivative of this flow.

$$\boldsymbol{U}^{n+1} = \boldsymbol{U}^n + \Delta t \boldsymbol{f}\left(\boldsymbol{U}^n\right) \tag{3.18}$$

The fourth order Runge-Kutta method is given by the equations below. Despite its higher computational cost at each step, it pays off by being able to take much larger steps without losing stability or precision.

$$\boldsymbol{U}^{n+1} = \boldsymbol{U}^n + \frac{\Delta t}{6}\left(\boldsymbol{K}_1 + 2\boldsymbol{K}_2 + 2\boldsymbol{K}_3 + \boldsymbol{K}_4\right) \tag{3.19}$$

$$\boldsymbol{K}_1 = \boldsymbol{f}\left(\boldsymbol{U}^n\right) \tag{3.20}$$

$$\boldsymbol{K}_2 = \boldsymbol{f}\left(\boldsymbol{U}^n + \frac{\Delta t}{2}\boldsymbol{K}_1\right) \tag{3.21}$$

$$\boldsymbol{K}_3 = \boldsymbol{f}\left(\boldsymbol{U}^n + \frac{\Delta t}{2}\boldsymbol{K}_2\right) \tag{3.22}$$

$$\boldsymbol{K}_4 = \boldsymbol{f}\left(\boldsymbol{U}^n + \Delta t \boldsymbol{K}_3\right) \tag{3.23}$$

The boundary conditions routine is called after each sub-step of the method.

The largest time step possible is defined by the method's numerical stability. For the flow's diffusive characteristics, equation 3.24 must be observed, and for the flow's convective characteristics, equation 3.25 must be observed. The maximum CFL value depends on the time integration method chosen. For the fourth order Runge Kutta, a CFL under around 1.3 is stable.

$$\Delta t \leq \frac{Re}{\left(\frac{1}{\Delta x_{min}^2} + \frac{1}{\Delta y_{min}^2} + \frac{1}{\Delta z_{min}^2}\right)} \tag{3.24}$$

$$\Delta t \leq \frac{CFL_{max}}{\left(\frac{1/Ma+u_{max}}{\Delta x_{min}} + \frac{1/Ma+v_{max}}{\Delta y_{min}} + \frac{1/Ma+w_{max}}{\Delta z_{min}}\right)} \tag{3.25}$$

The diffusive stability does not depend on the flow state, only on the mesh and on the Reynolds number, so it is only computed once. The convective stability depends on the flow velocity field and is computed at every step. Equation 3.25 also shows that for very low Mach numbers, closer to an incompressible flow, the time step would have to be significantly reduced due to the increased speed of sound waves compared to the flow velocity, considerably increasing the computational cost.

At very low Mach numbers, the incompressible Navier-Stokes equations would yield a much faster solution at the cost of not being able to identify any acoustic phenomena or the instability modes related to it. In the research group, there is an ongoing work evaluating the viability of the SIMEX method, which combines implicit and explicit time marching methods for distinct parts of the governing equations as a way of allowing larger time steps to be taken without the large computational penalty of solving all the governing equations implicitly. (RODRIGUES, 2017)

3.1.6 Anti-aliasing filtering

In this type of simulation, high-frequency numerical noise may quickly build up, causing the simulation to diverge from the physical solution.

In a real flow, some mechanisms transport energy from long wavelengths to shorter ones, until the molecular viscosity becomes strong enough to dissipate this energy. In a fully turbulent flow, this is known as the Kolmogorov scale (KOLMOGOROV, 1991). Simulations down to this scale would require extremely fine meshes and are outside the scope of this work and have a huge computational cost, outside the reach of modern computers for most geometries, even one as simple as an open rectangular cavity.

Eriksson and Rizzi (1985) state that, due to aliasing effects, the motion in the shortest wavelength resolved by the mesh is numerically transferred to long wavelengths, which causes the solution to diverge from the physical system.

A numerical low-pass filter attenuates this noise (GAITONDE; VISBAL, 1998). The filter strength can be adjusted before runtime and, ideally, should be as low as possible, minimizing its effect on results.

This filtering should be enough to dissipate the motion in short wavelengths before they reach the Nyquist frequency limit, which states that a mesh can only resolve wave lengths of, at least, twice the node spacing and that shorter oscillations would cause aliasing issues.

At both ends of the stencil and at discontinuities in the domain, a special treatment must be done as the stencil spans five points to each side. Three options are available in this implementation. Filtering can be turned off at those five last points; or decentered stencils can be used to keep the 10th order filtering; or the filtering order is progressively decreased in order to reduce the stencil and to keep it inside the useful domain.

Filtering is done at the end of each time step and requires solving a tridiagonal linear system for each direction.

It is implemented in a very similar manner to the spatial derivatives. The matrices for the linear system are formed and solved at the end of each time step. The treatment for border and corner nodes is the same as described in figure 3.4 and equation 3.17.

The system to be solved is the following:

$$\alpha_f \bar{u}_{i-1} + \bar{u}_i + \alpha_f \bar{u}_{i+1} = \sum_{n=0}^{N} \frac{a_n}{2} \left(u_{i-n} + u_{i+n}\right) \tag{3.26}$$

For this tenth order scheme, the coefficients are:

$$\begin{gathered} a_0 = \frac{193 + 126\alpha_f}{256}, \quad a_1 = \frac{105 + 302\alpha_f}{256}, \quad a_2 = \frac{-15 + 30\alpha_f}{64} \\ a_3 = \frac{45 - 2\alpha_f}{512}, \quad a_4 = \frac{-5 + 10\alpha_f}{256}, \quad a_5 = \frac{1 + -2\alpha_f}{512} \end{gathered} \tag{3.27}$$

α_f is an adjustable parameter from -0.5, which is maximum filtering, to 0.5, which is no filtering. u_i is the function value at node i and $\bar{u}_i$ denotes this value after filtering.

The spectral function of the filter shows the attenuation for each wavenumber. It is given by:

$$SF(\omega) = \frac{\sum_{n=0}^{N} a_n \cos\left(n\omega\right)}{1 + 2\alpha \cos\left(\omega\right)} \tag{3.28}$$

Figure 3.5 is a plot of this spectral function for various values of α for this tenth order scheme.

3.1.7 Artificial damping

This DNS is used in two distinct parts of this work. Besides being called during the instability analysis, it is also used to generate the base flow.

A fundamental requirement for this base flow to be used for instability analysis is to be steady, i.e., its derivatives with respect to time are null. Given that $\boldsymbol{f}(\boldsymbol{U})$ describes

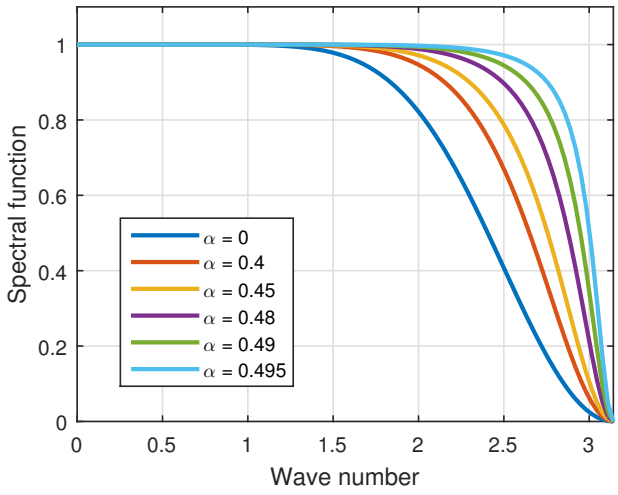

Figure 3.5 – Spectral function for the tenth order low-pass filter.

the time derivative of the flow $\boldsymbol{U}$, a steady state solution $\boldsymbol{U}_0$ suitable to be a base flow would yield

$$\boldsymbol{f}(\boldsymbol{U}_0) = \boldsymbol{0} \tag{3.29}$$

Two of the most straightforward methods to obtain $\boldsymbol{U}_0$ are:

1. Run the time evolution for a sufficient time to reach a steady flow within a certain tolerance.

2. Use a Newton iteration method to solve the non-linear system.

The first solution works only if all the base flow modes are stable and requires long simulations when close to critical stability conditions. An open cavity flow may not always meet this criterion, as it may be two dimensionally unstable, which would cause the simulation to reach a periodical solution.

At the critical stability condition, the time average of this periodical solution coincides with the base flow, but this is not true for unstable conditions. (SIPP; LEBEDEV, 2007)

The second solution has a very large computational cost for this type of system, with many variables. It would also require a considerable amount of recoding of the DNS.

Åkervik et al. (2006) propose a solution based on the first method, called the Selective Frequency Damping (SFD). It works as a low pass filter in the time domain, which damps the unstable modes present in the flow so that a physical steady state is reached by the simulation, even if it is physically unstable.

It is based on a proportional feedback control and works by adding a forcing term to the governing equations.

$$\frac{\partial \boldsymbol{U}}{\partial t} = \boldsymbol{f}(\boldsymbol{U}) - \chi(\boldsymbol{U} - \boldsymbol{w}) \tag{3.30}$$

Where $\boldsymbol{w}$, ideally, would be the target steady flow, but as it is not available at run time, it is substituted by a time filtered flow obtained by the convolution of $\boldsymbol{U}$ with a time filtering kernel T.

$$\boldsymbol{w} = \bar{\boldsymbol{U}}(t) = \int_{-\infty}^{t} T(\tau - t, \Delta)\boldsymbol{U}(\tau)d\tau \tag{3.31}$$

The filtering kernel can be defined as:

$$T(\tau - t, \Delta) = \frac{1}{\Delta} \exp\left(\frac{\tau - t}{\Delta}\right) \tag{3.32}$$

The cutoff frequency is given by:

$$\omega_c = \frac{1}{\Delta} \tag{3.33}$$

For the implementation, equations 3.31 and 3.32 as rewritten in the equivalent differential form:

$$\frac{\partial \bar{\boldsymbol{U}}}{\partial t} = \frac{\boldsymbol{U} - \bar{\boldsymbol{U}}}{\Delta} \tag{3.34}$$

This equation can be solved along with the actual flow, with few changes to the code and a small increase in the computational cost. Both χ from equation 3.30 and Δ from equation 3.34 are adjustable parameters.

χ controls the strength of the artificial damping. Low values may cause the system to remain unstable or very close to the critical condition. High values add too much damping, causing the system to take a very long time to converge.

Δ controls the cutoff frequency, which should be lower than the unstable mode's frequency. On the other hand, high values of Δ, therefore low cutoff frequencies, cause a similar effect to a strong damping, increasing the time needed for the solution to reach the steady state.

In summary, the following system of equations is solved through time:

$$\frac{\partial \boldsymbol{U}}{\partial t} = \boldsymbol{f}(\boldsymbol{U}) - \chi(\boldsymbol{U} - \bar{\boldsymbol{U}}) \tag{3.35}$$

$$\frac{\partial \bar{\boldsymbol{U}}}{\partial t} = \frac{\boldsymbol{U} - \bar{\boldsymbol{U}}}{\Delta} \tag{3.36}$$

When this system reaches a steady state, $\boldsymbol{U}$ and $\bar{\boldsymbol{U}}$ will be equal and the second term of the first equation will vanish. Therefore, $\boldsymbol{U}$ will represent the physical flow $\boldsymbol{U}_0$, which is steady.

To reduce the computational cost, a fourth order Runge-Kutta scheme may be used to solve for the physical part of the flow, which is only the first term of the right-hand side of equation 3.35, for its increased stability. While the other parts are solved by the simpler explicit Euler method. Hence, equation 3.19 is replaced by:

$$\boldsymbol{U}^{n+1} = \boldsymbol{U}^n + \frac{\Delta t}{6}\left(\boldsymbol{K}_1 + 2\boldsymbol{K}_2 + 2\boldsymbol{K}_3 + \boldsymbol{K}_4\right) - \Delta t\ \chi(\boldsymbol{U} - \bar{\boldsymbol{U}}) \tag{3.37}$$

With equations 3.20 to 3.23 still used for the sub steps $\boldsymbol{K}_1$ to $\boldsymbol{K}_4$. Equation 3.36 is solved through time by:

$$\bar{\boldsymbol{U}}^{n+1} = \bar{\boldsymbol{U}}^n + \Delta t \frac{\boldsymbol{U}^n - \bar{\boldsymbol{U}}^n}{\Delta} \tag{3.38}$$

It is worth noting that the goal of using this Selective Frequency Damping method is simply obtaining a steady state flow as quickly as possible. Therefore, there is no need for high precision algorithms for the time stepping. The Runge-Kutta algorithm is used because of its excellent stability properties, allowing larger time steps.

It is also possible to use this method only in the buffer zone to mitigate problems at the boundary conditions such as reflections. In this case, χ is multiplied by a parameter η that depends on the position, which varies smoothly from zero at the beginning of the buffer zone to one at the domain boundary.

3.2 Implementation

The DNS code used in this work is developed in-house and is a revision of the code used previously by our group. The preprocessing is done in Matlab® and includes the following steps:

- Receive the input parameters
- Create a directory for the results and initialize log files
- Generate the mesh
- Identify walls immersed in the domain

- Organize the domain partition for parallelization
- Set up the boundary conditions
- Set up matrices with coefficients for the spatial derivatives and filters
- Create the initial flow

The processing itself is written in FORTRAN, compiled by gfortran[1]. The Matlab® part of the code automatically writes some of the FORTRAN files and calls the compiler, this is done to minimize overheads as the DNS is executed.

Flow files are saved in .mat format, which is a compressed lossless format that takes roughly half the disk space of an equivalent binary file in our usage.

3.2.1 Domain decomposition and parallel execution

For the parallel execution, the domain is decomposed in slices and each one is sent to a different process. Figure 3.6 illustrates this decomposition, as done by the 2DECOMP&FFT library, which uses the MPI protocol (LI; LAIZET, 2010).

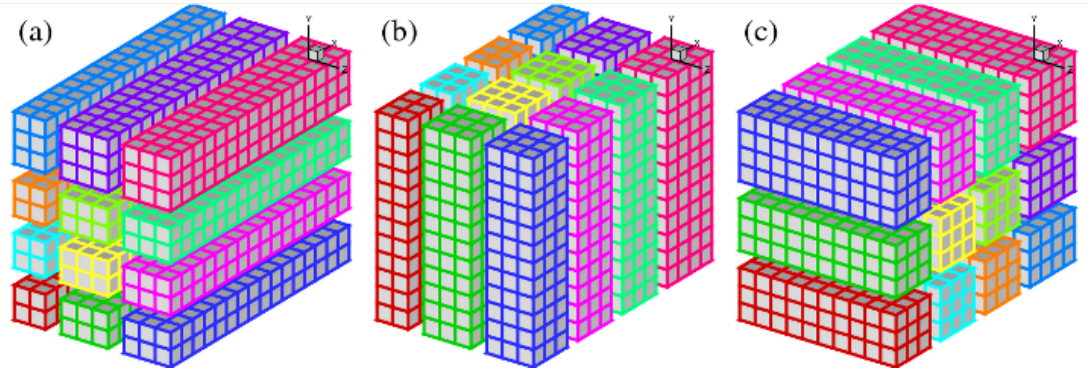

Figure 3.6 – Scheme of a three-dimensional domain decomposed for a grid of 3x4 processes (LI; LAIZET, 2010).

Each MPI process holds all points of the domain in one direction, but not in the others. For most operations, the decomposition in x is used, i.e., each process can access all points in x for their values of y and z. Which means that for the derivatives and filters in all directions to be computed, the domain must be transposed once for each direction. This process is illustrated in figure 3.7. An analogous routine is used for the noise filtering in each direction.

The flow geometry must be taken in account when choosing the number of nodes to be used. The subroutine for the boundary conditions is called when the domain in

[1] <https://gcc.gnu.org/fortran/>

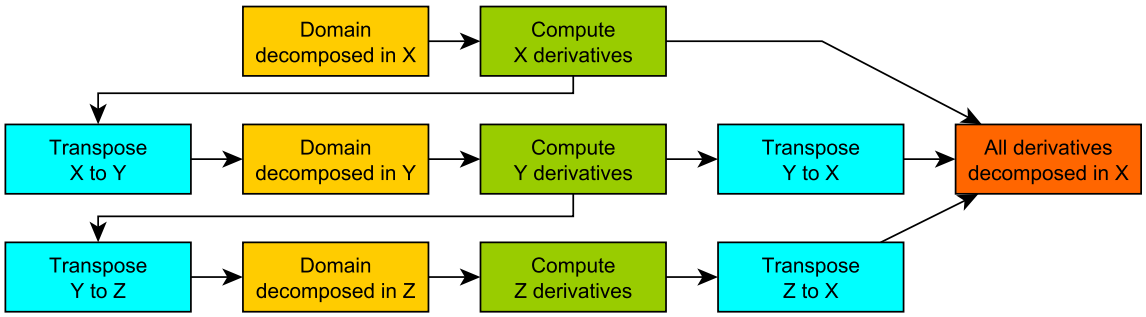

Figure 3.7 – Flowchart to obtain derivatives of the decomposed domain.

decomposed in the stream-wise x direction, i.e., no program instance has access to all values of y and z in the domain. This becomes an issue when computing wall-normal Neumann boundary conditions, as a number of points in the y direction are needed at this step and all these nodes should be contained in the same instance, to avoid communication overhead. Therefore, all points needed for the Neumann conditions must be contained in a single instance.

3.2.2 Linear system solver

Both the spatial derivatives and the spatial filter are implicit. Using either of them involves solving a tridiagonal matrix, which is done with the Thomas algorithm. A sample system is shown below, where y_i are known values and the solver must compute d_i.

$$\begin{bmatrix} b_1 & c_1 & & \cdots & a_1 \\ a_2 & b_2 & c_2 & & \vdots \\ & a_3 & b_3 & \ddots & \\ \vdots & & \ddots & \ddots & c_{n-1} \\ c_n & \cdots & & a_n & b_n \end{bmatrix} \begin{bmatrix} d_1 \\ d_2 \\ \vdots \\ d_n \end{bmatrix} = \begin{bmatrix} y_1 \\ y_2 \\ \vdots \\ y_n \end{bmatrix} \tag{3.39}$$

When $a_1 = c_n = 0$, the system is non-cyclical and therefore can be solved by the Thomas algorithm:

1: **for** $i = 2 \cdots n$ **do**
2: $\quad a_i = a_i / b_{i-1}$
3: $\quad b_i = b_i - a_i c_{i-1}$
4: $\quad y_i = y_i - a_i y_{i-1}$
5: **end for**
6: $d_n = y_n / b_n$
7: **for** $i = n - 1 \cdots 1$ **do**
8: $\quad d_i = (y_i - c_i d_i) / b_i$
9: **end for**

If the system is cyclical, the algorithm proposed by Temperton (1975) is used. The first line of the inverse of the tridiagonal matrix is computed during the preprocessing and stored. This line is used to obtain the value of d_1 from the vector y. The system is then modified to:

$$\begin{bmatrix} b_2 & c_2 & & \cdots & 0 \\ a_3 & b_3 & c_3 & & \vdots \\ & a_4 & b_4 & \ddots & \\ \vdots & & \ddots & \ddots & c_{n-1} \\ 0 & \cdots & & a_n & b_n \end{bmatrix} \begin{bmatrix} d_2 \\ d_3 \\ \vdots \\ d_n \end{bmatrix} = \begin{bmatrix} y_2 - a_1 d_1 \\ y_3 \\ \vdots \\ y_n - c_n d_1 \end{bmatrix} \tag{3.40}$$

which can be solved by the Thomas algorithm.

3.2.3 Flowchart

Two flowcharts were prepared to illustrate how the distinct parts of the code interact. The first one, in figure 3.8, focuses on the preprocessing stage. The top line of each frame identifies the task, while the bottom line shows which file contains it. The second flowchart, in figure 3.9, shows the interaction between the routines in the FORTRAN part of the code, where the simulation is performed.

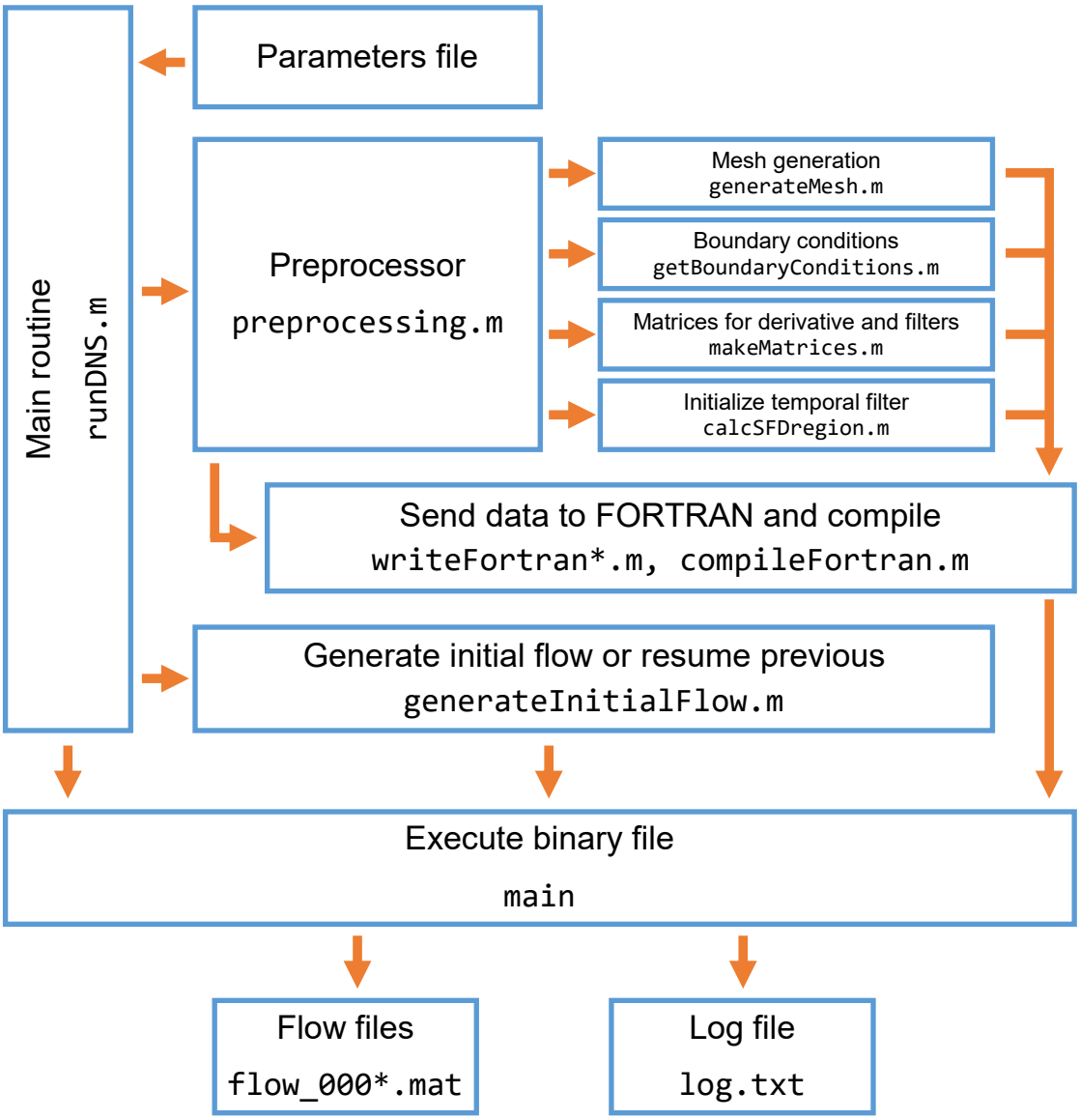

Figure 3.8 – Flowchart of the DNS. The top line of each frame identifies the task, while the bottom line shows which file contains it.

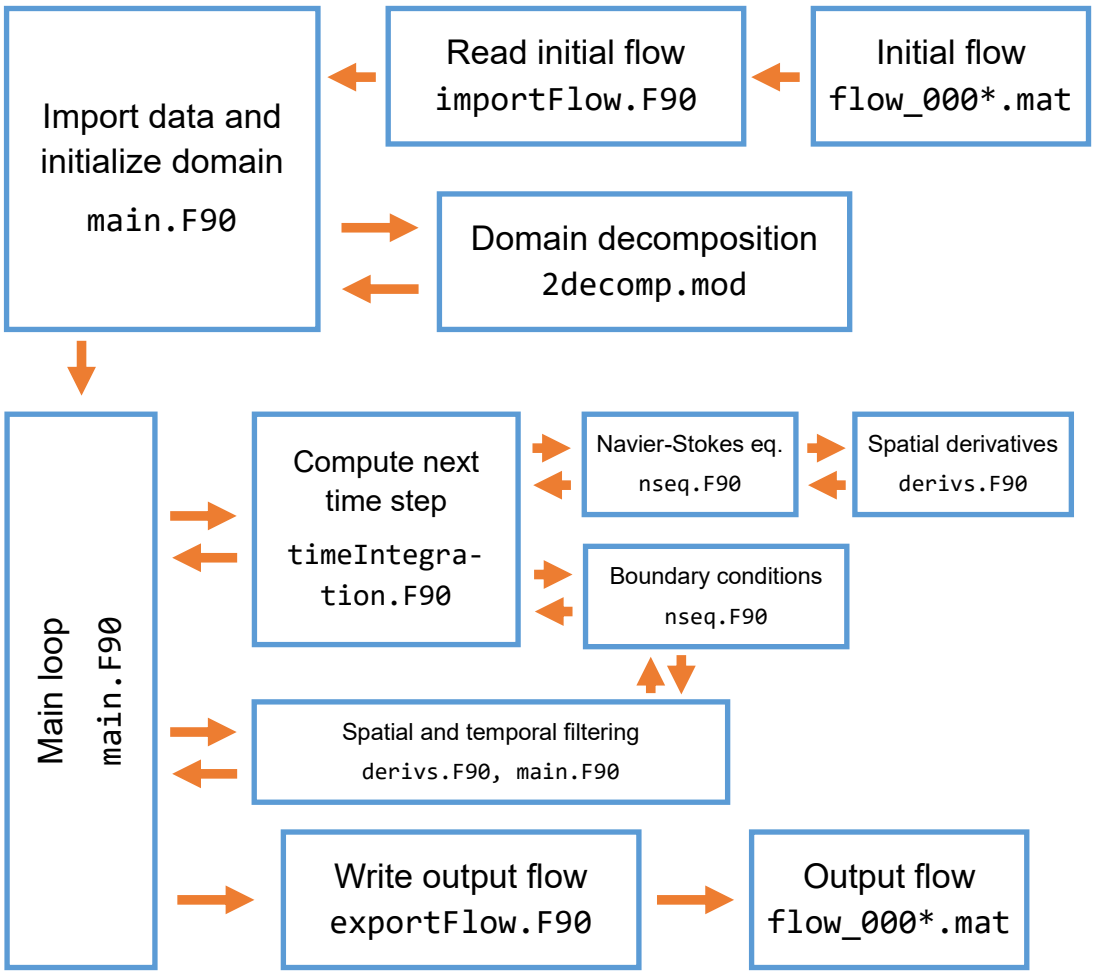

Figure 3.9 – Flowchart of the simulation routine of the DNS. The top line of each frame identifies the task, while the bottom line shows which file contains it.

3.3 Performance

To test the code performance, two test scenarios were defined. The code was executed in a server with 72 CPU cores at a nominal clock of 3.1 GHz.

The first scenario is a 2D domain, with 640×260 mesh nodes, run for 1000 time steps (each with 4 sub-steps due to the fourth order Runge Kutta method plus a filtering step). Table 3.1 brings the total execution times and the respective parallelization efficiency. Some of the cases were run multiple times with no significant change in results.

The normalized time is the total run time divided by the number of nodes in the mesh and amount of time steps. The efficiency is calculated by dividing the total speed-up by the number of processors used.

The parallelization strategy was highly efficient with up to 12 processors. Above that number, the MPI overhead started significantly affecting the performance gains. With 8 and 10 processors, an efficiency greater than 100% was achieved, this is a phenomenon known as super-linear speed-up, which may be caused by several factors, most likely the increased cache memory available to the code as more processors were allocated, reducing the data transfer to and from the RAM.

The second scenario is a 3D case with $640 \times 260 \times 16$ mesh nodes, run for a total of 100 time steps. This time, there was no super-linear scaling of performance, likely due to the increased total domain size. The array column in table 3.2 indicates how many domain partitions were used in the y and z directions, respectively.

Figure 3.10 summarizes the results from tables 3.1 and 3.2. In cases where multiple array configurations were used for the same number of processors, only the best result is

Table 3.1 – DNS execution time for different numbers of parallel processes, two-dimensional case.

Processors	Total time (s)	Normalized time (ns)	Speed-up	Efficiency
1	240	1445	1.00	100%
2	122	734	1.97	98%
3	81.4	489	2.95	98%
4	63.1	379	3.81	95%
6	42.2	254	5.69	95%
8	27.7	167	8.66	108%
10	23.4	141	10.3	103%
12	22.1	133	10.9	91%
15	20.7	124	11.6	77%
20	14.1	85	17.0	85%
30	10.4	63	23.0	77%
35	10.5	63	22.9	65%
40	10.0	60	24.0	60%

Table 3.2 – DNS execution time for different numbers of parallel processes, three-dimensional case.

Processors	Array	Total time (s)	Normalized time (ns)	Speed-up	Efficiency
1	1 × 1	913	3432	1.00	100%
2	1 × 2	469	1762	1.95	97%
2	2 × 1	472	1773	1.94	97%
4	1 × 4	234	880	3.90	97%
4	2 × 2	234	879	3.90	98%
4	4 × 1	247	928	3.70	92%
8	1 × 8	118	444	7.72	97%
8	2 × 4	119	448	7.66	96%
8	4 × 2	122	459	7.47	93%
8	8 × 1	123	465	7.38	92%
10	10 × 1	104	394	8.71	87%
16	2 × 8	70.0	263	13.1	82%
16	4 × 4	70.3	264	13.0	81%
16	8 × 2	71.6	269	12.8	80%
20	10 × 2	62.3	234	14.7	73%
32	4 × 8	47.6	179	19.2	60%
32	8 × 4	47.4	178	19.3	60%
40	10 × 4	43.8	165	20.8	52%
64	8 × 8	38.8	146	23.5	37%

shown in the figure. Note that these values are only valid for this case in this computer and may vary drastically for larger or smaller meshes and for different computational environments. Larger meshes tend to be more scalable.

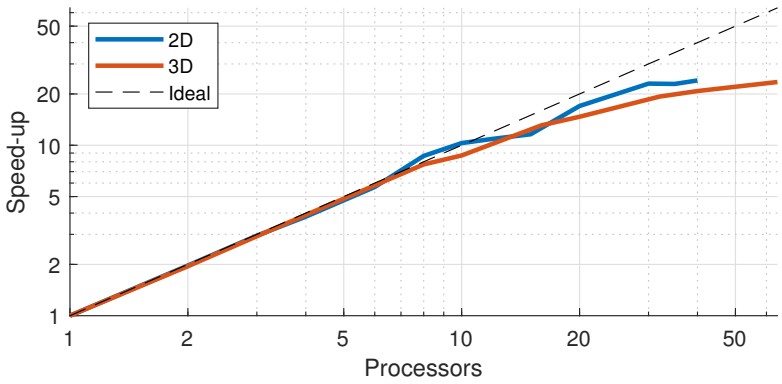

Figure 3.10 – Speed-up obtained for different numbers of processors for our 2D and 3D test cases.

When compared to the previous code developed by our group, the performance was considerably improved. In 2D cases, for the same number of processors, the run time was reduced to about one third, while in 3D cases it was roughly halved.

3.4 Strategies for mesh generation

When setting up a case to be solved by this DNS, a new mesh must be defined. By combining an analysis of the numerical methods with the experience of the research group, we have created a small set of rules that one could follow when generating a new mesh. Naturally, following these rules does not guarantee that the simulation is mesh-independent; however, they provide a good starting point.

- At least 13 points per period are necessary to accurately resolve a spatial wave.
- The minimum wall-normal mesh spacing must be, at most, 10% of δ^* at the region of interest.
- The cavity corners are usually the most critical region for mesh spacing, due to the large gradients.
- Node spacing should not change more than 10% from one node to the next in regions the flow if expected to oscillate.
- The wall-normal physical domain must be, at least twice as large as δ_{99} at the outflow.

To follow these rules, one must first estimate which frequencies are to be expected in each part of the domain. For a flat plate, spatially unstable TS waves have an angular velocity below $\omega = 0.15$, when normalized by the local δ^*. By approximating the convection velocity of TS wave to a third of the free flow velocity, the minimum length of an unstable TS wave is around $15\delta^*$, therefore the stream-wise spacing of the flow should be, at most, $1.15\delta^*$.

Phenomena inside the cavity may happen at higher frequencies. A cavity of length $L = 10\delta^*$ in a flow of Mach number $Ma = 0.5$ is expected to have its third Rossiter mode (R3) at an angular velocity of $\omega = 0.7$. Therefore, the maximum spacing should be $0.25\delta^*$, if R3 is assumed to be the phenomenon of interest that happens at the highest frequency.

Figure 3.11 illustrates the mesh for a gap case with the following parameters: $Re_{\delta_0^*} = 600$, $L = 10$, $D = 5$, $Ma = 0.5$. All lengths are normalized by δ^* at the gap leading edge. The spacing in the flow direction (X) is 1 at most of the domain. There is a region with spacing 4 upstream from the cavity, as TS waves are not expected there. The spacing at the flat plate leading edge is locally reduced to 2 as means to correctly resolve the larger gradients there. A region with spacing 0.2 spans from the gap leading edge to $30\delta^*$ downstream from its trailing edge. This is necessary due to the higher frequency phenomena in the gap and their resulting TS waves, which dissipate downstream due to

being spatially stable. Both gap corners are further refined due to the large gradients, the leading edge has a minimum spacing of 0.065 and the trailing edge, of 0.05.

In the flow-normal direction (Y), the minimum spacing is 0.065 and occurs at the flat plate. The spacing is smoothly increased to 0.5 at the gap bottom and to 1 at the free flow, away from the flat plate. Including the buffer zones, this mesh has 766 nodes in X and 214 in Y.

The physical domain goes from 0 to 413 in X and from -5 to 20.7 in Y. The origin is placed at the flat plate leading edge. Including the buffer zones, the domain spans $-517 \leq X \leq 1006$ and $-5 \leq Y \leq 274$. The gap is between $X = 202.8$ and $X = 212.8$.

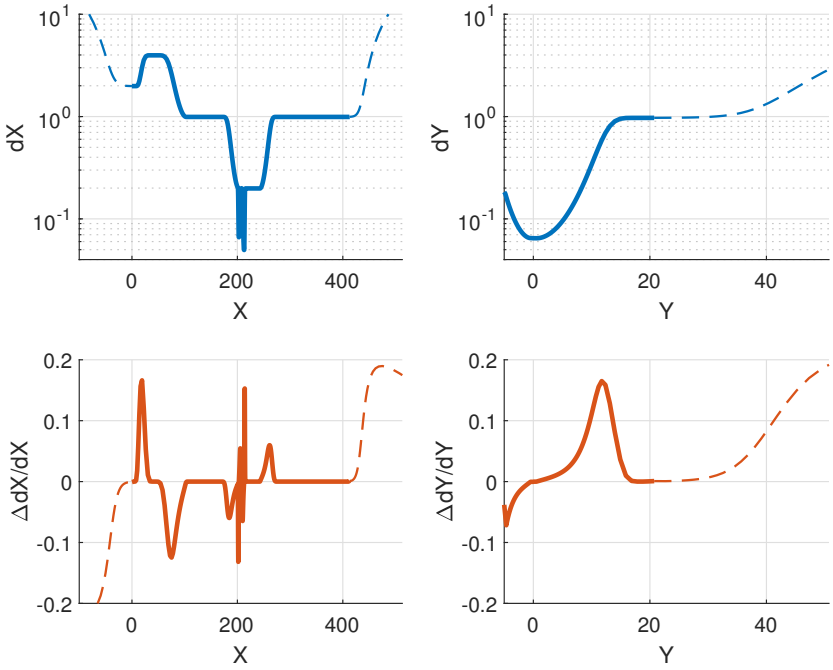

Figure 3.11 – Mesh spacing (top) and relative spacing change (bottom) for X (left) and Y (right) in a gap case. Buffer zones are represented by the dashed lines and are not fully shown for clarity.

3.5 Obtaining a base flow

A base flow is defined as an equilibrium point of the Navier-Stokes equation, it is, when the time derivatives of all variables are null. Such flow is often required as initial state for distinct types of instability analysis and, therefore, must be obtained with great accuracy.

In the case of stable flows, by simply starting the DNS with an arbitrary flow (such as a Blasius boundary layer) and letting it evolve will cause it to eventually reach the

base flow, as all modes will be damped out. This strategy, however, is often very time consuming, especially at the near-critical scenarios we wish to address in this study. On the other hand, if the flow is unstable, it would not reach the base flow naturally, as it is an unstable equilibrium point.

Two techniques are combined to reach a base flow quickly and reliably for both stable and unstable scenarios. The Selective Frequency Damping (SFD) method is used to stabilize any unstable mode present (ÅKERVIK et al., 2006) and a time-averaging process is done in a manner that whole periods of the least stable modes are contained within the window, damping them by roughly an order of magnitude every cycle.

In this code, it is possible to turn on the SFD filter only at selected parts of the domain, where we can maximize its benefits while reducing the possibility it would cause new near-critical modes or slow down the convergence of other modes. For example, by activating the SFD only at the cavity's trailing edge, it is possible to stabilize Rossiter modes by breaking their acoustic feedback mechanism. A similar concept is employed at the buffer zones to damp out any oscillations that might reach the open boundaries and reflect.

We have found the SFD to be most effective when dealing with modes that have high frequencies. Using it to damp low frequency modes requires its Δ parameter to be set too high, which would cause the flow to converge much slower due to the modes relative to the $\bar{\boldsymbol{U}}$ term of equations 3.35 and 3.36. Therefore, for these modes, a time-averaging process is used. We either estimate or measure the period of the least stable low frequency modes and compute the mean flow at the end of every cycle.

A test scenario was established with the following parameters: $Re_{\delta_0^*} = 600$, $L = 15$, $D = 5$, $Ma = 0.5$. Once more, all lengths are normalized by δ^* at the gap leading edge. This is a slightly unstable flow and, therefore, the SFD filter must be used to stabilize it. The initial condition is a Blasius profile on the flat plate and a stationary flow in the gap. Figure 3.12 shows the temporal evolution of stream-wise velocity (U) at three probes, one upstream from the gap ($X = 100$), one just before the gap ($X = 200$) and one downstream from it ($X = 300$). All probes are 1 length unit away from the flat plate. Three types of SFD filter were used: only at the buffer zones, at the buffer zones and at the gap trailing edge and at the whole domain. In all cases, the SFD parameters were $\Delta = 10$ and $\chi = 0.05$.

When SFD was used only at the buffer zones, which represents the physically accurate case, the unstable Rossiter mode was able to grow and reach a limit cycle, while both other cases successfully damped these oscillations. By analyzing the first probe, which is upstream from the gap, when the SFD filter was applied only around the trailing edge, the overall trend of the flow was not affected when compared to the first case, apart from the absence of the Rossiter mode. When the filter was applied to the whole domain,

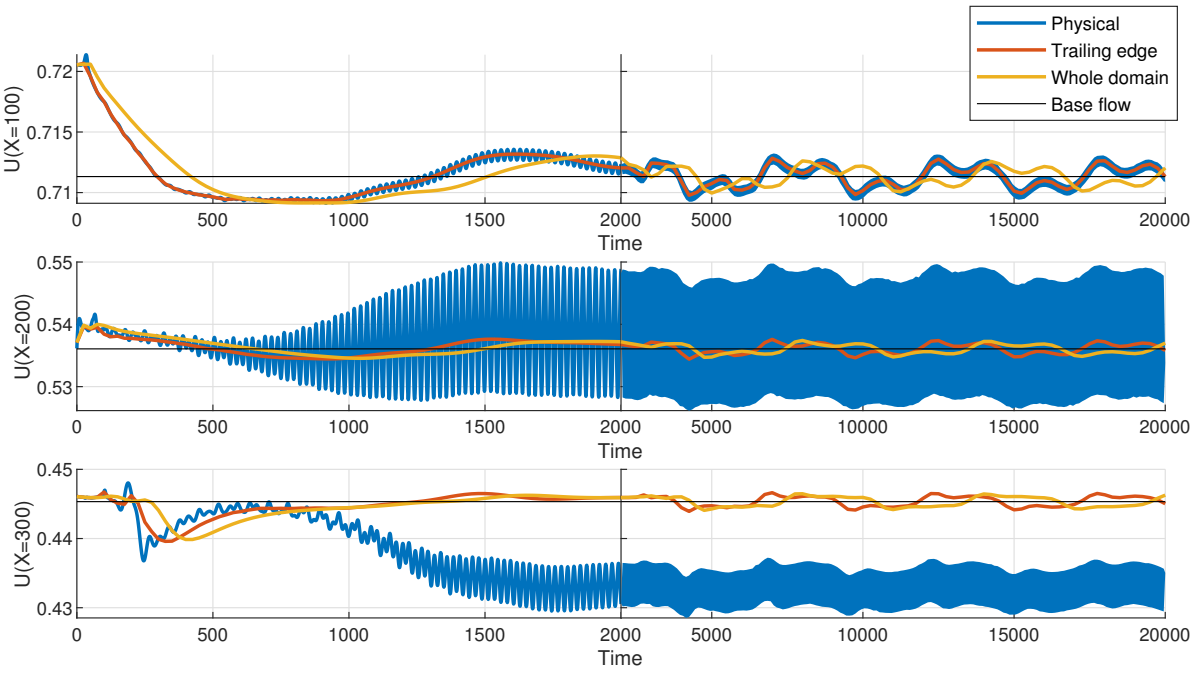

Figure 3.12 – Time series of stream-wise velocity (U) at three probes as the domain evolves from the initial condition towards a base flow for three different SFD strategies: only at the buffer zones (blue), at the buffer zones and at the gap trailing edge (red) and at the whole domain (yellow). Note that the time scale is changed after $t = 2000$ for better visualization of the initial transient phase.

the whole time series was slowed down, and the remaining modes took a longer time to complete a cycle.

The second and third probes present yet another effect, which is the shift of the mean flow due to the limit cycle in the physical case. Once more, turning on the SFD only at the leading edge did not affect the low frequency oscillations in the domain, while using the SFD in the whole domain did.

We have identified this low frequency oscillation as a standing acoustic wave that spans the whole domain in the stream-wise direction. Due to the Dirichlet boundary conditions in one side of the domain and the Neumann boundary conditions in the other, the length of this wave can be estimated as four times that of the domain.

After the flow finishes its initial transient, and assuming all the unstable modes are correctly damped, the remaining oscillations in the domain are caused by this acoustic mode. Due to the very long wave lengths, the buffer zones are not very effective at damping it, which would cause it to oscillate for a long time before dissipating. Damping it with the SFD is also impractical, as the cut-off frequency required would be very low, causing the whole solution to move at a slow pace towards the base flow. Therefore, we use time averaging techniques to damp these modes. When the solution completes a whole cycle of

this mode, the mean flow is computed and the simulation resumes from this new state. Every time the mean flow is computed, the oscillations reduce by about one order of magnitude.

Figure 3.13 shows the residual of the simulation as the baseflow is reached. This residual shows the maximum change for each variable between two consecutive time steps. The SFD filter was turned on at the trailing edge of the cavity. The solution was simulated until $t = 10000$, which is enough for the transient flow to dissipate and for the first acoustic wave cycle to finish. The mean flow is computed, and the simulation resumes until a new acoustic wave cycle is finished, which takes another 6200 time units. This process is repeated until all residuals are in the order of 10^{-13}, which is considered the numerical noise floor for this solver.

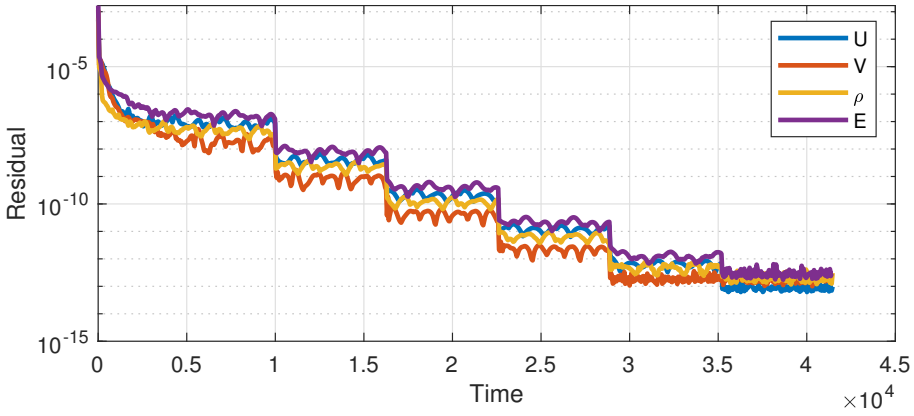

Figure 3.13 – Maximum residual of each variable towards a base flow.

Chapter 4

Linear Stability Theory

4.1 Introduction

Methods for computing the global stability of flows have been used on several applications in the past decades (THEOFILIS, 2011). Many implementations involve building the Jacobian matrix of the flow and solving its eigenproblem. However, starting with Eriksson and Rizzi (1985), who worked with the Euler equations, the alternative, time-stepping method was developed and became popular. Edwards et al. (1994) and Chiba (1998) used this method for the Navier-Stokes equations and Tezuka and Suzuki (2006), to solve a 3D global stability case for the first time. These methods do not require the Jacobian matrix explicitly, but, instead, require a flow solver. An overview of the global stability analysis and other types of modal analysis can be found in (TAIRA et al., 2017).

One reason for the popularity of time-stepping methods is that the flow solver can be treated as a black box, which is simply incorporated into the algorithm, greatly reducing code implementation and verification efforts. Gómez, Gómez and Theofilis (2014) and Liu, Gómez and Theofilis (2016) demonstrated the great flexibility of this method by coupling it to the well-known OpenFOAM CFD software. Time-stepping methods have also been successfully used to solve the adjoint eigenproblem for flow sensitivity analysis (BRYNJELL-RAHKOLA et al., 2017) and for transient growth analysis (BARKLEY; BLACKBURN; SHERWIN, 2008). Mack and Schmid (2010) implement a time-stepping solver and use Cayley transformations to accelerate the convergence of the algorithm in specific parts of the spectrum. More recently, Negi, Hanifi and Henningson (2020) have employed this method for fluid-structure interaction problems. A review of similar methods and its applications can be found in Loiseau et al. (2019). However, if a very large number of eigenvalues is required, the matrix-forming methods are usually more

efficient (THEOFILIS, 2011).

The widely used time-stepping approach discussed in this work is based on the Arnoldi method (ARNOLDI, 1951) for solving eigenproblems. Instead of needing the flow's Jacobian matrix, this method only requires the ability to obtain the product of such matrix by an arbitrary vector. The governing equations are rearranged in a way that the result of this product can be obtained from a run of a flow solver.

In this chapter we investigate parameters that influence the accuracy and cost of this method and develop equations that provide optimal parameter values for its efficient use. We will use the classical open cavity flow as an example. Even though the specific optimal parameters will vary according to, for example, the flow studied, flow solver used and the computational resources available, the trend and sensitivity of the method's performance with respect to each parameter, the guidelines, the equations for estimating optimal values and the conclusions are general.

The chapter focuses on four choices that need to be made when setting up this algorithm: the disturbance magnitude; the Fréchet derivative accuracy order; flow simulation time for each Arnoldi iteration; and the size of the Krylov span. Section 4.2 covers the methods employed in our global stability analysis and explains these parameters and where each of them is needed. As will be explained, even though all these parameters affect accuracy in complicated ways, the optimal value of disturbance magnitude is mostly independent on the integration time and on the size of the Krylov span. In turn, the optimal integration time is also independent on the Krylov span dimension and is only weakly dependent on the disturbance magnitude.

The first two choices are discussed in section 4.4 and are associated to the trade-off between Fréchet truncation errors and flow solver discretization errors. Section 4.5 discusses the effect of the integration time. Section 4.6 analyses the trade-off between the Krylov span size and the integration time of each Arnoldi iteration. Section 4.7 covers the convergence of eigenmodes as well as the contribution of each Arnoldi iteration to the overall result. The last section summarizes the findings.

Goldhirsch, Orszag and Maulik (1987) developed a similar method for obtaining the leading eigenvalues of a large matrix by converting it into a time-dependent differential equation and using this new system to select only the leading modes. They analyzed some sources of errors and part of the current study extends their work. We are concerned with the accuracy in retrieving flow modes. The important topic of the emergence of spurious modes owing to ill-posed boundary conditions is outside our scope; this is discussed by Ohmichi and Suzuki (2016). Our results do not apply to matrix forming methods, whose accuracy and efficiency are analyzed by Gennaro et al. (2013).

Local instability analysis is also used in this work. Since it is nowadays considered

a relatively well-known technique, we refrain from reviewing this topic and describing our implementation. Juniper, Hanifi and Theofilis (2014) describe this technique in detail and present simple codes that can be used to develop research codes.

4.2 Methods

4.2.1 Linear stability computations

A flow evolution can be expressed as

$$\frac{dU}{dt} = f(U) \ , \tag{4.1}$$

where U is a vector that contains all flow variables for each node of a mesh. The flow U is given by the base flow plus a disturbance: $U = U_0 + \tilde{u}$. The known base flow satisfies the steady Navier-Stokes equations, and the disturbance is small. A is the Jacobian matrix

$$A = \frac{\partial f(U_0)}{\partial U} \ , \tag{4.2}$$

hence, after linearizing equation 4.1 around U_0, we obtain

$$\frac{d\tilde{u}}{dt} = A\tilde{u} \ . \tag{4.3}$$

For an initial disturbance $\tilde{u}_0$, the solution $\tilde{u}$ is, formally,

$$\tilde{u} = e^{tA}\tilde{u}_0 \ . \tag{4.4}$$

By computing the eigenvalues S and eigenvectors V of A, equation 4.4 can be rewritten as

$$\tilde{u} = Ve^{tS}V^{-1}\tilde{u}_0 \ . \tag{4.5}$$

Each column ϕ_A of V corresponds to a flow mode and is associated to a value σ_A in S the diagonal matrix of eigenvalues, which gives the mode's amplification rate and oscillation frequency as its real and imaginary parts, respectively. Positive amplification rates indicate instability.

The Jacobian matrix is $N \times N$, where N is the number of nodes in the domain multiplied by the number of dependent variables, namely, 4 for 2D flows and 5 for 3D ones, when using the compressible Navier-Stokes equations; hence the interest in methods that

avoid the solution of the full Jacobian matrix. In the approach used here (ERIKSSON; RIZZI, 1985; CHIBA, 1998; TEZUKA; SUZUKI, 2006; GÓMEZ; GÓMEZ; THEOFILIS, 2014), it is convenient to define a matrix

$$B = e^{\tau A} \ . \tag{4.6}$$

The concept behind the eigenvalue solver method used here is that by recursively multiplying a matrix B by a vector, the eigenvector corresponding to the eigenvalue with the greatest absolute value is selected. Using this idea, it is possible to construct a set of n linearly independent vectors that approximate the eigenvectors of the n largest eigenvalues of B, which correspond to the leading eigenvalues of A. If care is taken, the approximation can be excellent. The method is implemented via the Arnoldi algorithm (ARNOLDI, 1951) and belongs to the class of orthogonal projection techniques for approximate solutions of linear systems (SAAD, 2003).

The Arnoldi algorithm starts with a ℓ^2 normalized vector ζ_1, which will be discussed in the next section. At each iteration k, the Arnoldi algorithm takes a normalized vector ζ_k, and calculates the product $B\zeta_k$. Next, the dot products of ζ_j $(j = 1 \dots k)$ with $B\zeta_k$ are stored in positions $h_{j,k}$ of matrix H. A vector $\tilde{u}_{k+1}$ is given by the Gram-Schmidt orthonormalization of $B\zeta_k$ with respect to all previous ζ_j $(j = 1 \dots k)$. The norm of this vector is stored in $h_{k+1,k}$. The disturbance distribution vector for the following iteration, ζ_{k+1}, is obtained by normalizing $\tilde{u}_{k+1}$. The matrix H is of the Hessemberg form, and is constructed so that (TEZUKA; SUZUKI, 2006)

$$B\left[\zeta_1, \zeta_2, \dots, \zeta_M\right] = \left[\zeta_1, \zeta_2, \dots, \zeta_M\right] \begin{bmatrix} h_{1,1} & \dots & & \dots & h_{1,M} \\ h_{2,1} & \dots & & & \vdots \\ 0 & \ddots & & & \\ \vdots & \ddots & \ddots & \vdots & \vdots \\ 0 & \dots & 0 & h_{M,M-1} & h_{M,M} \end{bmatrix} . \tag{4.7}$$

After enough Arnoldi iterations, the eigenvalues of B, σ_B, with the largest modulus are approximated by the eigenvalues of H. In turn, the eigenvalues of A are $\sigma_A = \log(\sigma_B)/t \approx \log(\sigma_H)/t$, therefore, the eigenvalues of B with the largest modulus correspond to the eigenvalues of A with the largest real part, which are the most unstable and, therefore, usually most of interest in a global stability analysis. The respective eigenvectors are given by $\phi_A = \phi_B \approx [\zeta_1 \dots \zeta_M]\phi_H$. The H matrix is orders of magnitude smaller than the original Jacobian matrix of the flow problem, which massively reduces the computational resources needed. In calculating the eigenvalues of A from those of B, the procedure is ambiguous because the complex logarithm function is multivalued. The imaginary part,

which relates to the frequency, has an undetermined contribution of $2\pi n/\tau$, with n integer. Its value must be verified by, for example, observing the mode oscillation in the flow simulation. This ambiguity of the imaginary part does not affect the accuracy, and often it is the real part that is most vulnerable to discretization errors.

Finally, to multiply B by ζ_k, define F as

$$F(U) = U(0) + \int_0^\tau f(U)dt \ , \tag{4.8}$$

where τ is hereinafter referred to as integration time. The flow $U(t)$ is given by the sum $U_0 + \tilde{u}(t)$, in which $\tilde{u}(0) = \tilde{u}_0$ and $\tilde{u}(\tau)$ is given by equation 4.4. Substituting these in equation 4.8 and $e^{\tau A}$ by B shows that F can provide an approximation for the linear model as:

$$F(U) \approx U_0 + B\tilde{u}_0 \ . \tag{4.9}$$

Hence, B is the Jacobian of F:

$$\frac{\partial F(U)}{\partial \tilde{u_0}} = B \ . \tag{4.10}$$

Using a Taylor series expansion, we can write

$$F(U_0 + \varepsilon_0\zeta) = F(U_0) + \varepsilon_0 B\zeta + \overrightarrow{\mathcal{O}}(||\varepsilon_0\zeta||^2) \ , \tag{4.11}$$

where ε_0 is a small scalar. Keeping in mind that ζ has unitary norm, this leads to

$$B\zeta = \frac{1}{\varepsilon_0}\left[F\left(U_0 + \varepsilon_0\zeta\right) - F\left(U_0\right)\right] + \overrightarrow{\mathcal{O}}(\varepsilon_0) \ . \tag{4.12}$$

$B\zeta$ is the directional derivative of F in the ζ direction, known as Fréchet derivative. Equation 4.12 provides a first-order accurate approximation for $B\zeta$.

A second-order approximation is given by:

$$B\zeta = \frac{1}{2\varepsilon_0}\left[F\left(U_0 + \varepsilon_0\zeta\right) - F\left(U_0 - \varepsilon_0\zeta\right)\right] + \overrightarrow{\mathcal{O}}(\varepsilon_0^2) \ ; \tag{4.13}$$

and a fourth-order:

$$B\zeta = \frac{1}{12\varepsilon_0}\left[-F\left(U_0 + 2\varepsilon_0\zeta\right) + 8F\left(U_0 + \varepsilon_0\zeta\right) - 8F\left(U_0 - \varepsilon_0\zeta\right) + F\left(U_0 - 2\varepsilon_0\zeta\right)\right] + \overrightarrow{\mathcal{O}}(\varepsilon_0^4) \ . \tag{4.14}$$

Most of the literature chooses the second-order approximation (CHIBA, 1998; TEZUKA; SUZUKI, 2006; GÓMEZ et al., 2015), while, for example, Eriksson and Rizzi (1985) used the fourth-order variant. In this chapter this choice is analyzed. The values F to be used in equations 4.12 to 4.14 are obtained by integrating equation 4.1 numerically for a given disturbance $\tilde{u}_0$. This is carried out by the flow solver. The initial disturbance is discussed in the next section and the flow solver used is described later.

Algorithm 1 summarizes the full process.

Algorithm 1

1: Steady state flow U_0 from flow solver
2: Initial disturbance ζ_1 of norm 1
3: **for** k = 1 ... M **do**
4: Compute $B\zeta_k$ using equation 4.12, 4.13, or 4.14
5: $h_{j,k} \leftarrow \zeta_j^T \cdot B\zeta_k \qquad j = 1 \dots k$
6: $\tilde{\zeta}_{k+1} \leftarrow B\zeta_k - \sum_{j=1}^{k} h_{j,k}\zeta_j$
7: $h_{k+1,k} \leftarrow ||\tilde{\zeta}_{k+1}||$
8: $\zeta_{k+1} \leftarrow \tilde{\zeta}_{k+1}/h_{k+1,k}$
9: **end for**
10: Compute eigenvalues σ_H and eigenvectors ϕ_H of H
11: $\sigma_A \leftarrow \log(\sigma_H)/\tau$
12: $\phi_A \leftarrow \{\zeta_1 \dots \zeta_k\}\phi_H$

Two different sources cause most of the errors. One is the Arnoldi algorithm, which uses the reduced order matrix H to approximate the large matrix B. Increasing the number of Arnoldi iterations (M) creates a larger Krylov span which can more accurately reproduce the true modes of the flow. However, τ also affects this approximation, and the product τM is what governs this accuracy (GOLDHIRSCH; ORSZAG; MAULIK, 1987). In sections 4.6 and 4.7, we present results for various values of M and τ and analyze the convergence of different modes.

The other error is the inaccuracy in approximating $B\zeta_k$ in equations 4.12 to 4.14 and can be further divided into two parts: the errors in the Fréchet derivative approximation and errors associated with the evaluation of F via the flow solver. They are affected by the choices of truncation order in the Fréchet derivative, ε_0 and τ. The error in evaluating F is associated with discretization error and nonlinear terms. Naturally, linearized flow solvers are not subject to nonlinear error, such as the one used by Loiseau et al. (2014), however, often the flow solver is not linearized. Sections 4.4 and 4.5 explore these issues and make it clear that some parameters affect more than one source of error.

4.2.2 Initial disturbance

The Arnoldi method efficiency also depends on the initial vector (ζ_1), as modes with a larger contribution to the initial disturbance tend to converge faster. In principle, the initial disturbance should contain all desired modes. However, Goldhirsch, Orszag and Maulik (1987) argue that even if a certain mode is not contained in the initial disturbance, it is likely to appear in the result due to numerical errors.

Random distributions, such as white noise, which have a flat spectrum may be seen as an advantage. However, they excite high-frequency modes, which are soon damped out, resulting in a quick loss of disturbance energy. We used as the initial disturbance a Gaussian distribution centered close to the cavity, where most of the activity takes place. The characteristic lengths in each direction are chosen so that the disturbance approaches zero well before the boundaries of the domain.

Equations 4.12 to 4.14 require the selection of a small scalar ε_0, which is the norm of the disturbance $\tilde{u_0}$ that is added to the flow. It is convenient to also define a parameter ε, such that $\varepsilon = \varepsilon_0/\sqrt{N}$, where N is the total number of variables in the flow solver and remains constant in our study. ε is the RMS of the disturbance $\tilde{u_0}$.

The error when computing $B\zeta$ has two major contributors: the truncation error in the Fréchet derivative and the accuracy of the F approximations. The former is directly linked to the norm of the disturbance (ε_0), while the latter is related to its RMS (ε).

4.2.3 Computational cost

One objective of this chapter is to provide guidelines for accessing efficiency in computing the modes with a desired accuracy. There are several measures of computational cost. CPU time is often used; however, this can be difficult to establish if parallel processing is used. In our case, while most parts of the computational procedures are parallelized, in some of them, notably the eigenvalue solution, the algorithms are closed, and we have limited access to the parallelization level achieved. Moreover, CPU cost is especially important with large clusters shared by many users. In our case, the code was allowed full access to 10 CPU cores of a workstation. Under these circumstances the time to a solution is an interesting measure of cost. This measure was used here and referred to as wall-time; however, as discussed at the end of the chapter, the conclusions can be extrapolated to other measures of cost.

Often a large part of the computational demand comes from the flow solver runs which provides the product $B\zeta$. In our framework, this cost is proportional to the number of Arnoldi iterations M, yielding a computational complexity of $\mathcal{O}(M)$. Some steps involve computational complexities above $\mathcal{O}(M)$; for instance, the Gram-Schmidt

orthonormalization in the Arnoldi algorithm has a complexity of $\mathcal{O}(M^2)$ and the eigenvalue solution of H, despite optimizations that can be used in some cases, tends to $\mathcal{O}(M^3)$ complex. There is also an overhead for transferring data between the flow solver and the global stability solver, as well as an overhead for starting up the flow solver at each Arnoldi iteration. Hence a total cost estimate of the method is given by:

$$C = (C_\tau \, \tau + C_{It}) \, N_{call} \, M + C_{GS} \, M^2 + C_{Eig} \, M^3 + C_0 \ , \tag{4.15}$$

where τ is the integration time; $C_\tau \tau$ is the wall-time the flow solver takes to integrate until τ; C_{It} is the wall-time of calling the flow solver once, which includes the IO operations between the flow solver and the eigenvalue problem solver, and the flow solver startup overhead; N_{call} is the number of flow solver calls to form one column in the Krylov span and depends on the order of accuracy of the Fréchet derivative; C_{GS} is the wall-time of the Gram-Schmidt operation, normalized by M^2. C_{Eig} is the wall-time of computing the eigenvalues of H, normalized by M^3; C_0 includes all other overheads, such as start-up and compilation time, and is fixed and negligible in the scope of this study.

Our Arnoldi algorithm implementation is in MATLAB and uses its built-in parallelization capabilities; the flow solver is written in FORTRAN and is parallelized by MPI. The cost coefficients were estimated with the aid of MATLAB's profiling tool and averaged across many executions with different parameters, in the ranges $100 \leq M \leq 4000$ and $0.01 \leq \tau \leq 10$. Table 4.1 shows these values in seconds. They are highly dependent on the implementation, on the computer and on the specific details of each flow case. Nevertheless, they provide an idea of the order of magnitude of the overall cost and how it scales with the Krylov span dimension, M. In our investigation, the discretization time interval of the flow solver was fixed at 10^{-3}. Moreover, the wall-time is associated to the number of time steps, while, as seen below, the accuracy is mostly related with the integration time τ, that is, the number of time steps multiplied by the discretization time interval. Fixing the discretization time interval makes them proportional. In our flow solver, the time step is upper bounded by the numerical stability of the solution, in the form of the Courant–Friedrichs–Lewy (CFL) condition, and the time integration truncation error at largest stable time step possible is negligible in comparison with the space integration error.

Table 4.1 – Estimated coefficients of computational cost, in seconds

	Value (s)	Complexity
C_τ	10	τM
C_{It}	0.6	M
C_{GS}	$1.5 \cdot 10^{-4}$	M^2
C_{Eig}	$4 \cdot 10^{-10}$	M^3

To illustrate these concepts, figure 4.1 (Top) shows the dimension M of the problem that was possible to construct and solve for $C = 1$ hour and 1 day as a function of τ. For a fixed C, M increases as τ reduces. Also, as a function of τ, the figure displays τM, here called total integration time, which increases with τ. Figure 4.1 (Bottom) gives the fraction of C spent on each part of the procedure. For $C = 1$ hour or for larger values of τ with $C = 1$ day, M is small, and C is dominated by the flow solver. As the Krylov space grows larger, the Gram-Schmidt normalization takes a greater portion of C, as it scales with M^2. Despite having a cost that scales with up to M^3, the time spent computing the eigenvalues of H is still comparatively small in the parameter space searched. For smaller values of τ (thus larger M), the overhead of starting the flow solver also becomes more relevant. This plot considers a first-order accurate Fréchet derivative, but results are qualitatively similar for 2nd and 4thorders.

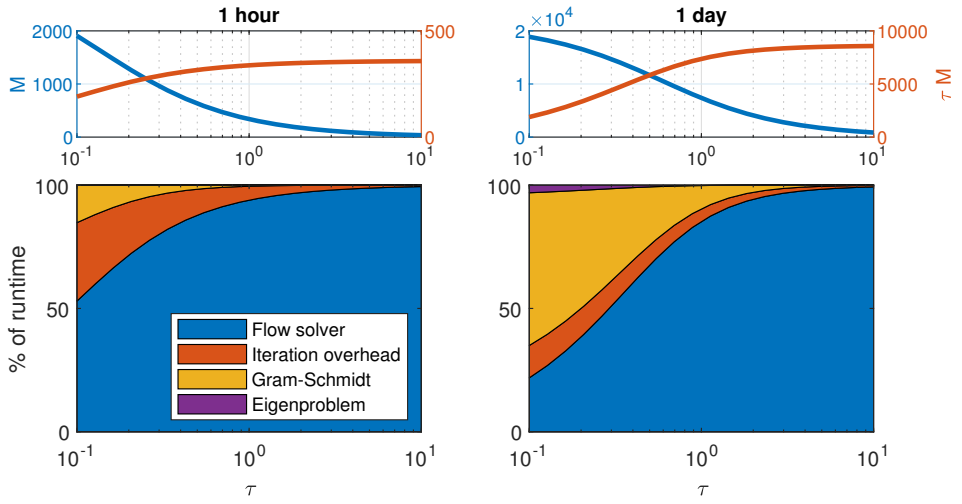

Figure 4.1 – (Top) Number of Arnoldi iterations (M) and total integration time (τM) as a function of integration time τ for two values of C. (Bottom) Fraction of time spent in each part of the procedure.

Restarted Arnoldi techniques (EDWARDS et al., 1994; LEHOUCQ; SORENSEN, 1996; KNOLL; KEYES, 2004; BAGHERI et al., 2009), allow the use of multiple smaller Krylov spans instead of a single larger one, which reduces the total memory usage of the algorithm as well as the cost components that scale super-linearly with M, such as the Gram-Schmidt orthonormalization. As will be seen, with optimal computational parameters these techniques have a limited impact, and, hence, are not investigated here.

Another aspect that may be considered when analyzing the trade-off between τ and M is memory usage. This algorithm requires storing all previous disturbances in memory in the $[\zeta_1 \dots \zeta_k]$ matrix, in our case up to around 2.4 MB per disturbance. However, memory optimization is of greater concern for the matrix-forming strategy (GENNARO et al., 2013), and is outside the scope of this work.

4.3 Baseline results of the studied case

Our test scenario is a flow over a two-dimensional open rectangular cavity. The Mach number is $Ma = 0.5$, Reynolds number based on the cavity depth (Re_D) is 1000 and the boundary layer momentum thickness at the cavity leading edge is given by $D/\theta_0 = 100$. The cavity's aspect ratio is $L/D = 2$. We chose this case as it is well documented and representative of typical cavity instability problems currently under study (BRÈS; COLONIUS, 2008; YAMOUNI; SIPP; JACQUIN, 2013; MATHIAS; MEDEIROS, 2021b). Under these conditions, this flow is unstable. In this work the simulations are two-dimensional as this is enough for our purpose and limits the computational cost. Nevertheless, the conclusion is general and applicable to three-dimensional flows, as discussed in the last section.

The mesh has 340×220 nodes in the stream-wise and wall-normal directions, respectively. The coordinate system origin is at the beginning of the boundary layer, while the cavity leading edge is at (0.23,0). All lengths are normalized by the cavity depth and the density and velocities, by the free-stream values. The useful domain spans from $x = -1$ to 5 in the stream-wise direction and from $y = -1$ to 4 in the wall-normal direction. At the open boundaries of the domain, there is a buffer zone, which progressively increases node spacing and lowers differentiation accuracy order, designed to prevent boundary effects from contaminating the solution. Upstream of the origin, a free-slip condition on the wall was used, which better negotiates the stagnation point at the origin (MARTINEZ; MEDEIROS, 2016). Figure 3.2 shows the domain, the mesh and the boundary conditions. Both base flow and stability results were independent on the computational mesh and domain.

The base flow was obtained using the flow solver with the aid of a Selective Frequency Damping (SFD) filter, which damps modes below a certain frequency threshold (ÅKERVIK et al., 2006). Without such filter, the unstable modes of the flow would prevent reaching a steady state. The SFD filter was turned off during the stability analysis. Figure 4.2 (Top) depicts the base flow in the cavity region, while figure 4.2 (Bottom) shows the base flow convergence history. All residuals are in the order of 10^{-13} relative to free-flow values.

Using the techniques described, the global stability analysis of this flow was performed. Figure 4.3 (Left) shows the eigenvalue spectrum. A positive real part indicates an unstable mode. There are six unstable modes, known as Rossiter modes ($\sigma_{R1} = 0.1344 \pm 1.5276i$, $\sigma_{R2} = 0.3230 \pm 2.7762i$ and $\sigma_{R3} = 0.2672 \pm 3.9143i$) (ROSSITER, 1964; MATHIAS; MEDEIROS, 2021b), and their respective complex conjugates. Also indicated is mode S1 ($\sigma_{S1} = -0.0215 \pm 0i$) the least stable stationary mode, i.e., with a null imaginary part. It relates to the transport of internal energy in the cavity (BERGAMO et al., 2015).

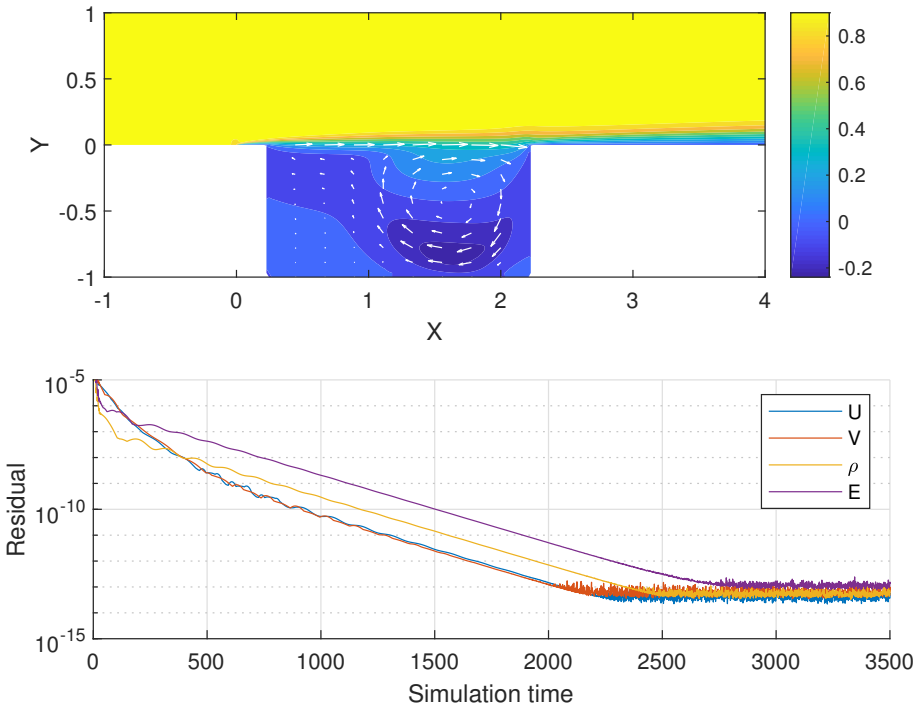

Figure 4.2 – (Top) Streamwise velocity of the base flow (contours every 10% of the free-flow, from -30% to 90%) and velocity field inside the cavity. (Bottom) Maximum residue of each variable as the flow evolves to the steady state.

The right-hand side of the figure shows density contours of these modes, the Rossiter modes at an arbitrary phase. In the following sections, we will use as examples mode R2, the most unstable for this set of parameters and mode S1, which is slightly stable. Their stability results will illustrate the sensitivity analysis and optimal value estimates presented in the following sections.

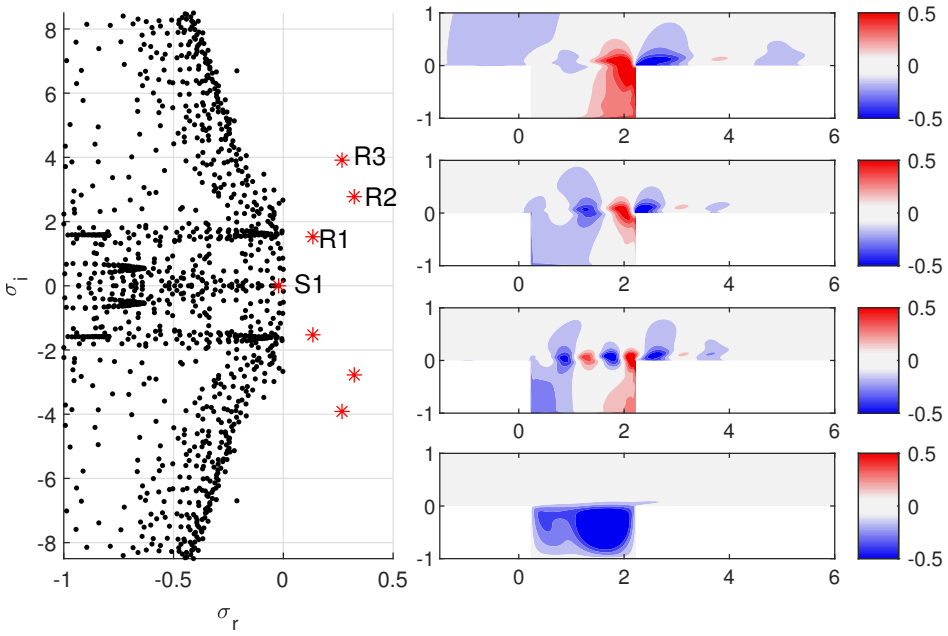

Figure 4.3 – (Left) Eigenspectrum of the base flow, with the unstable Rossiter modes (Rn) and the least stable stationary mode (S1) indicated, (Right) Density contours for the Rossiter modes 1 to 3 and the Stationary mode 1.

4.4 Order of accuracy of the Fréchet derivative and disturbance magnitude

The Fréchet derivative approximates the product $B\zeta$ for the Arnoldi algorithm. In this section we focus on two choices that must be made: the truncation order of the derivative approximation and the magnitude of the disturbance, ε. On the one hand, reducing the disturbance magnitude reduces the truncation error in the Fréchet derivative. On the other hand, owing to the discretization error in the flow solver, reducing the disturbance may deteriorate the approximations of F, as it involves the evolution of disturbances that are several orders of magnitude smaller than the base flow. Moreover, stable modes may attenuate to orders of magnitude smaller than their original amplitude. These aspects advocate the use of high accuracy order methods (LELE, 1992; GAITONDE; VISBAL, 1998; SOUZA; MENDONÇA; MEDEIROS, 2005; SILVA; SOUZA; MEDEIROS, 2010). Often, the flow equations include the nonlinear terms. This may pose another upper bound for ε, but this is strongly dependent on τ and hence is postponed to the next section.

If the truncation error of the Fréchet derivative becomes a limiting factor for the disturbance magnitude, a higher order approximation must be used. This brings the extra computational cost of increasing the number of calls to the flow solver. As an

example, Tezuka and Suzuki (2006) used the second-order method and noted that the effect of changing ε within two orders of magnitude was negligible. This indicates that the discretization error of the flow solver, the nonlinear terms, and the truncation error of the Fréchet derivative were negligible within the range of parameters of that study.

In our study, we tested disturbance magnitudes in the range $10^{-11} \leq \varepsilon \leq 10^{-3}$, combined with different values of τ. Both first and second-order accurate Fréchet derivatives were evaluated. The Krylov span M was so large that, within machine accuracy, the results for the eigenvalues tracked did not change for larger spans.

Figure 4.4 (Left) shows the values of the real part of the R2 eigenvalue obtained with different combinations of parameters. The results are in better agreement with each other in the range $10^{-9} \leq \varepsilon \leq 10^{-6}$. For reference, we performed calculations with $\tau = 1$, $\varepsilon = 10^{-6}$, $M = 2500$ and a fourth-order accurate Fréchet derivative. This Fréchet derivative is more expensive but provides more accurate results. Throughout this study, this case will be called reference case. Figure 4.4 (Right) shows the difference between each case and this reference.

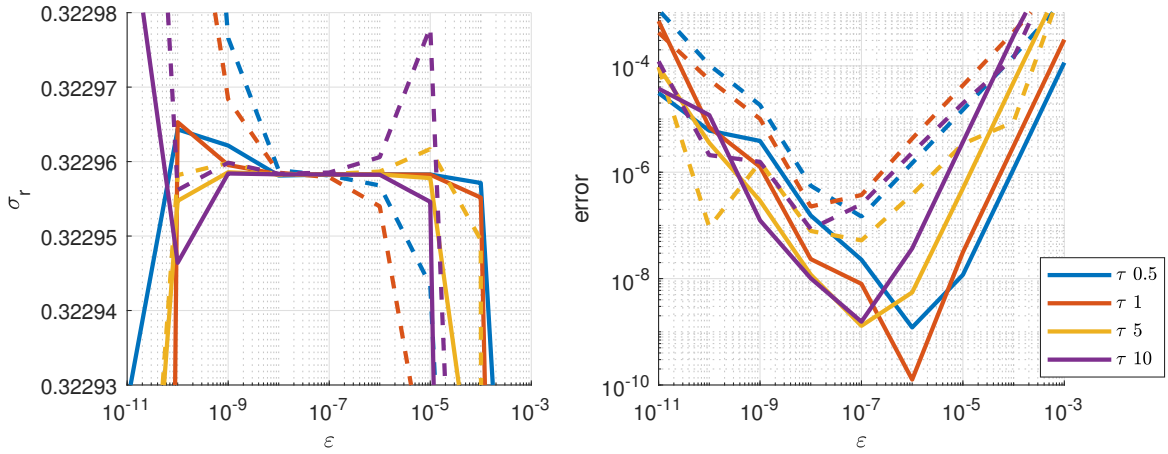

Figure 4.4 – Real part of the R2 eigenvalue as a function of ε for different values of τ. Dashed lines represent first-order accurate Fréchet derivative, and full lines, second-order accurate. (Left) Absolute value. (Right) Difference to the reference case.

From figure 4.4 (Right), in comparison with first-order accurate Fréchet, the second-order one considerably improved the accuracy. For large ε the truncation error dominates and the error decreases as ε diminishes. Accordingly, this is the region most affected by the Fréchet derivative truncation order. Close inspection reveals that, in this region, the error for σ_r decays approximately with either first or second-order, depending on the Fréchet derivative approximation used. This lends support to the approach here used and demonstrates the reference case represents an effective exact solution for the problem.

Also from figure 4.4 (Right), for small ε, the error grows as ε decreases. This

is associated with inaccuracy in the F approximations and originates in the flow solver discretization error. Accordingly, in this region the error is less affected by the Fréchet derivative truncation order. There, the error scales roughly linearly with $1/\varepsilon$, which is the expected scale for this type of error in the estimates of a first derivative like the Fréchet one. For first-order accurate Fréchet derivative the error scaling produces the characteristic "V" shape of the error curve in figure 4.4 (Right).

The maximum accuracy is better than 10^{-8}, but the optimum for $\tau = 1$ is likely to be fortuitous owing to the greater similarity of parameters with the reference case. The minimum error for 2nd order accuracy is about two orders of magnitude lower than for first-order accuracy; however, if an accuracy of 10^{-6} were acceptable, first-order would have produced sufficiently accurate results at about half the cost. For first-order accurate, the optimum ε is between 10^{-8} and 10^{-7}. Consistent with the error scaling discussed above, the optimum ε for second-order accuracy is larger than that of first-order accuracy. The optimum value of ε is lower for larger values of τ due to the nonlinear effects to be discussed in section 4.5.

Figure 4.5 shows the result for mode S1. In general, the same conclusions are reached. Being a stable mode, S1 is more vulnerable to discretization errors in the flow solver. Hence the effect of the discretization error is felt earlier for this mode, slightly raising the minimum error.

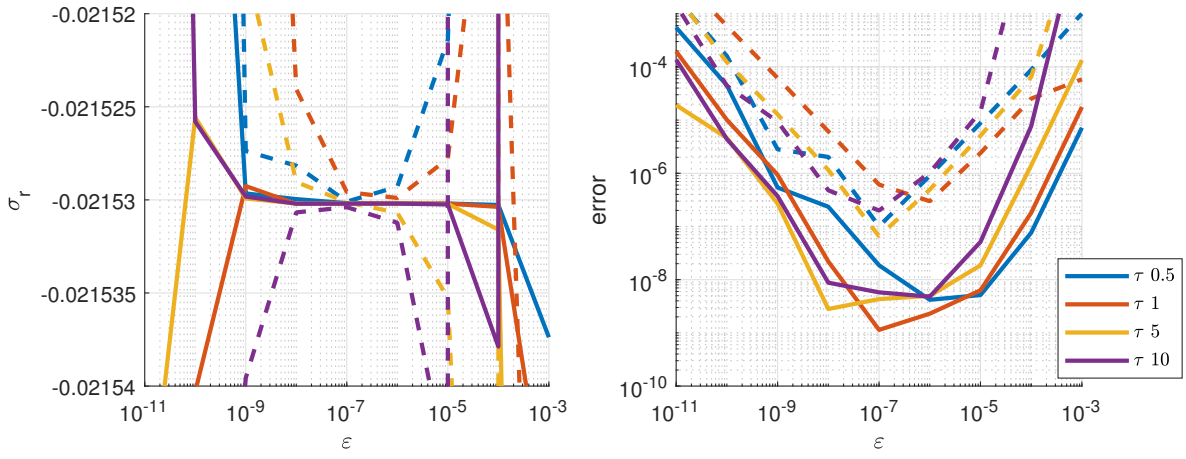

Figure 4.5 – Real part of the S1 eigenvalue as a function of ε for different values of τ. Dashed lines represent first-order accurate Fréchet derivative, and full lines, second-order accurate. (Left) Absolute value. (Right) Difference to the reference case.

Despite the complexity, the error behavior closely follows the theoretical error scaling in the asymptotic range of discretization (SILVA; SOUZA; MEDEIROS, 2010). It is possible to predict the order of magnitude of the optimal ε for a first order accurate Fréchet derivative approximation by replacing the exact solution F by the numerical

solution of the solver in equation 4.11. This introduces all the errors intrinsic to the flow solver. Using $\tilde{F}$ to indicate the numerical solution,

$$\tilde{F}(U_0 + \varepsilon_0\zeta) = \tilde{F}(U_0) + \varepsilon_0 B\zeta + \overrightarrow{\mathcal{O}}\left(\|\varepsilon_0^2\zeta\|\right) + \overrightarrow{E_F} \,, \tag{4.16}$$

where $\overrightarrow{E_F}$ is the error of the numerical approximation of F. Isolating $B\zeta$ (remember that $||\zeta|| = 1$),

$$B\zeta = \frac{1}{\varepsilon_0}\left[\tilde{F}\left(U_0 + \varepsilon_0\zeta\right) - \tilde{F}\left(U_0\right)\right] + \overrightarrow{\mathcal{O}}(\varepsilon_0) + \frac{\overrightarrow{E_F}}{\varepsilon_0} \,. \tag{4.17}$$

It is possible to derive similar expressions for Fréchet derivatives of arbitrary accuracy order n, which we can write in general form as:

$$B\zeta = \delta_n\tilde{F} + \overrightarrow{\mathcal{O}}(\varepsilon_0^n) + \frac{\overrightarrow{E_F}}{\varepsilon_0} \,, \tag{4.18}$$

where $\delta_n\tilde{F}$ is the nth order accurate finite differences approximation for the Fréchet derivative.

The numerical error of F, $\overrightarrow{E_F}$, has two main components: the discretization errors of the flow solver, and the errors caused by nonlinear effects in the flow solution. However, as anticipated, the nonlinear error is neglected in the analysis here and considered in the next section. Each scalar component in the vector $\overrightarrow{E_F}$ has a discretization error of the order of ε_S, which is a measure of the flow solver's error. Therefore, the norm of $\overrightarrow{E_F}$ is $\varepsilon_S\sqrt{N}$, where N is the total number of variables in the system. Replacing ε_0 by $\varepsilon\sqrt{N}$, the total error of $B\zeta$ in equation 4.18 is estimated as

$$E_B = \left\| \overrightarrow{\mathcal{O}}(\varepsilon_0^n) + \frac{\overrightarrow{E_F}}{\varepsilon_0} \right\| = \mathcal{O}\left((\varepsilon\sqrt{N})^n\right) + \mathcal{O}\left(\varepsilon_S/\varepsilon\right) \,. \tag{4.19}$$

The optimum E_B is where $\partial E_B/\partial\varepsilon$ is null, leading to

$$\varepsilon_{opt} = \mathcal{O}\left(\left(\frac{\varepsilon_S}{N^{n/2}}\right)^{\frac{1}{n+1}}\right) \,. \tag{4.20}$$

With $\varepsilon_S = 10^{-13}$, from figure 4.2, we can estimate the minimum error for first-order accurate Fréchet derivative as $\varepsilon_{opt} = \mathcal{O}(10^{-8})$ and for the second-order accuracy as $\varepsilon_{opt} = \mathcal{O}(10^{-6})$. The error scaling involves coefficients which were disregarded, yet the estimates are close to what was observed in figures 4.4 and 4.5.

It is important to note that the theoretical analysis estimates the error in $B\zeta$ while figures 4.4 and 4.5 show the error for selected eigenvalues. Moreover, this equation does

not account for non-linear errors, which occur if both ε and τ are large enough. These issues are best discussed in connection with τ and are, hence, left to the next section. In any case, as will be seen, following the guidelines for use of optimal integration time, the nonlinear error becomes negligible and equation 4.20 is enough to determine the optimal value of ε.

According to equations 4.19 and 4.20, the size of the grid, the discretization error of the flow solver, and the truncation order of the Fréchet derivative approximation affect the optimal disturbance amplitude and the minimal error E_B in different ways. These dependencies are explored in figure 4.6. Regarding the error E_B, higher order Fréchet derivative approximations provide better results, which deteriorate faster with an increase in N or ε_S. For example, if $\varepsilon_S = 10^{-16}$ and $N = 10^3$, going from first order accurate to fourth order accurate Fréchet derivative reduces E_B by 10^6. For a less accurate code and larger grids, say $\varepsilon_S = 10^{-8}$ and $N = 10^7$, the same change reduces E_B by only a factor of 10, even at optimal conditions. This warns that numerical errors associated with less accurate codes in large grids cannot be compensated by higher order accurate Fréchet derivative. About ε_{opt}, high-order accurate Fréchet derivative approximations require a substantially larger ε for optimal performance. Moreover, for low-order accurate Fréchet derivatives, ε_S has a much larger impact on ε_{opt}. This indicates that, for a given grid, the use of low order accurate Fréchet derivatives requires a finer tuning to achieve optimal conditions. On the other hand, for low order accurate Fréchet derivative approximation, the optimal conditions are less sensitive to the grid size N.

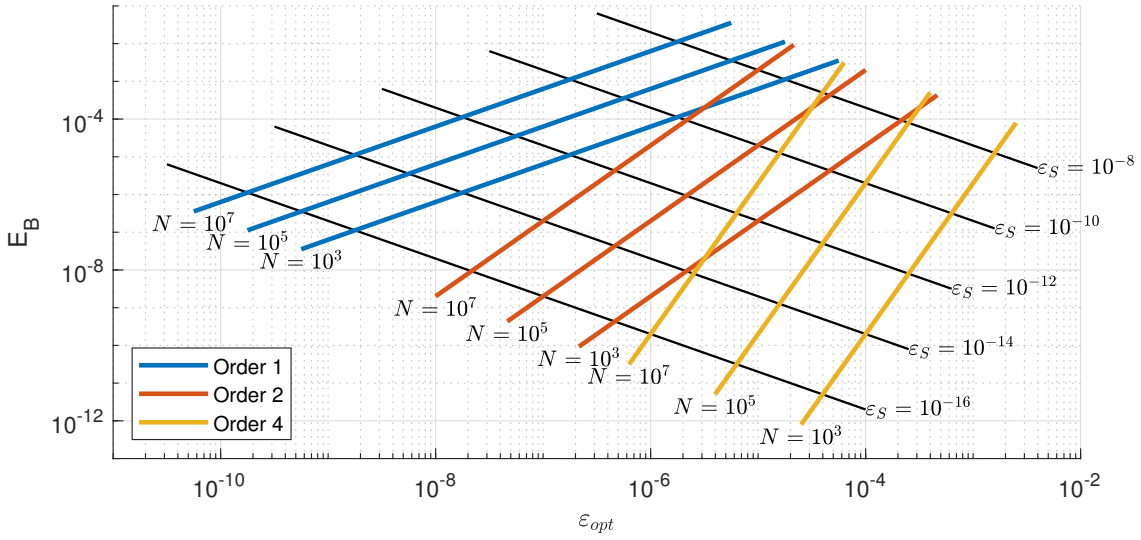

Figure 4.6 – Values of ε_{opt} and the corresponding E_B as a function of ε_S and N for 1st, 2nd and 4th order accuracy Fréchet approximations.

4.5 Effect of integration time length

Another parameter to be chosen when solving the Fréchet derivative to approximate $B\zeta$ is the integration time τ. A larger τ can better isolate one mode from the others within the Arnoldi algorithm; on the other hand, if the integration time is too long, unstable modes may grow sufficiently to develop nonlinear effects, and stable modes may be attenuated enough as to be contaminated by the discretization error of the solver. Small τ also reduces the accuracy of the Fréchet derivative approximations. In this section, we compute the overall error for various values of τ and develop equations for optimal τ. According to Goldhirsch, Orszag and Maulik (1987), every time the flow solver is called, it acts in the direction of filtering the most unstable (or least stable) modes present in the flow; they introduced the concept of filtering time, τM, which we refer to as total integration time. They defined a lower limit for τM as

$$\tau M \gg \frac{1}{\left|\sigma_i^R - \sigma_{M+1}^R\right|} , \tag{4.21}$$

where σ_{M+1} is the eigenvalue to be retrieved in the next iteration and σ_i^R is the real part of the sought eigenvalue, $M + 1 > i$. For a fixed M, equation 4.21 is a lower bound for τ. According to Gómez, Gómez and Theofilis (2014), there is also an upper bound of τ for a stable mode as:

$$\tau \ll \frac{\ln\left(\frac{\varepsilon_S}{\varepsilon}\right)}{\sigma_i^R} , \tag{4.22}$$

where ε is the magnitude of the disturbance added to the base flow and ε_S is the flow solver's discretization error. This limit is associated with the amplitude of the stable mode becoming too small and hence vulnerable to the flow solver's discretization errors.

Figure 4.7 gives both (Left) lower and (Right) upper bounds for τ according to equations 4.21 and 4.22. Lower limits for modes R1, R2, R3 and S1 are presented, but only S1 has its upper limit shown, as equation 4.22 is only valid for stable modes. In our tests, $\tau M = 2500$ (dashed line), which places our simulations well above the lower bounds for all modes considered. The upper bound equation requires ε_S, which is estimated as 10^{-13}, from figure 4.2. The maximum τ used in our study was 50, which places our simulations well below this bound for the range $10^{-11} < \varepsilon < 10^{-3}$ tested.

In practice, however, more restrictive bounds often apply. Moreover, the bounds do not indicate optimum values. To investigate this, we used results similar to those of the previous session but presented in a way to better explore the sensitivity of the performance to the integration time.

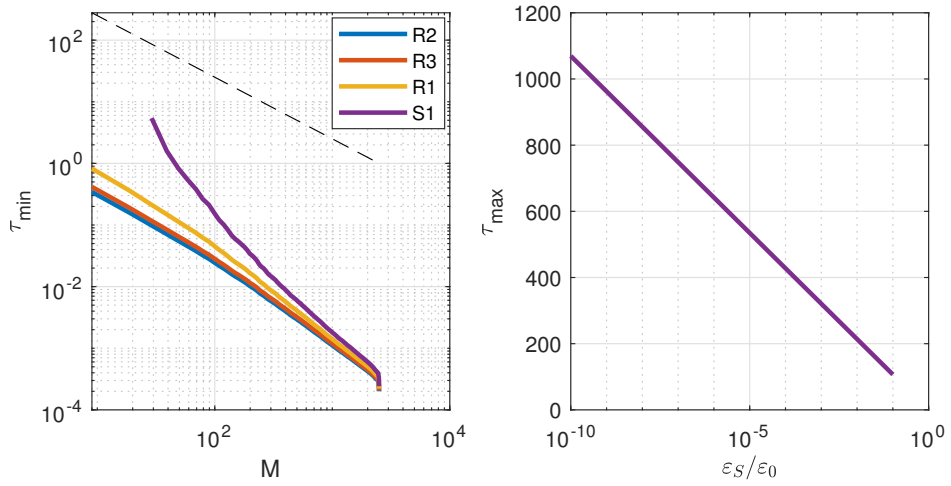

Figure 4.7 – (Left) Lower limit for τ according to equation 4.21. The dashed line represents the product $\tau M = 2500$, which was used in this work. (Right) Upper limit for τ according to equation 4.22.

As seen above, τ can affect the Krylov span approximation as well as the F and the Fréchet derivative approximations. In this section we address only the effect of τ on the F and the Fréchet derivative approximations and therefore we ensured that M was so large as not to affect the results. The effects of M and τ on the Krylov span approximation are discussed in the next section.

Figure 4.8 shows the real part of the R2 eigenvalue for various combinations of τ and ε, with both first and second-order accurate Fréchet derivatives. It also shows the error relative to the reference case. Figure 4.9 shows the same data, but for mode S1. A rapid increase in error is observed on the right-hand side of these figures. This is associated with nonlinear effects in the flow solution as we will discuss. Note, the effective upper boundaries of τ are much more restrictive than those of equation 4.22 even for the stable modes. The error increase for lower τ cannot be linked to the effect described by equation 4.21, as we have chosen a value of M large enough so that it no longer influences the results. This error has a different origin which will also be addressed.

To explain the nonlinear effect, we use figure 4.10. On the left, the figure shows results of the time evolution of the base flow with no disturbances other than the noise floor, which is at the level 10^{-13}. The figure displays the contribution of each mode to the flow as it evolves. These curves were obtained by reconstructing the output from the flow solver from linear combination of all 2500 modes retrieved by the global stability analysis. It is impossible to fully reconstruct the signal unless all modes are available, so we have used a least squares approach to obtain an optimal representation in this limited set. At $\tau = 20$, mode R2 already dominates the flow. However, as early as $\tau = 10$, modes R2 and R3 are present and growing exponentially. Figure 4.10 (Right) shows snapshots of

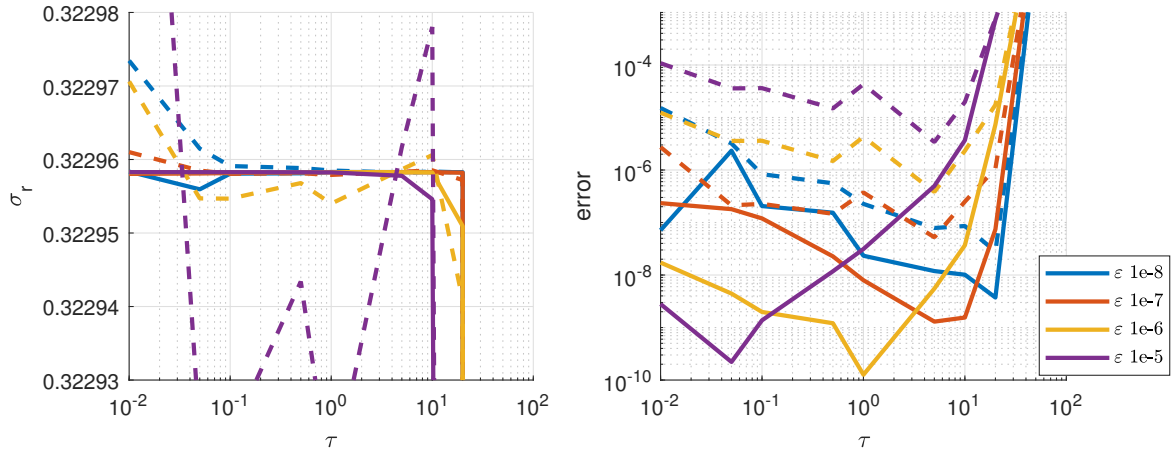

Figure 4.8 – Real part of the R2 eigenvalue as a function of τ for selected values of ε. Dashed lines represent the first-order accurate Fréchet derivative, while full lines represent the second-order accurate derivative. (Left) Absolute value. (Right) Difference to the reference case.

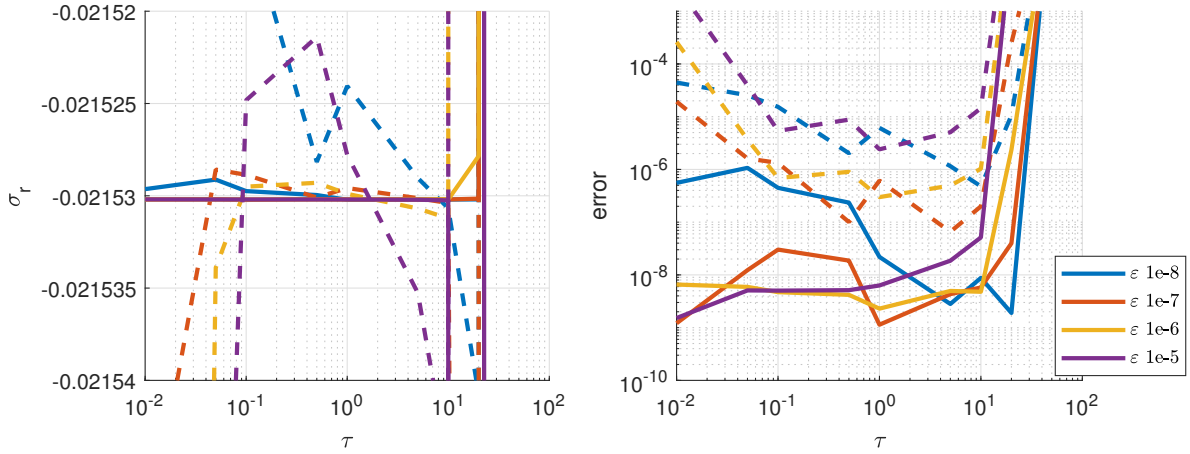

Figure 4.9 – Real part of the S1 eigenvalue as a function of τ for selected values of ε. Dashed lines represent the first-order accurate Fréchet derivative, while full lines represent the second-order accurate derivative. (Left) Absolute value. (Right) Difference to the reference case.

the flow fluctuations along the time evolution, illustrating the emergence of the R2 mode. At $\tau = 50$, the gray lines that depict stable modes start growing as well, until reaching saturation at $\tau = 90$; yet those modes did not become unstable. This is an artifact of the dominant mode's nonlinearity.

An estimate of the magnitude of the nonlinear terms of the disturbance Navier-Stokes equations is the square of the leading mode, formally $\varepsilon^2 e^{2\sigma_1^R \tau}$, which matches the growth rate observed in the figure. As this nonlinear content grows, it contaminates the evolution of the sought modes because the Arnoldi algorithm projects this nonlinear

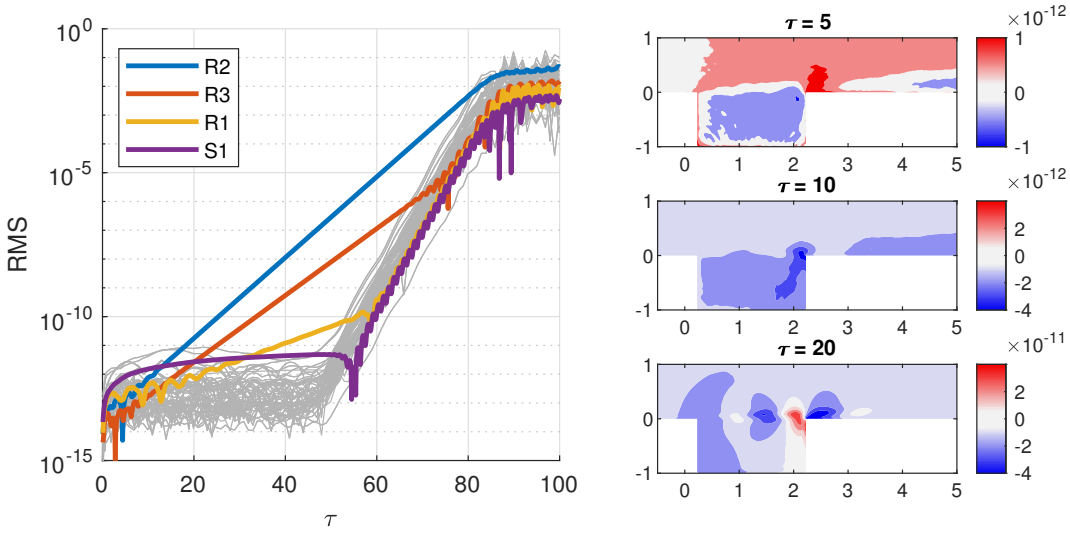

Figure 4.10 – (Left) Evolution of each mode in the flow as it is simulated starting from the base flow without the introduction of any disturbance other than the discretization error. Modes R1 to R3 and S1 are highlighted. Solution projections on the 100th least stable are shown as thin gray lines. (Right) Snapshots of the density fluctuation at $\tau = 5$, 10, and 20.

content onto the linear modes. Even the leading mode R2 is affected, as reflected in the irregular oscillations shortly after the limit cycle is reached. The nonlinear error is, naturally, only present if a nonlinear solver is used. It is relevant only for unstable flows and more critical for large values of τ, when the most unstable modes have enough time to grow and become nonlinear.

Figure 4.11 shows the same analysis as figure 4.10, but for different starting conditions. In the upper row, we added the initial disturbance of the Arnoldi procedure, ζ_1, to the base flow with magnitudes $\varepsilon = 10^{-5}$, 10^{-7} and 10^{-9}. The bottom row uses disturbance ζ_{100}, corresponding to the 100th Arnoldi iteration. Similar results would be obtained if other iterations were chosen. This illustrates the mode evolution within each Arnoldi iteration. In these cases, the nonlinearities surfaced much earlier in the simulation, especially for larger values of ε.

This phenomenon defines an upper bound of τ, which can be estimated as follows. It is required that the mode amplitude be substantially larger than the nonlinear error contamination,

$$\varepsilon e^{\sigma_i^R \tau} \gg \varepsilon^2 e^{2\sigma_1^R \tau} \ , \tag{4.23}$$

leading to

$$\tau \ll \frac{\ln(\varepsilon)}{\sigma_i^R - 2\sigma_1^R} \ . \tag{4.24}$$

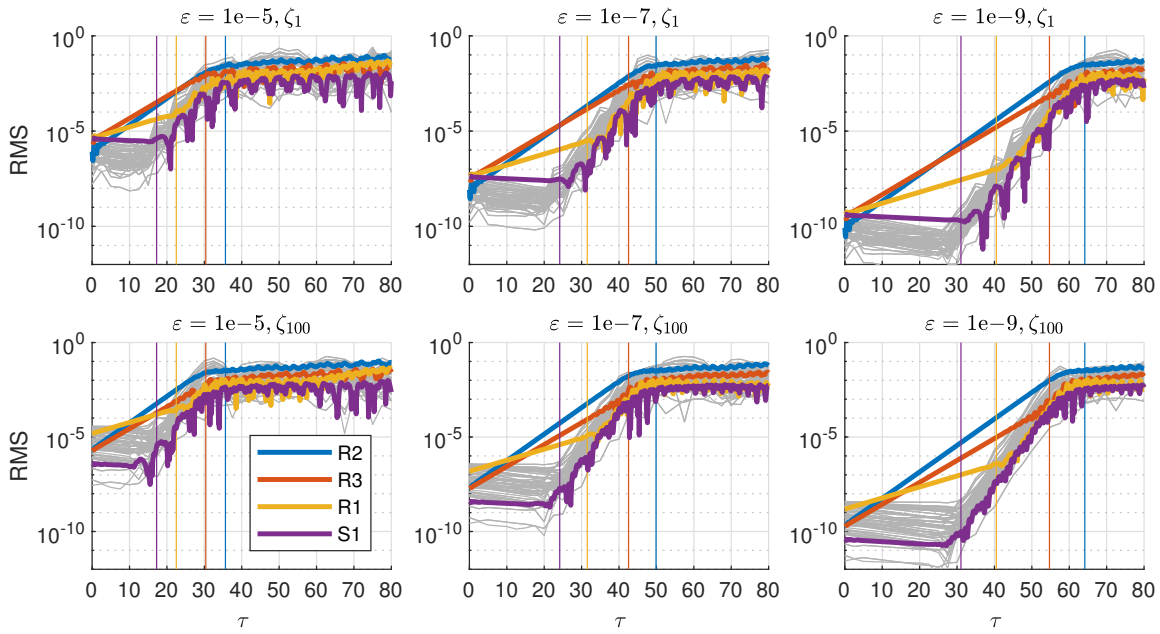

Figure 4.11 – Evolution of each mode in the flow as it is simulated from different starting conditions. Modes R1 to R3 and S1 are highlighted. Modes up to the 100th least stable are shown as thin gray lines. Vertical lines depict the upper limits of τ, as given by equation 4.24.

Using equation 4.24, we computed the τ bounds associated with each mode, represented by the vertical lines in figure 4.11. They offer good estimates of the values of τ from which the linear projection of each mode shows nonlinear effects. This is also the time from which there is a massive error increment in figures 4.8 and 4.9. As seen in these figures, the bounds slightly decrease for more stable and are not affected by the order of accuracy of the Fréchet derivative. The estimates captured consistently the effect of ε and apply for any Krylov iteration. It is important to note that, if there are no unstable modes, these nonlinear effects should reduce with time and the upper bound given by equation 4.22 is likely to be the only constraint for large τ.

As for the lower values of τ, Figures 4.8 and 4.9 show a slow increase in error as τ is reduced. This is associated with the discretization error of the Fréchet derivative approximations, which in turn affects σ_A. If there is not enough time of flow evolution, the finite differences in the Fréchet derivative, become vulnerable to numerical errors of the flow solver.

We developed estimates for an optimal τ as follows. We can include in equation 4.19 the nonlinear error neglected in the previous section, which becomes

$$E_B = \mathcal{O}((\varepsilon\sqrt{N})^n) + \mathcal{O}(\varepsilon_S/\varepsilon) + \mathcal{O}(\varepsilon e^{2\sigma_1^R \tau}) \ . \tag{4.25}$$

From equation 4.6, we have

$$dA = \frac{1}{\tau} e^{-A\tau} dB \ . \tag{4.26}$$

Substituting E_B from equation 4.25 into dB, the norm of the error in A is

$$E_A \approx \frac{(\varepsilon\sqrt{N})^n + \varepsilon_S/\varepsilon + \varepsilon e^{2\sigma_1^R \tau}}{\|\tau e^{A\tau}\|} \ . \tag{4.27}$$

For small τ, the denominator of equation 4.27 can be written as

$$E_A \approx \frac{(\varepsilon\sqrt{N})^n + \varepsilon_S/\varepsilon + \varepsilon e^{2\sigma_1^R \tau}}{\tau} \ , \tag{4.28}$$

which predicts a slow accuracy degradation as τ reduces. The behavior is consistent with the results shown in figures 4.8 and 4.9. As explained above, the error arises in the Fréchet derivative approximations, but is governed by the accuracy of the flow solver and hence we assign it to errors in the F approximations. The rate of increase of error as τ reduces is not dependent on either the Fréchet derivative accuracy order or on ε, as suggested by figures 9 and 10 .

If τ is so large that the leading mode becomes dominant, we approximate$\|e^{A\tau}\|$ by $e^{\sigma_1^R \tau}$, the leading eigenmode, which yields

$$E_A \approx \frac{(\varepsilon\sqrt{N})^n + \varepsilon_S/\varepsilon + \varepsilon e^{2\sigma_1^R \tau}}{\tau e^{\sigma_1^R \tau}} \ . \tag{4.29}$$

This equation is plotted in Figure 4.12 (Left) for various combinations of ε and Fréchet derivative order of accuracy approximations. Figures 4.8 and 4.9 show the error in the eigenvalues σ, while equation 4.29 and figure 4.12 relate to the error in $A\zeta$, which is of the same order of the errors in A itself, as ζ has a unitary norm. However, according to Davis and Moler (1978), when a small disturbance is added to an invertible matrix, its eigenvalues will be changed by an amount whose upper bound is proportional to the norm of said disturbance. Since matrix A is invertible (as it has no null eigenvalue), this explains why E_A and E_σ behave similarly. This also justifies the estimates of optimal ε.

Equation 4.29 can provide estimates of the optimal τ for the dominant mode. However, for less unstable (or more stable) modes, the upper boundary of τ reduces (see figure 4.11) and so would optimal τ. Figures 4.10 and 4.11 indicate that each mode behaves independently from the others regarding nonlinear errors. This observation led us

to an ad-hoc equation that offers good estimates of optimal τ for any given eigenvalue. We simply replace $e^{A\tau}$ by $e^{\sigma_i^R \tau}$ in equation 4.27 for each mode i, yielding

$$E_{A_i} \approx \frac{(\varepsilon\sqrt{N})^n + \varepsilon_S/\varepsilon + \varepsilon e^{2\sigma_1^R \tau}}{\tau e^{\sigma_i^R \tau}} \,, \tag{4.30}$$

where E_{A_i} is meant to indicate the error in matrix A which would affect accuracy of eigenvalue i. For small τ, it reduces to equation 4.28. Also note that, for large τ and stable flows, the equation leads to the upper bound expressed by equation 4.24, as presented by Gómez, Gómez and Theofilis (2014). Figure 4.12 (Right) shows the value of E_{A_i} for Mode S1, while figure 4.12 (Left) can be interpreted as the equivalent for Mode R2. By comparing figure 4.12 with figures 4.8 and 4.9, we observe that equation 4.30 adequately accounts for the reduction of the optimum τ for less unstable modes, see figure 4.11.

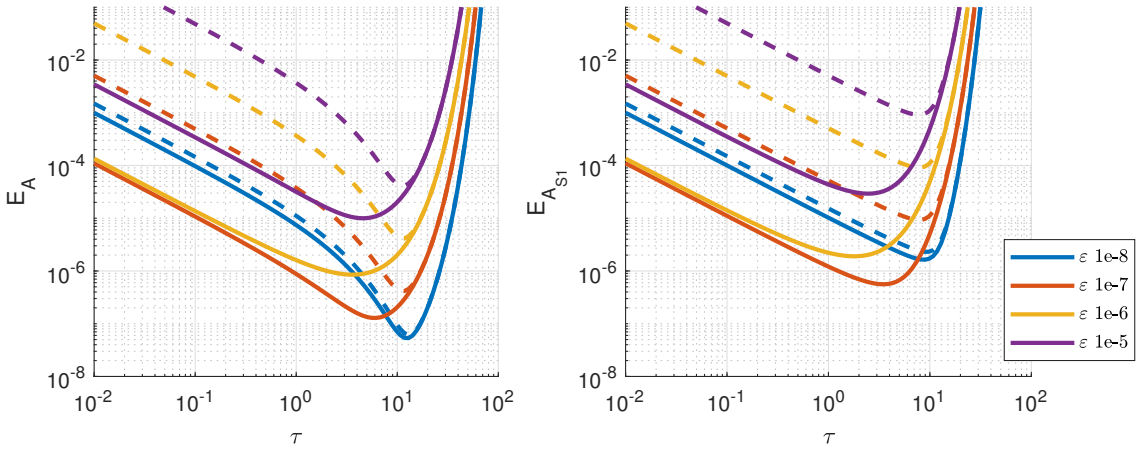

Figure 4.12 – Estimate of the error in $A\zeta$ as a function of τ for select values of ε, (Left) using equation 4.29 and (Right) using equation 4.30 with values corresponding to mode S1. The solid lines represent second order accurate Fréchet derivative approximation and the dashed lines, first order approximation.

An estimate of the eigenvalues is needed as input for equations 4.27 to 4.30, which may not be known a priori. Therefore, it is important to quantify the sensitivity of optimal τ to the eigenvalues. Figure 4.13 (Left) shows the value of E_A for mode R2 for a range of hypothetical values of σ_{R2}^R and τ, as computed by equation 4.30. The actual value, $\sigma_{R2}^R = 0.3230$, is indicated by the black line. Each color represents a different value of Δ_σ, which was added to σ_{R2}. ε was fixed at 10^{-6} and the second order accurate Fréchet derivative was used. The figure shows that the error is much more sensitive to changes in σ when τ is large. Figure 4.13 (Center) shows error estimates for mode S1 as σ_{R2} is changed, while Figure 4.13 (Right) shows error estimates for mode S1 as its own eigenvalue changes.

The figure shows that the value of optimal τ for both the leading mode and the other modes are not very sensitive to the values of neither the leading eigenvalue nor

the sought eigenvalue. Moreover, it shows that choosing a τ smaller than τ_{opt} does not degrade the accuracy substantially and prevents the risk of the very dangerous nonlinear contamination. Therefore, a safe approach is to use a value of τ somewhat smaller than the optimum dictated by equation 4.29; in our study, very good results were produced for τ about 5 times smaller than the upper limit given by equation 4.24.

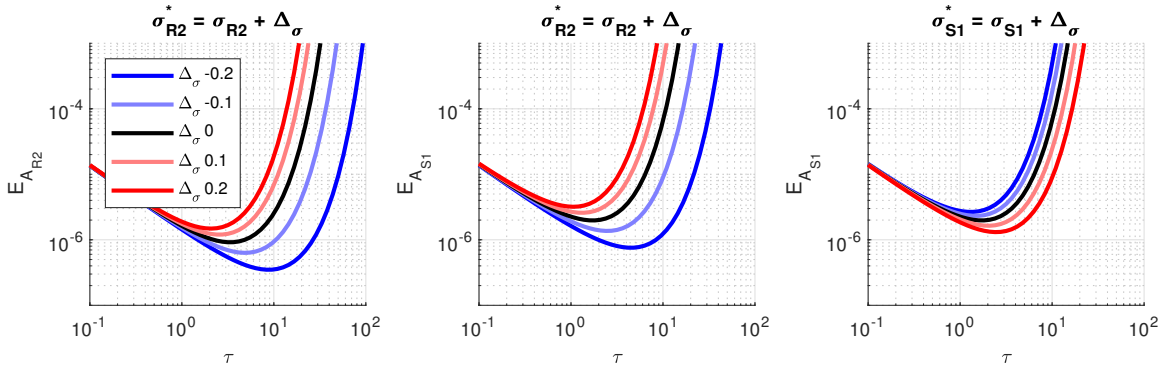

Figure 4.13 – (Left) Values of E_A for mode R2 when the real part of its eigenvalue is changed. (Center) Values of E_A for mode S1 when the real part of the leading eigenvalue is changed. (Right) Values of E_A for mode S1 when the real part of its eigenvalue is changed.

Equations 4.29 and 4.30 comprise not only the effects of τ, but also that of ε and of the order of accuracy of the Fréchet derivative approximation investigated in the previous section. It can be used as follows. Following the guidelines above, it is anticipated that, the error associated with the nonlinear term will be negligible to be on the safe side. Hence, differentiation of either of these equations leads to equation 4.20. With ε_{opt} defined, it is possible to obtain the optimal value of τ from equation 4.30 with a rough estimate of the leading eigenvalue and the most stable eigenvalues sought. Analytically differentiating this equation with respect to τ does not lead to simple expressions, hence we refrain from presenting it. The equation also allows the evaluation of the effect of increasing the order of accuracy of the Fréchet approximations, of reducing the flow solver noise floor and of increasing the computational grid.

It is possible to introduce a renormalization step in the algorithm to increase the maximum value of τ, while keeping the disturbance norm within an acceptable range, away from both nonlinear effects and rounding errors. However, the renormalization of the disturbance would affect all modes equally; for example, reducing the norm of stable modes to keep an unstable mode from becoming nonlinear. In practice, the effect of the renormalization on the error could be estimated by subtracting the real part of σ_1 from all eigenvalues, which can be thought of as forcing the first mode to have neutral stability and adjusting the amplitude of all other modes accordingly. Figure 4.14 shows the predicted error according to equation 4.30 with and without renormalization. In both

cases, the second order accurate Fréchet derivative is used. By using the renormalization, equation 4.30 predicts virtually unlimited accuracy for the first mode for very large values of τ. Naturally, this would not be possible due to rounding errors during the renormalization subroutine, which, however, were not accounted for by the equation.

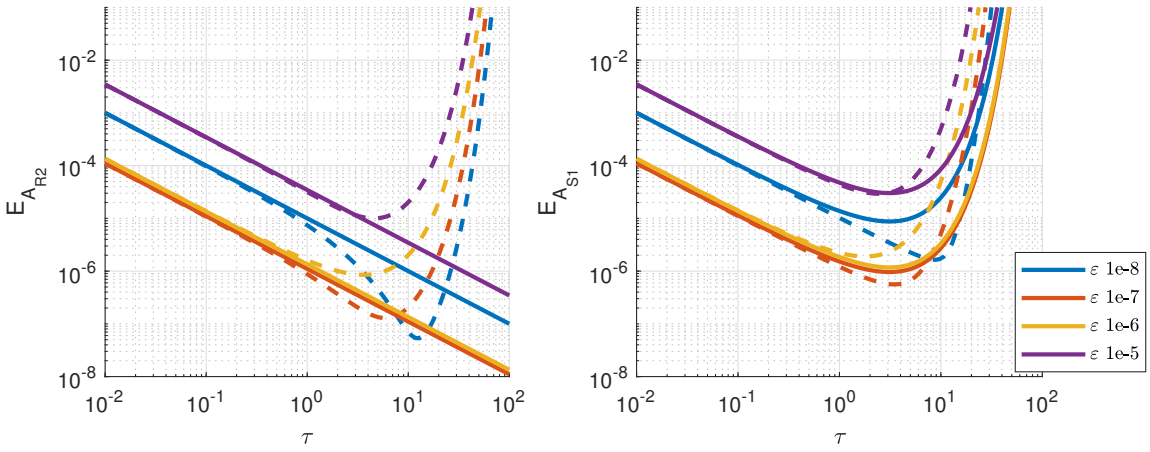

Figure 4.14 – Estimate of the error in $A\zeta$ as a function of τ for select values of ε, using equation 4.30 for modes R2 (Left) and S1 (Right). The solid lines represent the case with renormalization and dashed lines, without.

Figure 4.15 shows the measured error for modes R2 and S1 for various values of τ, with $\varepsilon = 10^{-7}$ and second order accurate Fréchet derivative and compares the regular case to cases that were renormalized at different intervals T_R. This result closely matches figure 4.14, in which there was in increased accuracy in the leading mode at the cost of reduced accuracies for other modes.

In sum, renormalization techniques might mitigate the non-linear effects; however, they carry the added cost of causing non-leading modes to decay into background noise more quickly. In fact, if τ is large enough so that all non-leading modes become negligible in comparison to the leading mode each time the flow solver is called, this method becomes very similar to the Residual Algorithm, presented by Theofilis and Colonius (2003), which is only able to capture the leading mode of a flow.

Nonetheless, for stable flows, i.e., $\sigma_1^R < 0$, renormalization might increase the accuracy of the least stable eigenvalues by keeping them at larger amplitudes. For instance, in a hypothetical flow where the least stable eigenvalues are given by $\sigma_1 = -0.1$, $\sigma_2 = -0.12$, $\sigma_3 = -0.2$, equation 4.30 predicts the values shown in figure 4.16. In this scenario, eigenvalues that are very close to the least stable mode, such as σ_2, have a slightly increased accuracy. However, the benefits of renormalization only appear at very high values of τ, which might hinder the ability to accurately retrieve the imaginary part of the eigenvalues, due to the multivalence of the complex logarithm function, which adds an undetermined contribution of $2\pi n/\tau$, with n integer, to the imaginary part. As τ grows

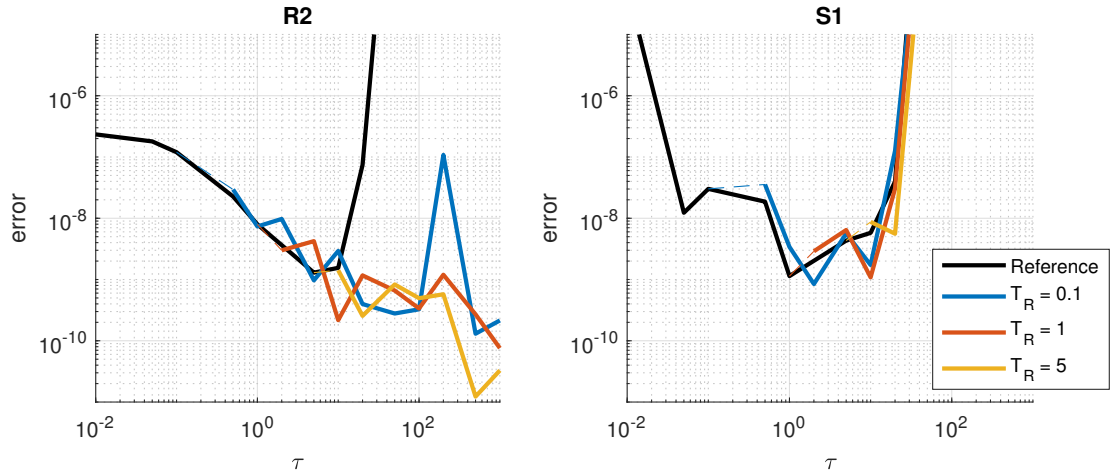

Figure 4.15 – Difference in the real part of the eigenvalue corresponding to modes R2 (Left) and S1 (Right) as a function of τ for $\varepsilon = 10^{-7}$ and second order accurate Fréchet derivative. The black line is the reference case, with no renormalization and the colored lines represent different intervals of renormalization.

larger, the distance between consecutive candidates for the imaginary part reduces, making it difficult the compute the value of n.

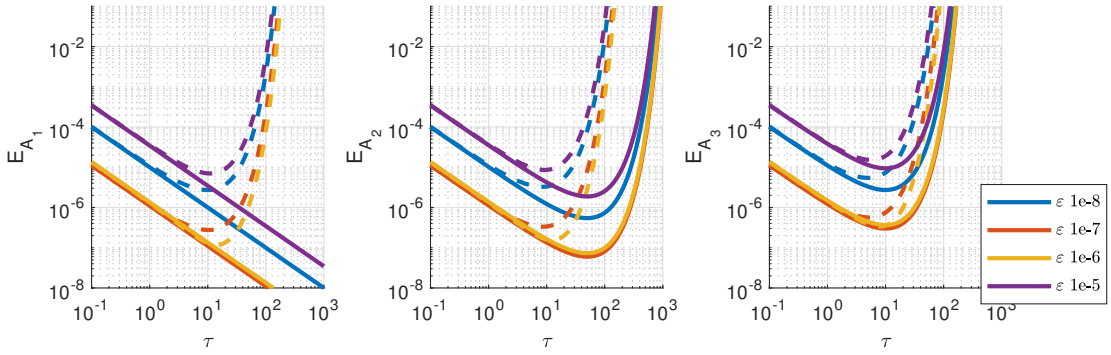

Figure 4.16 – Estimate of the error in $A\zeta$ as a function of τ for select values of ε, using equation 4.30 for a hypothetical flow with the least stable eigenvalues given by $\sigma_1 = -0.1$, $\sigma_2 = -0.12$, $\sigma_1 = -0.2$. The solid lines represent the case with renormalization and dashed lines, without.

4.6 Krylov span dimension and optimization of the total computational time

Following Goldhirsch, Orszag and Maulik (1987), the origin of the lower boundary for τM (equation 4.21) is the error caused by truncating the eigenspectrum to the first M

modes, which is

$$Error \propto \left| e^{(\sigma_{M+1}-\sigma_1)\tau M} \right| . \tag{4.31}$$

This reflects the observation that, in case the growth rates are too close to each other, the total integration time (τM) must be long enough for a mode to be properly identified, hence the boundary. At a glance, it may seem that any combination of τ and M that gives the same total filtering time (as they refer to τM) would produce the same level of accuracy. Nevertheless, increasing M has the additional benefit of moving σ_{M+1} further to the left of the spectrum, hence further reducing this type of error. This suggests that increasing M instead of τ is more cost effective. However, as discussed in section 4.2.3, for large values of M the cost tends to increase nonlinearly with M.

Hence there remains the question of the optimal balance between τ and M that allows the required modes to be retrieved with the desired accuracy and lowest C. With this goal, we mapped the error for various combinations of τ and M, for $\varepsilon = 10^{-6}$ and for first and second-order accurate Fréchet derivatives. Figures 4.17 and 4.18 give the results for modes R2 and S1, respectively. The colored contours indicate iso-levels of error relative to the reference case. The white area for large τ and M was not covered in the study, while in the white areas for small M, the algorithm did not find the sought mode. The solid light gray lines are isocontours of computational cost, as computed by equation 4.15 with the coefficients from table 4.1. From left to right, they represent 5 minutes, 10 minutes, 30 minutes and 1 hour of wall-time, excluding start-up time which is independent of τ and M. The dashed gray lines indicate constant values of $t = \tau M$. Note that, contrary to the previous two sections, this section also addresses the issue of computational time required for a given accuracy and as such the numerical results are dependent on the speed of the flow solver, the efficiency of the eigenvalue problem solver and the computational resources. Nevertheless, the conclusions still serve as general guidelines for improving solution efficiency.

Consistent with Goldhirsch, Orszag and Maulik (1987), in both figures 4.17 and 4.18, the error is larger if the product τM is small. The bounds for τ discussed in the previous section are also observable in the figures. At large τ there are the nonlinear effects which rapidly reduce accuracy. At small τ there is a gradual reduction in accuracy at large M.

Both figures illustrate interesting aspects of the trade-off between τ and M. For $M < 20$, iso-accuracy lines approach the vertical, indicating that, in this region, increasing M is more beneficial than increasing τ. This may be a manifestation of the extra benefit of increasing M discussed in connection with equation 4.31. However, at least for the unstable mode, figure 4.8 suggests this may also be a manifestation of errors associated with nonlinear effects caused by large τ. Away from this region, the extra benefit of

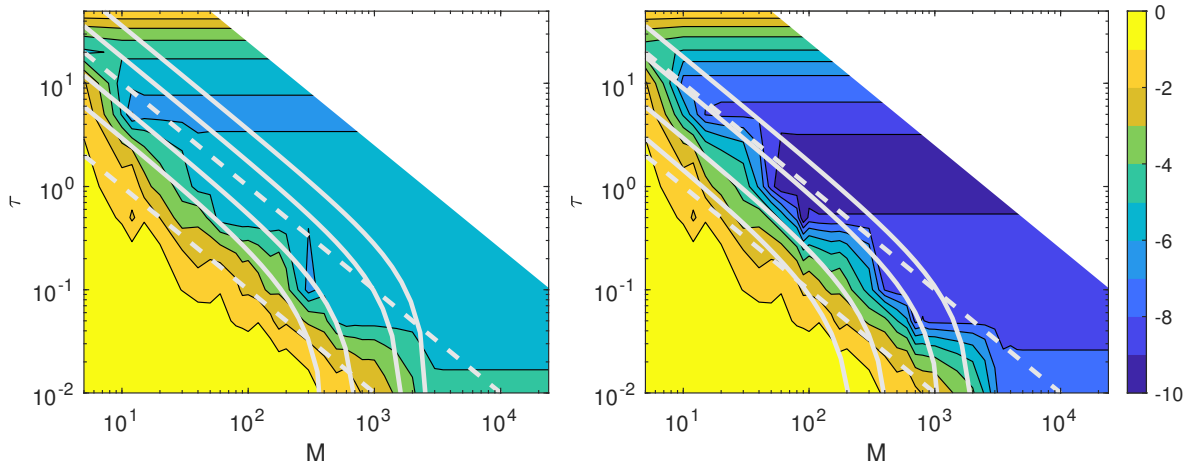

Figure 4.17 – Isocontours of $\log_{10}$(Error) of the real part of the R2 mode, using $\varepsilon = 10^{-6}$. The full gray lines represent a constant computational cost of 5 minutes, 10 minutes, 30 minutes and 1 hour from left to right. The dashed gray lines indicate constant $t = \tau M$. (Left) First order accurate Fréchet derivative. (Right) Second order accurate Fréchet derivative.

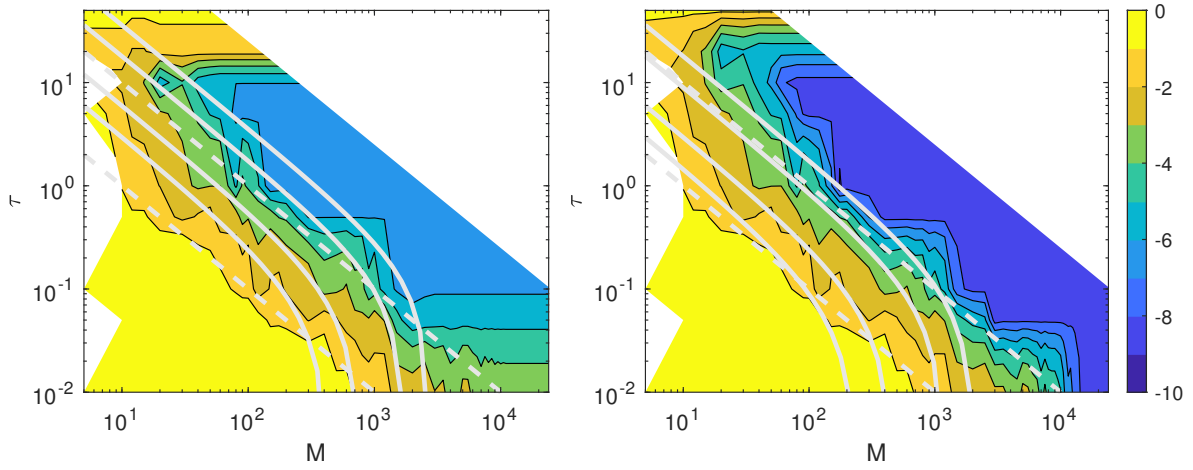

Figure 4.18 – Isocontours of $\log_{10}$(Error) of the real part of the S1 mode, using $\varepsilon = 10^{-6}$. The full gray lines represent a constant computational cost of 5 minutes, 10 minutes, 30 minutes and 1 hour from left to right. The dashed gray lines indicate constant $t = \tau M$. (Left) First order accurate Fréchet derivative. (Right) Second order accurate Fréchet derivative.

increasing M does not appear to be relevant.

In a large central portion of the figures, the curves of iso-cost are roughly parallel to the constant τM lines. This corresponds to the region were the cost of running the flow solver dominates the computations, see figure 4.1. At large M, the cost increases massively, becoming almost independent of τ. It must also be considered that this argument disregards the fact that increasing M has the added benefit of retrieving more modes; that is, we assumed a given set of eigenvalues is desired.

The results indicate that the most cost-effective approach is to use a total integration time τM with the largest τ possible that is still below the upper bounds established, which, from section 4.5, tends to provide better accuracy. Under these circumstances the cost is mostly that of running the flow solver. We recall that the cost was measured by wall-time, which, in our solver, is essentially proportional to CPU time; hence, similar conclusions would have been reached if either were the measure of cost. Therefore, optimal τ does not depend on M, which once more removes one dimension of the parametric search. After establishing ε and τ from the equations of the previous sections, we should run the Arnoldi algorithm and monitor the solution for increasing M until the desired accuracy or minimum error bound is reached. As opposed to τ and ε, M does not need to be decided in advance and its effect on the solution can monitored as the algorithm runs. Our study was restricted to 2D simulations. For 3D simulations, the wall-time or CPU-time associated with the flow integration would be substantially longer and the conclusion would still hold.

Restarted Arnoldi methods considerably reduce the cost associated with the Gram-Schmidt orthonormalization, but, as long as the cost is dominated by the flow solver, this strategy would not be beneficial. This is the situation in our test case, and reason restarted methods were not considered here as it would not affect the optimal parameters. For 3D simulations the CPU-time associated with the flow solver tends be even longer and even less likely to benefit from restarted algorithms. Overall, our results suggest that a wide range of applications would not benefit from restarted algorithms.

The similarity between both frames in each of the figures 4.17 and 4.18 for contour levels down to 10^{-5} is remarkable. This indicates that, for these error levels, the truncation order of the Fréchet derivative does not play a role, as discussed in section 4.4. There is an exception for very small τ, for which there is an effect of the truncation error on levels above 10^{-5}, which is consistent with section 4.5. Hence, under these circumstances, the first-order is the most efficient approach as it requires shorter computation times for the same accuracy. On the other hand, first-order accuracy could not reach an error level below 10^{-6}, while second-order accuracy consistently provides errors of 10^{-8}. This is more clearly illustrated and extended for other eigenvalues in Figure 4.19 which shows the eigenvalue convergence history for first and second-order accurate Fréchet approximations, and for different integration times.

Overall, the results show that, for this problem, if the target error level is about 10^{-5}, first-order is the better choice, whereas, if errors below 10^{-6} are required, at least second-order accurate Fréchet is needed. It should be added that $\varepsilon = 10^{-6}$ is optimal for second order accurate Fréchet derivative approximations, and suboptimal for first order; therefore, it is possible that slightly more accurate results would still be possible with first order. In the choice of the target accuracy, one must also consider that, for open flow

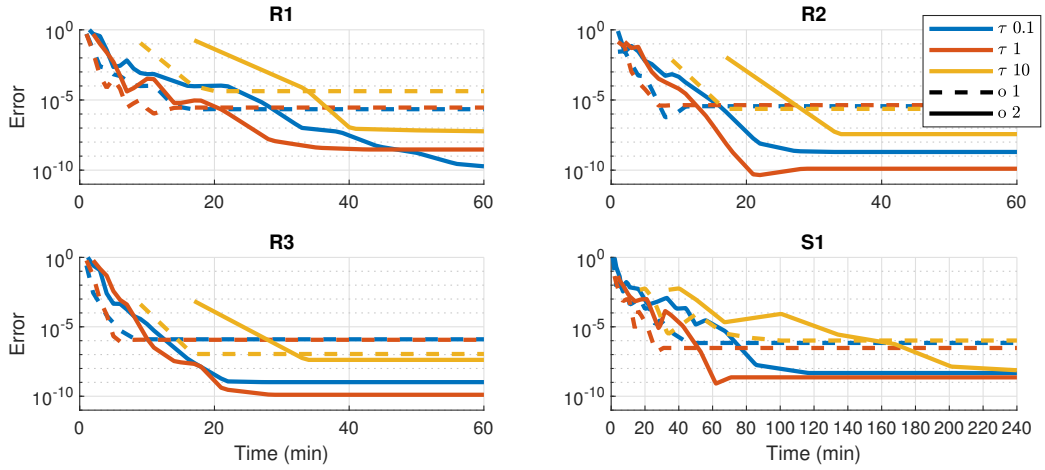

Figure 4.19 – Error of the first four eigenvalues as computational time is increased. $\tau = 0.1, 1, 10$, $\varepsilon = 10^{-6}$. Note that the time scale for mode S1 is different than that of modes R1 to R3.

applications, for example, details of the far field boundary conditions can easily affect the computation of leading eigenvalues in the range of 10^{-5} or above (OHMICHI; SUZUKI, 2016).

4.7 Rate of convergence of eigenfunctions and eigenvalues

In this section, we seek to evaluate how the accuracy of the eigenfunction estimates is affected by the parameters chosen, as well as how it affects the eigenvalue convergence rate. Figure 4.19 shows that the more unstable modes reach minimum error progressively faster. In fact, for mode S1, the error starts decreasing consistently only after all unstable modes have approached their minimum error values. This is associated with eigenfunction representation in the Krylov subspace, as we will discuss. Hence, it is important to investigate the accuracy of the eigenfunction estimates.

Figures 4.20 and 4.21 show the error of the eigenfunctions retrieved for modes R2 and S1, respectively. This error is computed as the mean absolute difference between an eigenfunction and its reference, both eigenfunctions have unitary norm ℓ_2. Using the absolute value of the eigenfunction, our results are unaffected by differences in the eigenfunction phase. The white areas close to the corners of the figures were not included in our parametric sweep.

Consistently, the parameters leading to most accurate eigenvalue results worked for the eigenfunctions as well. Looking at mode R2, the eigenfunction reaches an accuracy of up to 10^{-9} with a first-order accurate Fréchet derivative and up to 10^{-11} with a second-order one. Mode S1 reached an accuracy 10^{-7} with a first-order accurate derivative, while

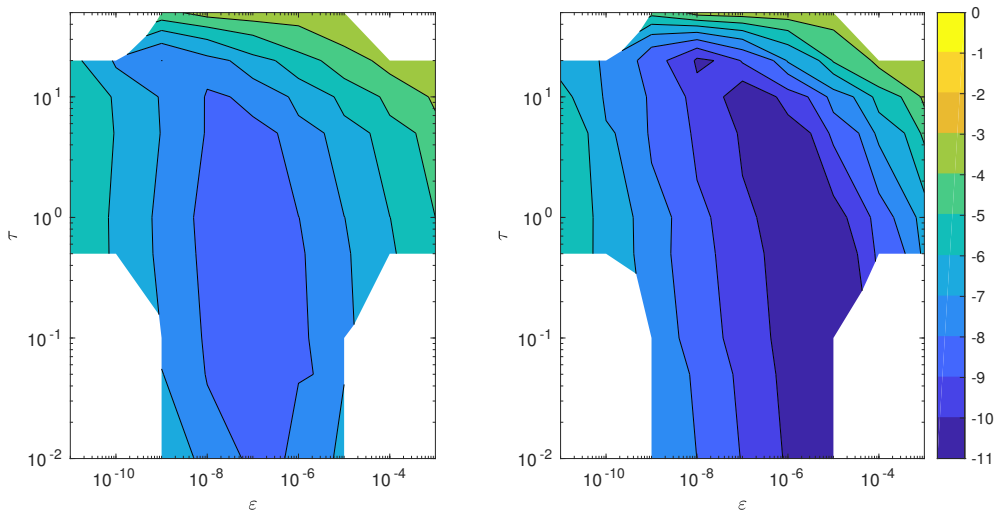

Figure 4.20 – Isocontours of $\log_{10}$(Error) of the eigenfunction of R2 for (Left) first-order accurate Fréchet derivative and (Right) second-order derivative.

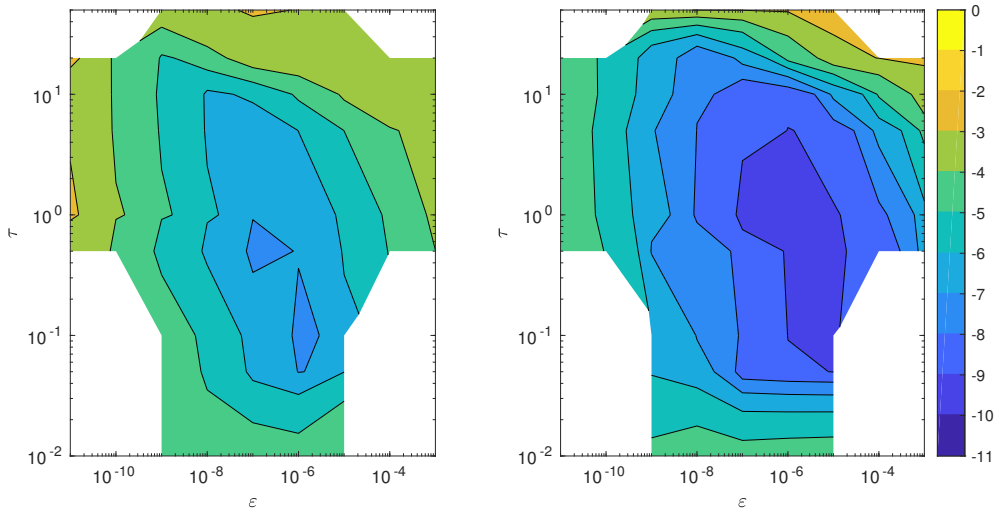

Figure 4.21 – Isocontours of $\log_{10}$(Error) of the eigenfunction of S1 for (Left) first-order accurate Fréchet derivative and (Right) second-order derivative.

the second-order one achieved 10^{-9}.

In some ways, these pictures summarize results obtained for the eigenvalues too. At large τ there are nonlinear effects that affect the accuracy. For small τ and small ε the computation of F becomes vulnerable to the discretization error. For large ε, there are both nonlinear and Fréchet derivative truncation errors, while, at low ε, there are discretization errors in F. Because of these effects, the region of maximum accuracy lies at the center. For second order accurate Fréchet derivatives, the truncation error reduces more rapidly, such that for this case the optimal region moves to the right as compared to the first order accurate one.

In the time-stepping method discussed, the eigenfunctions of each flow mode are retrieved as a linear combination of ζ_i, that are the initial disturbances in each iteration of the Arnoldi procedure. The weight of each ζ_i is given by the eigenvectors of matrix H, as per step 12 of Algorithm 1. By examining the eigenvectors ϕ_H, we can infer how much each iteration contributes to the convergence of a mode. Figure 4.22 shows $|\phi_H|$ as a function of M for R1, R2, R3 and S1 in our reference case. The most unstable modes converge faster. After a mode reaches convergence and therefore can be accurately filtered out of the flow by the Gram-Schmidt orthonormalization, the convergence rate of the next one is accelerated. This is because the converged mode can be accurately removed from the next disturbance by the Gram-Schmidt algorithm, which hence concentrates on filtering of the next dominant mode. It must also be added that modes which are almost orthogonal are expected to have smaller effects on each other. This is possibly an explanation for the faster convergence of mode R3 relative to R1. The convergence of the eigenfunction closely follows, and explains, the convergence of eigenvalues in figure 4.19.

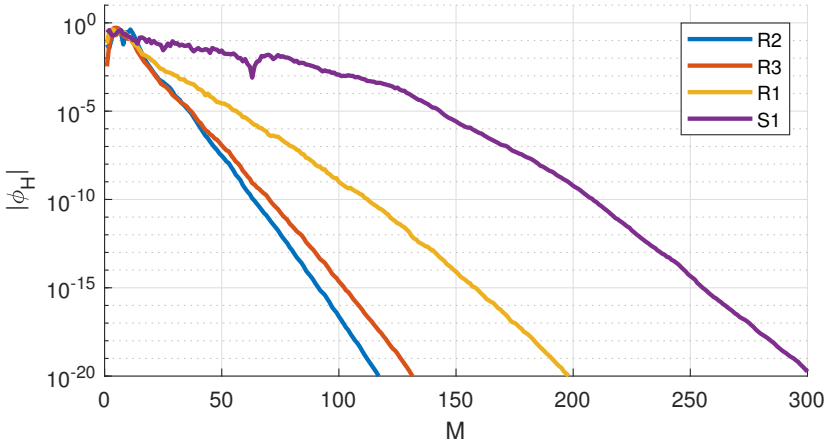

Figure 4.22 – Weight of each disturbance ζ_i in the eigenfunctions of modes R1, R2, R3 and S1.

4.8 Conclusion

We sought to establish guidelines for choosing computational parameters when performing a time-stepping, Jacobian-free global instability analysis of a flow. This procedure requires a solver that produces a flow solution, F. The computational parameters considered were disturbance magnitude (ε), order of accuracy of the Fréchet derivative approximation (n), integration time (τ) and dimension of the Krylov span (M). The analysis was carried out with codes developed in-house and used a two-dimensional compressible open cavity flow as an example; however, these guidelines should be valid for other types of flows and solvers, including three-dimensional scenarios. The following

sources of error may exist in this problem: (1) truncation error associated with the Fréchet derivative approximations; (2) discretization errors in the computation of F, which can be truncation or round-off; (3) errors associated with the nonlinear terms of the Navier-Stokes equations; and (4) errors associated with the Krylov subspace approximation. Parameter n affects the truncation error (1). Parameter ε affects the truncation (1), discretization (2) and the nonlinear (3) errors. Parameter M affects the Krylov subspace approximation (4) only, while parameter τ affects all errors.

In principle, the choice of ε, τ and M constitutes a search in a three-dimensional space. However, our analysis demonstrated that optimal τ must correspond to effectively negligible nonlinear terms. This led to the optimal ε being independent of τ and M, which reduces one dimension in the parametric search. The analysis also showed that optimal τ is independent on M and leads to the most cost-effective choice of τM, which reduces another dimension in the parametric search. Hence, as a guideline, one must first determine ε_{opt}, next τ_{opt} and finally M. M does not need to be known a priori and can be monitored along the Arnoldi iterations at no cost.

It was further found that optimal values of ε depend on a balance between truncation error (1) and discretization error (2) and can be estimated a priori by equation 4.20. Equation 4.19 can be used to evaluate the benefit of increasing the accuracy order of the Fréchet derivative approximations, the consequences of using less accurate flow solvers, and the care that must be taken when large grids are employed.

Our analysis shows that optimal values of τ can be established primarily based on its impact on the error associated with computing F and the Fréchet derivative, disregarding its impact on the Krylov span approximation. Under these circumstances, optimal τ depends on a complicated balance between the truncation error (1) and the discretization error (2), which both grow as τ reduces, and the nonlinear term error (3), which grows as τ increases. As such, optimal τ depends on ε, ε_S, n, on the mesh size, and on the growth rates of the modes involved. It is possible to estimate optimal τ by finding the minimum of equation 4.30. The magnitudes of the eigenvalues are required, but a guess would be enough. Figure 4.12 shows that the error increases massively for $\tau > \tau_{opt}$ and much less so for $\tau < \tau_{opt}$, hence, to be on the safe side, it is advisable to use values of τ somewhat smaller than τ_{opt}, perhaps a factor of 5. It is important to note that the discussion focused on a situation where a nonlinear solver is used for an unstable flow, which is common. If a linear solver is used, upper bounds for τ apply only for stable modes and can be obtained from equation 4.22 (GÓMEZ; GÓMEZ; THEOFILIS, 2014), which is also embedded in equation 4.30.

In our study, with optimal parameters, second order accurate Fréchet derivative approximations consistently provided eigenvalue computations within an accuracy of 10^{-8}. First order ones consistently offered eigenvalue accuracy of 10^{-5}, even with slightly

suboptimal parameters. If this reduced accuracy is sufficient, first order can deliver it at about half the cost of the second order one, as it needs only one call to the flow solver per Arnoldi iteration. For open flows, small variations in the numerical boundary conditions used to represent an infinite domain can easily affect the fourth or even the third decimal place of the eigenvalue computation (OHMICHI; SUZUKI, 2016). Hence, with the optimal values of ε and τ, it is likely that, in many applications, first order accurate Fréchet derivative approximations would be the most cost-effective choice.

Parameter M affects only the accuracy of the Krylov span approximations, in the form of its product with τ. In fact, our tests demonstrate that the accuracy increases with τM, as explained by Goldhirsch, Orszag and Maulik (1987). M, however, has a more complicated impact on computation time because the Gram-Schmidt procedure scales with M^2 and the eigenvalue problem with around M^3, thus it is interesting to reduce M. Hence using optimal τ also leads to the most cost-effective approach. Under these circumstances, the computational effort is used almost entirely in the flow solver, and scales linearly with M. Hence, optimizations in the orthogonalization or in the eigenvalue solver algorithm have almost no impact. In contrast to ε and τ, there is not an optimal M for maximum accuracy. As M increases, the error in the eigenvalues eventually reduces to a noise floor associated with the other errors. As the Arnoldi algorithm evolves, the accuracy of the eigenvalues can be monitored until the target level or the noise floor is achieved. Contrary to ε and τ, the desired M does not need to be known a priori. If three-dimensional flows are investigated, the cost associated with the flow solver would be even larger and the conclusions would still hold. In our analysis the wall-time was used as a measure of cost. In many applications, CPU-time could be a better measure; however, given that at optimal conditions the cost is dominated by the flow solver, using CPU-time as a measure of cost would lead to the same guidelines. It is important to mention that in situations such as our test 2D case where the computational cost is dominated by the flow solver, the used of restarted Arnold methods does not improve efficiency, and for that reason it was not studied here. In 3D global instability analysis, restarted methods are even less likely to be advantageous.

Beyond these guidelines, we investigated the rate of convergence of the eigenvalues and observed that an eigenvalue initiates a rapid convergence only after the eigenfunction of some previous eigenvalues have converged. This is associated with the level of orthogonality between these eigenfunctions. Hence, eigenvalue convergence requires eigenfunction convergence and the current guidelines work for both.

Chapter 5

Large Open Cavities

5.1 Introduction

Several features of vehicles, ranging from small ones, such as gaps at doors and windows, to large ones, such as the landing gear wells of airplanes and car sunroofs can be represented by the simple geometry of an open cavity. The flow recirculates inside the cavity and a mixing layer forms at its opening. Under certain circumstances, the flow in unstable and oscillations develop, and high levels of sound are emitted. In transonic and supersonic flows, such oscillations can greatly increase the aerodynamic drag of surfaces with cavities (MCGREGOR; WHITE, 1970). Owen (1958), Dix and Bauer (2000) indicate that pressure fluctuations in the cavities can affect the aircraft structure and cause structural fatigue.

In the next section, we discuss the two-dimensional linear stability of the open cavity flow, especially its sensitivity to the incoming boundary layer thickness and Mach number. In the following sections, we analyze how three-dimensionality affects Rossiter modes, in the form of span-wise modulation of such modes as well as their interaction with centrifugal modes (MATHIAS; MEDEIROS, 2019a; MATHIAS; MEDEIROS, 2020).

A 6th order spectral-like spatial differentiation is chosen for these simulations, while the time integration is done by the classical 4th order Runge-Kutta scheme. The anti-aliasing filter coefficient is set to $\alpha = 0.49$ and it is turned off close to the open boundaries, while reduced order schemes, with smaller stencils, are used close to the walls. Meshes are constructed following the guidelines presented in chapter 3.

5.2 Two-dimensional results

Initially, our study was inspired by that of Yamouni, Sipp and Jacquin (2013), but, as opposed to them, who looked at very high Reynolds numbers, we were interested on conditions close to critical. This led us to lower Re_D numbers, guided by ROWLEY, COLONIUS and BASU (2002), Brès and Colonius (2008), Sun et al. (2017). Since we focus on the Rossiter modes only, a short cavity was used with a fixed $L/D = 2$ to avoid wake modes. Two main aspects are studied: the effect of the thickness of the incoming boundary layer; and the effect of the free flow Mach number.

Figure 5.1 shows results for a typical scenario investigated in this section, corresponding to the following parameters: $L/D = 2$, $Re_D = 1000$, $D/\theta = 100$ and $Ma = 0.5$. The left-hand side gives the pressure fluctuation contours of Rossiter mode 2 at an arbitrary phase, the thick black lines represent fluctuation amplitude level zero. The right-hand side shows the wall-normal velocity contours for modes 1 to 5, which will be referred here as R1 through R5. The mode number refers to the number of vortices in the mixing layer.

The Rossiter modes are described as a feedback mechanism involving four steps, namely: (1) Kelvin-Helmholtz (KH) vortices grow in the mixing layer at the cavity opening, (2) these vortices reach the trailing edge and emit sound, (3) the acoustic waves travel upstream and (4) excite new KH instabilities at the cavity leading edge. However, it is not entirely clear how much a global stability analysis can explain and predict this complicated (and non-linear) behavior. Originally, the Rossiter modes referred to the limit cycle oscillations observed in experiments. In linear stability analysis we obtain an approximation of such modes and when necessary to avoid confusion we use the term Rossiter mode linear approximation.

Further details of the analysis can be found in (MATHIAS; MEDEIROS, 2021b).

5.2.1 Influence of the boundary layer thickness

The literature overlooks the influence of the boundary layer thickness on the Rossiter instability. Studies focus on very specific D/θ values and, for that reason, here we investigate it in detail. A sweep of D/θ was performed (figure 5.2), where the Mach number was fixed at $Ma = 0.5$ and D/θ ranged between 10 and 200. In all cases, $L/D = 2$ and $Re_D = 1000$. Higher values of D/θ enhanced the instability. For very small D/θ, only R1 is unstable and the higher the Rossiter mode the more stable it is. Rossiter modes R4 and R5 were still immersed in the mode cloud and not identifiable, hence, not shown. In the parameter range investigated, the growth rates increase with D/θ, as observed at higher Reynolds numbers by Yamouni, Sipp and Jacquin (2013), and reach a saturation for large D/θ. Higher Rossiter modes show stronger variation of growth rates with respect to

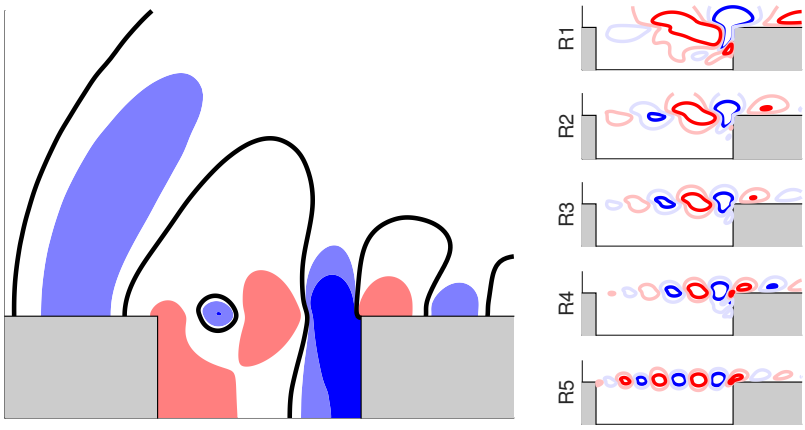

Figure 5.1 – Eigenfunctions of Rossiter mode linear approximations at $Re_D = 1000$, $D/\theta = 100$ and $Ma = 0.5$, at an arbitrary phase. (Left) Contours of pressure for mode 2. Black lines indicated level zero. (Right) Contours of wall-normal velocity for modes 1 to 5.

D/θ and saturate at higher values of D/θ. For these reasons, at higher D/θ, R2 overtakes mode R1 and becomes dominant. Afterwards, R3 also becomes more unstable than R1. The overall picture conveys the idea that, as D/θ increases, higher Rossiter modes become dominant if a saturation is not reached before. For the current parameter range only R1 and R2 dominate, but it seems that for higher Re or longer cavities, higher Rossiter modes could become dominant. At the same time, a slight increase in the mode frequency was observed. This is consistent with other studies which attribute the frequency increase to the higher convective velocity of the KH vortices in the mixing layer.

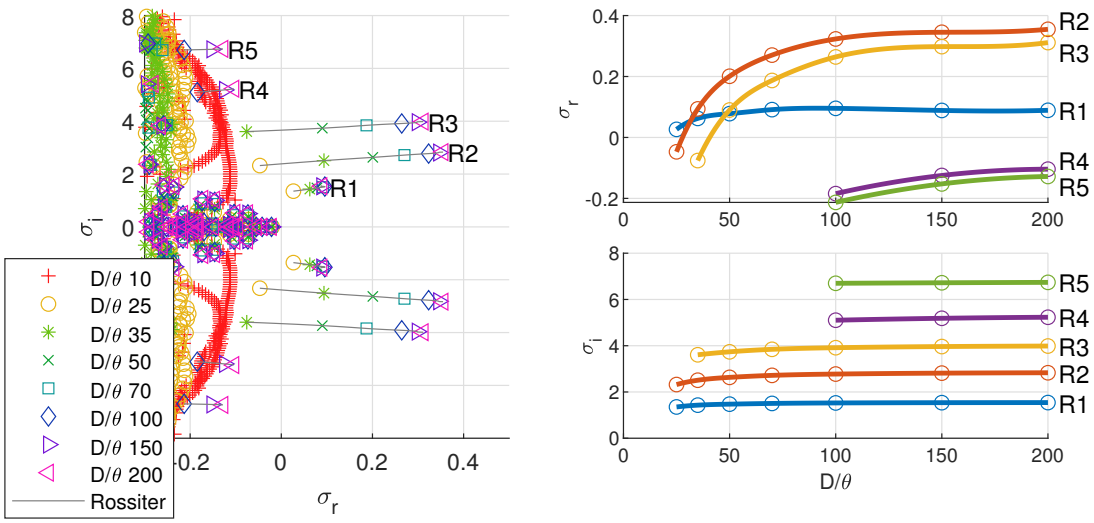

Figure 5.2 – Eigenvalues from the D/θ ratio sweep ($Re_D = 1000$, $Ma = 0.5$). (Left) Eigenspectrum. (Right) Real and imaginary parts of Rossiter mode eigenvalues.

In the current parameter space, the analysis indicates that, as D/θ increases, the flow moves from a regime where mode R1 dominates to one where modes R2 and R3 dominate. The increased instability for thinner boundary layers was attributed to the corresponding thinner mixing layers, which greatly enhanced the spatial amplification in the flow over the cavity, the unstable part of the cycle of the Rossiter modes. To substantiate the argument, the spatial growth of each mixing layer profile was obtained by solving the Orr-Sommerfeld equation. These amplification rates were integrated along the mixing layer to obtain the total spatial growth for each frequency ω, and are shown as the solid lines in figure 5.3 for different D/θ. In this analysis, the last 5% of the cavity length were disregarded, as the parallel-flow approximation was considered invalid there. The picture also includes bi-global stability growth rates of the Rossiter modes R1 to R5, which are referred to the vertical scale on the right-hand side of the frame. The figure shows that the global instability results are consistent with the mixing layer instability. Clearly, the dominant modes are selected by the mixing layer instability, confirming experimental observations by Sarohia (1977). The saturation at higher D/θ is also explained by this instability. This analysis considers incompressible flow, but at $Ma = 0.5$ the stability is not severely affected by compressibility, in particular the most unstable frequency.

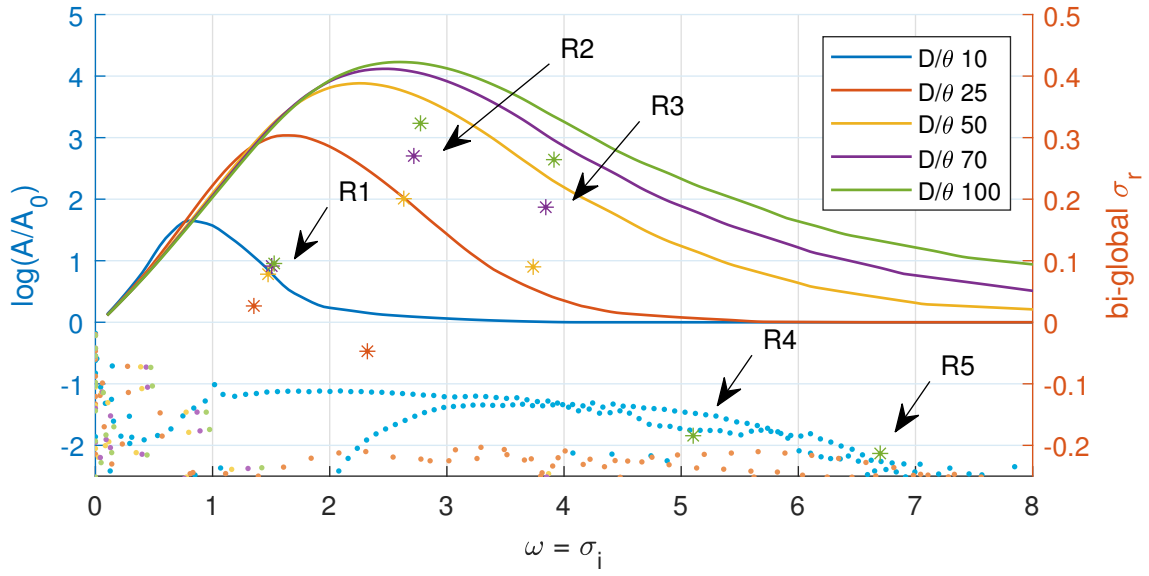

Figure 5.3 – Mixing layer integrated spatial amplification factor compared to the global instability results. The asterisks indicate the global modes eigenvalues of Rossiter modes and the dots are other eigenvalues, they refer to the scale on the right-hand side of the frame.

5.2.2 Influence of the Mach number

The previous section indicated that, in the current parameters, as D/θ increases, the flow moves from a regime where mode R1 dominates to one where modes R2 and R3 dominate. For the analysis of the compressibility effects, two representative Mach number sweeps were performed. As observed in figure 5.2, the thicker boundary layer at $D/\theta = 29.7$ represents a situation where only a pair of Rossiter modes is slightly unstable, while the thinner boundary layer at $D/\theta = 100$ is a more complex situation, with up to four unstable modes with higher temporal amplification levels. Figures 5.4 and 5.5 give, as a function of Mach number, the real and imaginary parts of the eigenvalues for both D/θ selected.

Within the parameter range covered, in general the sensitivity of the growth rates with respect to the Mach number was stronger for lower Mach numbers. For low D/θ (figure 5.4), at low Mach numbers, both R1 and R2 are stable and only these two modes become unstable as the Mach number increases. At low Mach numbers, R1 is the least stable. It becomes unstable at $Ma = 0.3$ and its growth rates saturates at about $Ma = 0.4$. R2 is more stable at low Mach numbers, but saturates only at higher Mach numbers, such that it becomes more unstable than R1 for $Ma > 0.5$.

For high D/θ (figure 5.5), four Rossiter mode linear approximations can be unstable in the Mach number range covered. Mode R2 is the most unstable for all Mach numbers and both R1 and R2 growth rates increase with the Mach number at the lower end but saturate at about $Ma = 0.3$. R3 and R4 are affected by compressibility in a more complex way. In all cases, the frequency reduces with the Mach number, a feature that is predicted by the Rossiter empirical equation and caused by the slower acoustic propagation upstream.

In summary, the most salient features of the Mach number effect are (1) the strong destabilizing effect of compressibility at low Mach number and (2), at high Mach numbers, either saturation or irregular behavior, depending on mode number and D/θ.

There is a strong destabilizing effect of Mach number at low number seen in figures 5.4 and 5.5, where compressibility has a small stabilizing effect on the mixing layer instability. Since Mach number did not considerably change the mixing layer profiles, the enhancement of the instability could not be associated directly with it. The receptivity of shear layer instability modes is not known to be very sensitive to the Mach number. On the other hand, the transfer of energy into acoustic waves grows very rapidly with the Mach number (GOLDSTEIN, 1976).

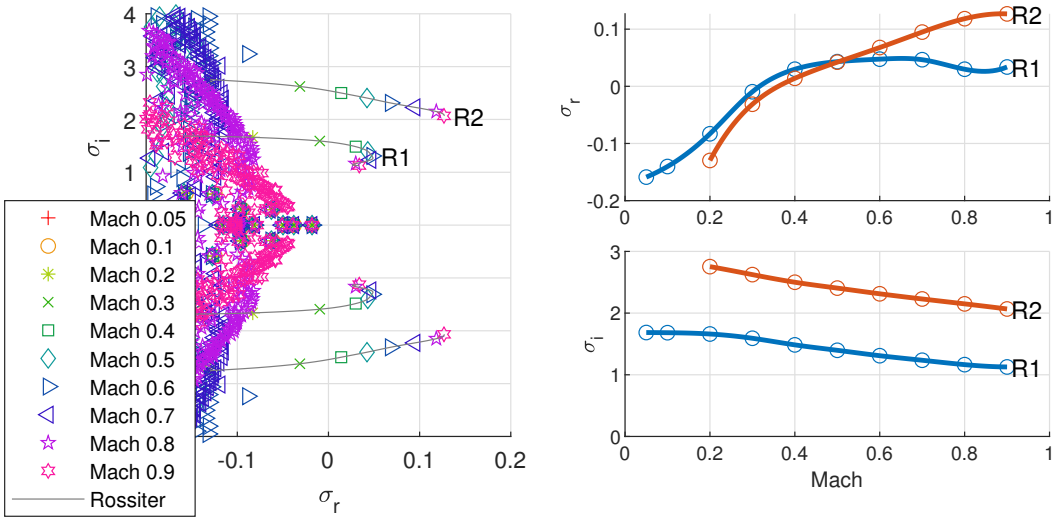

Figure 5.4 – Eigenvalues from the first Mach number sweep ($Re_D = 1149$, $D/\theta = 29.7$). (Left) Eigenspectrum. (Right) Real and imaginary parts of Rossiter mode eigenvalues.

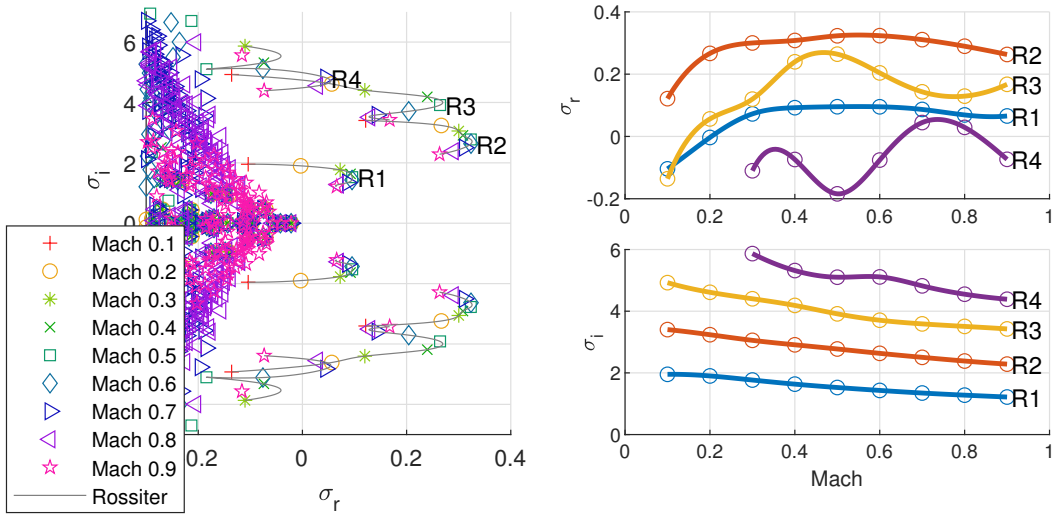

Figure 5.5 – Eigenvalues from the second Mach number sweep ($Re_D = 1000$, $D/\theta = 100$). (Left) Eigenspectrum. (Right) Real and imaginary parts of Rossiter mode eigenvalues.

Howe (2004) investigates the emission of sound by a cavity at low Mach numbers. In Howe's model, the acoustic energy transfer (ET_{Ac}) was computed as

$$ET_{Ac} = \frac{E_{Ac}}{E_{SL}} \ , \tag{5.1}$$

where

$$E_{Ac} = \int_{P_{Ac}} |p|^2 \, dx \ , \tag{5.2}$$

is the acoustic power in the far field and

$$E_{SL} = \int_{P_{SL}} |\nabla \cdot (\boldsymbol{\omega} \wedge \boldsymbol{v})| \, dx, \tag{5.3}$$

is the source term. In the equations, p, v and $\boldsymbol{\omega}$ are, respectively, pressure, velocity and vorticity, which can be obtained from the eigenfunctions of the Rossiter mode linear approximations. This was done as illustrated in figure 5.6. The source term was estimated by integrating across the shear layers, along the vertical black line shown in the figure. For the acoustic power, the integration was along a semi-circumference centered at the cavity trailing edge with radius equals to $2D$, starting at the cavity leading edge, but ending before the wake of Rossiter modes (the green line). It is not entirely clear whether this region corresponds to the near or the far field of the acoustic source, particularly in view that the extension of these fields is also affected by the Mach number. Regardless of that, we will refer to this region as acoustic field. Clearly, this position provides an estimate of the pressure fluctuations that trigger the Kelvin-Helmholtz vortices. In the picture, isocontours of the values of pressure and velocity eigenfunctions of the Rossiter mode 2 at $Ma = 0.6$ were overlaid to illustrate the flow at an arbitrary phase.

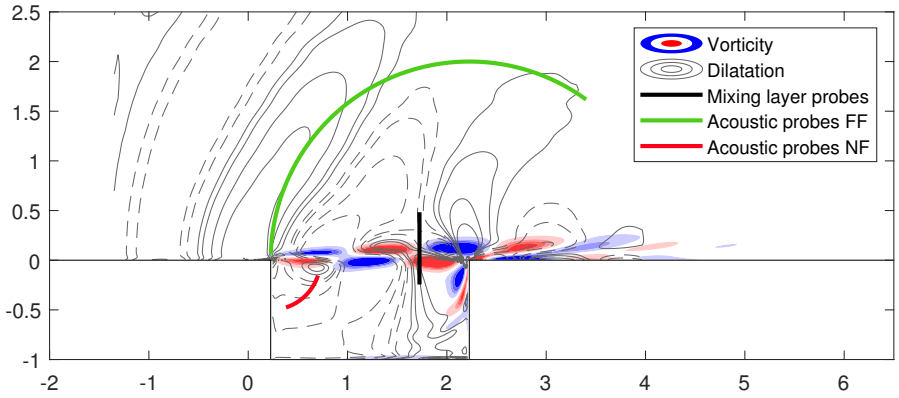

Figure 5.6 – Location of probes for the analysis of sound emission. Gray contours indicate dilatation fluctuations of the second Rossiter mode at $Ma = 0.6$, full line for positive contours and dashed line for negative ones. Colored contours indicate vorticity fluctuations. The black line indicates region of evaluation of sound source magnitude. Red and green lines indicate regions of evaluation of the magnitude of the pressure fluctuations.

In the analysis, the pressure and the velocities are normalized by their far-field values. Figure 5.7 shows the ET_{AC} as a function of Mach number, for modes 1 and 2 at

$D/\theta = 29.7$. The picture includes power functions of exponent 2 and 3 for reference. The acoustic energy transfer increases with the Mach number raised to a power between 2 and 3, depending on the Mach number and the mode.

The evaluation of the source term and acoustic power was also carried out with other integration regions around the green and black lines of figure 5.6. The near-field probes, shown in red, were used to test the sensitivity of results to the location of the probes and led to comparable, albeit noisier results.

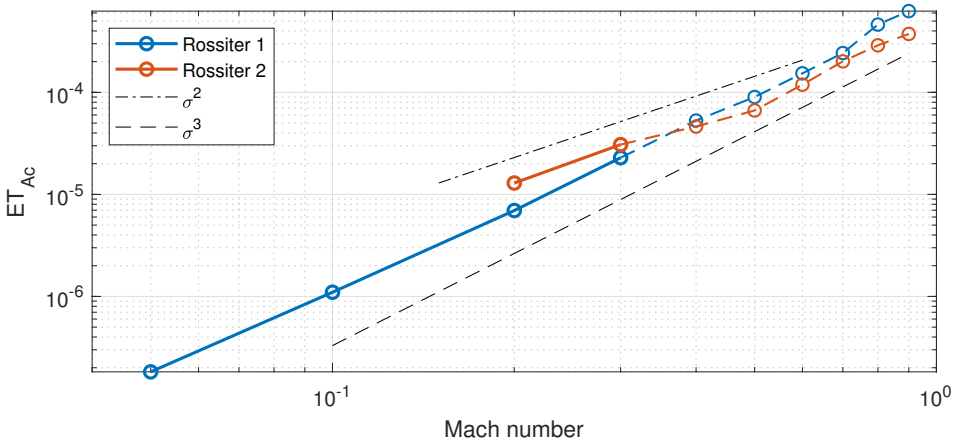

Figure 5.7 – Acoustic energy transfer (ET_{AC}) as a function of Mach number for the linear approximation of Rossiter modes 1 (blue) and 2 (red). The dashed and dashed-dotted lines represent Ma^3 and Ma^2 respectively.

The results are consistent with those by Howe (2004), which suggests that, at most frequencies, a dipole dominates the acoustic emission of the open cavity, which is proportional to $\rho_0 U^3 Ma^3$. However, it is unclear whether our so-called acoustic region corresponds to the near or the far field of the acoustic source. Moreover, Howe's theory is restricted to very low Mach numbers. Yamouni, Sipp and Jacquin (2013) also presents other arguments for a dipole source in connection with the acoustic cavity modes. In any case, more important for our analysis is the observation that indeed a consistent quantification of energy transfer could be extracted from the eigenfunctions and that the strong dependence on the Mach number offers an explanation for the large sensitivity of the amplification rates of the linear Rossiter mode at low Mach numbers.

Figure 5.5 also shows that, for high D/θ, modes 3 and 4 growth rates depend on Mach number in a very complex way, while modes 1 and 2 display a smooth dependence on Mach for both values of D/θ considered. Yamouni, Sipp and Jacquin (2013) observed a similar complex dependence and linked it to a resonance between Rossiter modes and standing acoustic waves in the cavity. These standing waves are described by Plumblee, Gibson and Lassiter (1962).

Figure 5.8 presents the frequency of Rossiter and standing waves modes as a

function of Mach number. The blue solid lines represent the Rossiter modes as predicted by

$$\omega = \frac{2\pi N_R}{\frac{1}{\kappa} + Ma\left(1 + \frac{0.514}{L/D}\right)}, \tag{5.4}$$

an equation proposed by Block (1976), which considers the cavity aspect ratio (L/D). In the equation, N_R is the Rossiter mode number and $\kappa = 1/1.75$ is an empirical constant. In the figure, the dashed orange lines represent the standing wave modes given by (PLUMBLEE; GIBSON; LASSITER, 1962)

$$\omega = \frac{\pi}{2Ma}\left[\left(\frac{M_p}{L}\right)^2 + \left(\frac{N_p}{D}\right)^2\right], \tag{5.5}$$

where M_P is the number of standing waves wavelengths in the stream-wise direction and N_P, in the wall-normal direction. The modes are identified by (M_P, N_P). In the case of a cavity with aspect ratio L/D=2, modes (2,0) and (0,1) coincide in frequency.

The figure also displays results from global instability analysis given by the circles. The circle radius is proportional to the distance from neutral stability conditions, the solid circles represent instability while hollow circles represent stability. Large, filled symbols indicate strong instability, large hollow symbols, the opposite.

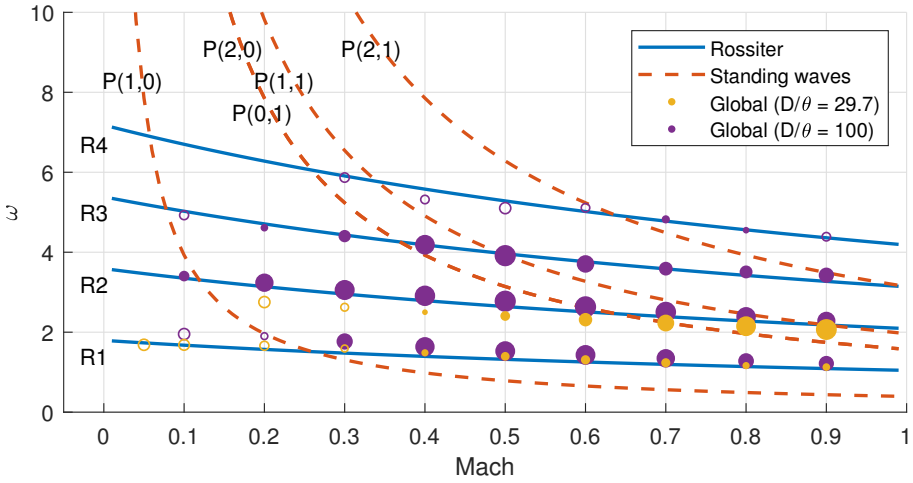

Figure 5.8 – Frequency predictions of Rossiter modes (blue) and standing wave modes (orange) compared to the global mode results (circles). The circle radius is proportional to the distance from neutral stability, the solid circles represent instability while hollow circles represent stability.

A correlation can be found between both types of modes and the global instability results. Rossiter mode 3 shows increased instability when the R3 curve approaches the $P(2,0)$ and $P(1,1)$ curves and, at a higher Mach numbers, the $P(2,1)$ curve. Mode R4 is

also affected by these interactions, not only on the growth rates but also in the frequency, the latter may be associated with the fact that this mode is only marginally unstable or stable. Albeit less pronounced, variations in frequency consistent with this argument are also observed for R3.

At lower frequencies, the $P(m,n)$ curves tend to become parallel to the R1 and R2 curves. This smooths out the dependence on Mach number but may be associated with a maximum instability for R1 at $Ma = 0.6$ and low D/θ (see figure 5.4), which has also been reported by Sun et al. (2017) at similar conditions. It may also explain why, contrary to all other modes that were observed to saturate at $Ma = 0.6$, mode 2 at low D/θ, seems to saturate only at $Ma = 0.9$.

5.3 Three-dimensional global stability

Apart from the two-dimensional modes that dominate in the form of Rossiter modes, in this parametric region, there are also three-dimensional unstable modes; namely centrifugal modes and span-wise modulated Rossiter modes. In this section, we investigate three-dimensional instability for an array of span-wise wave numbers (β), so that the periodicity in this direction has length $L_Z = 2\pi/\beta$. The LST routine was used in span-wise spectral mode, in which a single span-wise wave number is allowed each time. The 2D case is equivalent to $\beta = 0$, which considers the domain to be infinite and uniform in this direction.

Figure 5.9(Left) shows the eigenvalues as a function of β. Note that centrifugal modes have much lower amplification rates than Rossiter modes. Their frequency is lower by about one order of magnitude.

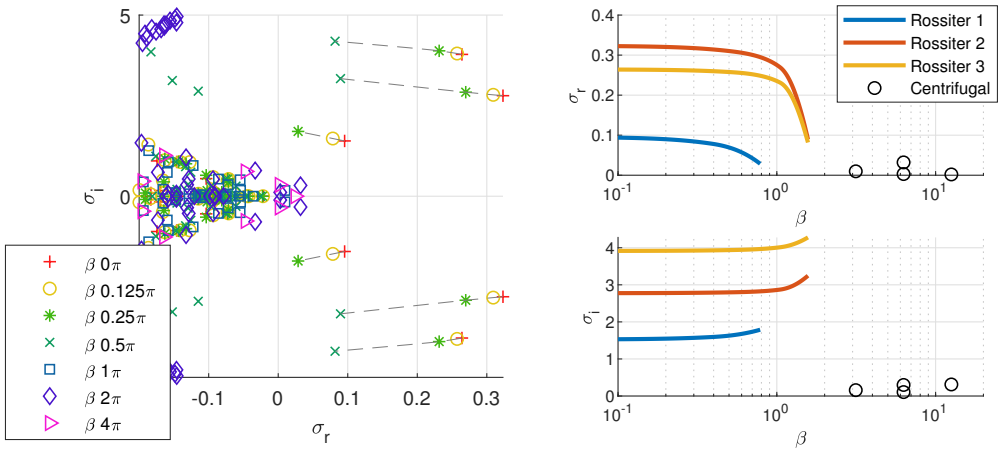

Figure 5.9 – Eigenvalues from the span-wise wave number sweep ($Re_D = 1000$, $D/\theta = 100$, $L/D = 2$, $Ma = 0.5$). (Left) Spectra in the complex plane. (Right) Real and imaginary parts of the eigenvalues of the Rossiter and centrifugal modes.

At lower β, Rossiter modes dominate. Slightly above $\beta = 1$, their growth rate reduces sharply. At the higher end of the spectrum, centrifugal modes appear. Under these conditions, there is no value of β for which both Rossiter and centrifugal modes are unstable. Figure 5.10 shows the most unstable modes for $\beta = \pi/4$ and $\beta = 2\pi$ at an arbitrary phase, they are Rossiter and centrifugal modes, respectively. In the next section, we further explore the instability analysis; however, the results shown here are representative of the parameter space investigated, in particular the fact that 2D Rossiter modes have much higher growth rates and frequencies in comparison with centrifugal modes.

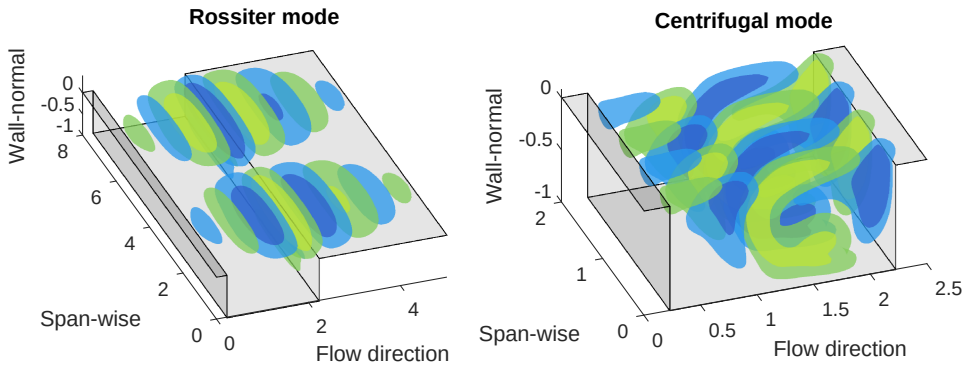

Figure 5.10 – Most unstable eigenmodes from the 3D LST analysis. (Left) $\beta = \pi/4$, isosurfaces of density. (Right) $\beta = 2\pi$, isosurfaces of span-wise velocity.

5.4 Non-linear effects

Next, we wanted to verify to which extent the global linear stability results could predict the nonlinear behavior of the flow. For this, DNS were performed. The study initiated with the $Re_D = 1000$, $D/\theta = 100$, $L/D = 2$, $Ma = 0.5$ case, the same presented in the previous section. Figure 5.11 presents results of 2D and 3D simulations. At the left-hand side of the figure, we show the time series of pressure at the cavity trailing edge at an arbitrary span-wise position for both 2D and 3D cases; at the right-hand side, we compare their spectra.

For the initial condition of the 2D case, no noise was added apart from the numerical background noise which stood at 10^{-13}. In the 3D simulation, a small span-wise disturbance was also added to trigger the three-dimensional effects. The flow was periodic in the span-wise direction and the span-wise domain was long enough that the flow became statistically independent on this direction, as is discussed later in this section.

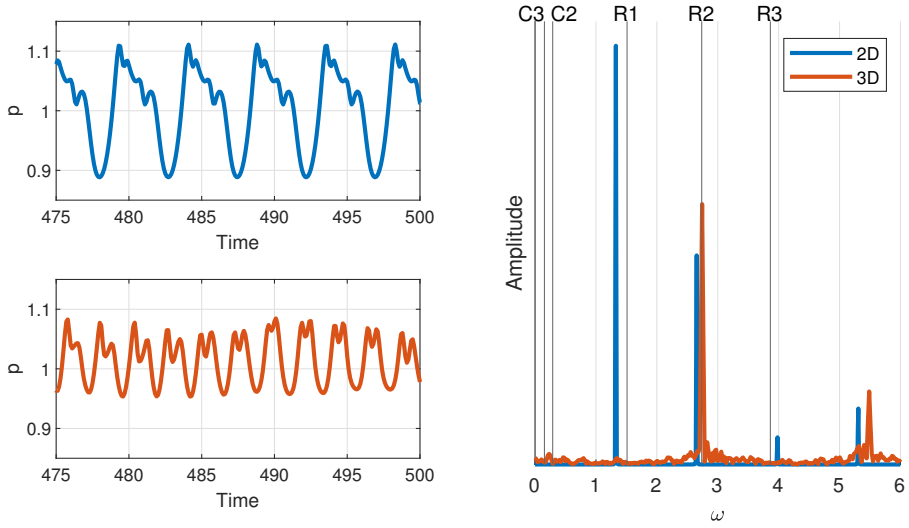

Figure 5.11 – Comparison between 2D and 3D simulations of the $Re_D = 1000$, $D/\theta = 100$, $L/D = 2$, $Ma = 0.5$ case. (Left) Time series of pressure at the trailing edge. (Right) Spectrum. The vertical lines mark angular velocities predicted by the linear stability analysis for each Rossiter mode (R1 through R3) and centrifugal mode (C2 and C3).

Previous section showed that the Rossiter mode was essentially 2D and much more unstable than the centrifugal modes. This suggests that 2D simulation should capture most features of the nonlinear regime of the cavity flow. However, while LST predicts the R2 mode as dominant, in the nonlinear simulation the R1 is the dominant. Perhaps even more surprising is that for the 3D simulation, the dominant mode is the R2 with a frequency very close to the LST predictions. In the 3D simulation, there is also a small peak in the spectrum between the frequencies predicted for centrifugal modes C2 and C3, at $\omega_{C2} = 0.29$ and $\omega_{C3} = 0.15$, respectively. In this section, we investigate why the 3D simulation results were closer to the 2D linear stability prediction than the 2D simulation.

Linear stability is expected to provide good predictions of the nonlinear behavior if the flow is close enough to the neutral conditions. However, it is difficult to predict a priori just how close it needs to be. We then tested conditions close to neutral and progressively more unstable to try and identify the mechanism that could explain the observation in figure 5.11. Three cases were chosen based on linear stability analysis. The first case (`R`) has no unstable centrifugal modes, only Rossiter modes are unstable. The second case (`C`) is the opposite, no unstable Rossiter modes, only centrifugal ones are unstable. The third case (`R+C 1`) is unstable for both types of modes, albeit at a much lower instability level when compared to the case from figure 5.11, which hereinafter will be referred to as case `R+C 2`. `R+C 3` is the most unstable of all cases. Table 5.1 summarizes the parameters for these cases. Note that Mach and Reynolds numbers were used to control the instability of each type of mode, considering that Rossiter is much more sensitive to Mach number than

the centrifugal mode, as was seen in the diagram by Brès and Colonius (2008), shown in figure 1.2. The table also shows which of the Rossiter and centrifugal modes were unstable in each scenario, sorted from the most to the least unstable.

Table 5.1 – Cases defined to investigate the interaction of Rossiter and centrifugal modes

Case	Re_D	Ma	D/θ	L/D	Rossiter	Centrifugal
`R`	1200	0.5	25	2	Unstable (R1)	Stable
`C`	1500	0.3	25	2	Stable	Unstable (C2)
`R+C 1`	1500	0.5	25	2	Unstable (R1)	Unstable (C2)
`R+C 2`	1000	0.5	100	2	Unstable (R2, R3, R1)	Unstable (C1, C2, C3)
`R+C 3`	1500	0.5	100	2	Unstable (R3, R2, R1)	Unstable (C1, C2, C3)

Figure 5.12 shows the growth rate of the most unstable mode as a function of β for each of the first three cases. The colored regions in the plot represent distinct types of modes. The centrifugal modes are subdivided into 3 groups of decreasing value of β (BRÈS; COLONIUS, 2008). Centrifugal mode I is stationary, i.e. $\omega = 0$, while mode II has the highest frequency of the three. In the first three cases considered, only mode II becomes unstable.

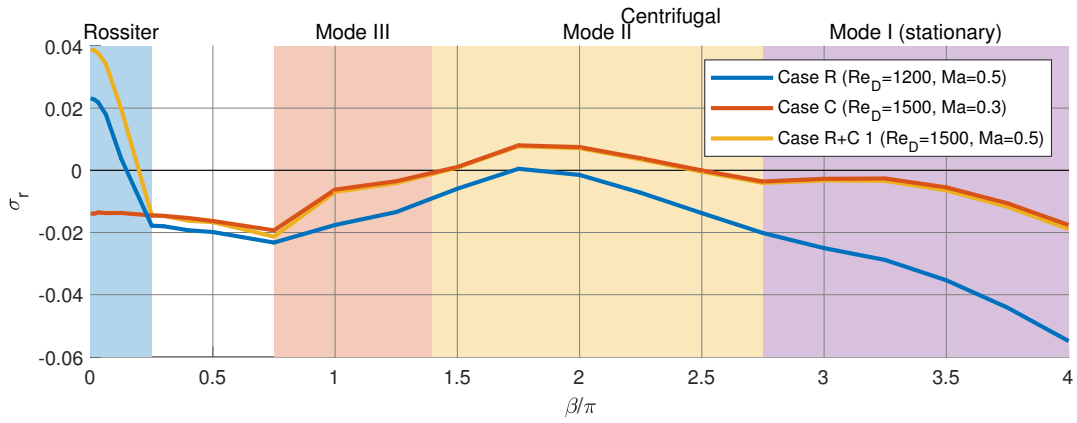

Figure 5.12 – Most unstable mode at each β for the first three cases defined in table 5.1. Each colored region represents a different type of mode.

The time series of pressure fluctuation from these cases are shown in figure 5.13, each color represents a probe in a different span-wise position. In agreement with the LST, case `R` becomes two-dimensional after fully developed, despite displaying some three-dimensionality between $t = 300$ and $t = 500$ shown by the different signals from each probe. Also in agreement with the LST, case `C` shows only three-dimensional oscillations. The span-wise distance between the probes is half a wavelength of the most unstable centrifugal mode, and the signals are perfectly consistent with this situation. The span-wise domain of case `C` corresponded two periods of the most unstable centrifugal mode; while, for case `R`, the domain was large enough for the span-wise modulated Rossiter modes of wave numbers as low as $\beta = \pi/16$. Case `R+C 1` presents a combination of both Rossiter and

centrifugal modes. Figure 5.14 shows that the nonlinear flow oscillates at the frequencies very close to those predicted by the LST. Hence, unlike the more unstable case `R+C 2`, these marginally unstable cases agreed with the global stability analysis.

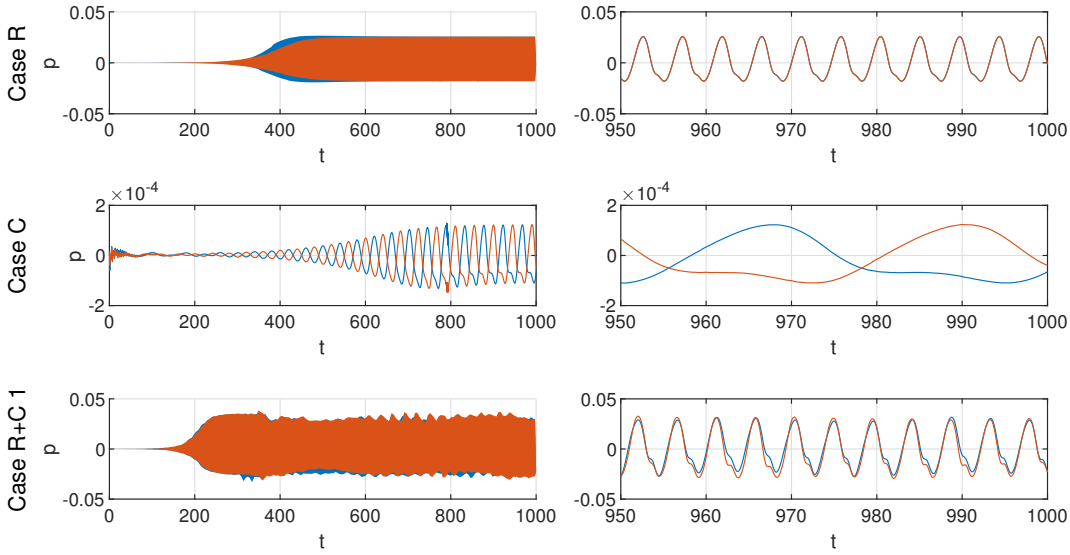

Figure 5.13 – Time series of pressure fluctuation for the cases defined in table 5.1. Blue and orange curves represent different span-wise positions.

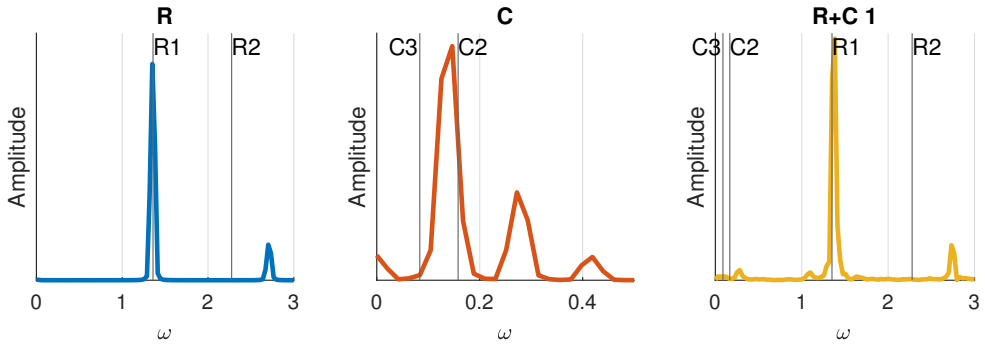

Figure 5.14 – Spectra of cases `R`, `C` and `R+C 1`. The linear predictions of angular velocities of each mode are also marked.

The last case is `R+C 3`, which is more unstable than `R+C 2` and much more unstable than `R+C 1`. It is defined by $L/D = 2$, $Re_D = 1500$, $D/\theta = 100$ and $Ma = 0.5$. Compared to case `R+C 2`, the Reynolds number based on cavity depth was increased from 1000 to 1500. The linear stability results of cases `R+C 1`, `R+C 2` and `R+C 3` are shown in figure 5.15. The time series of the simulations of case `R+C 3` are shown in figure 5.16.

Cases `R+C 2` and `R+C 3` reached comparable simulation results, in which the signals are much more irregular that of case `R+C 1`. The linear stability analysis of case `R+C 3` predicts Rossiter mode 3 to be the most unstable, at $\sigma_{R3} = 0.42 \pm 3.9i$, slightly ahead of

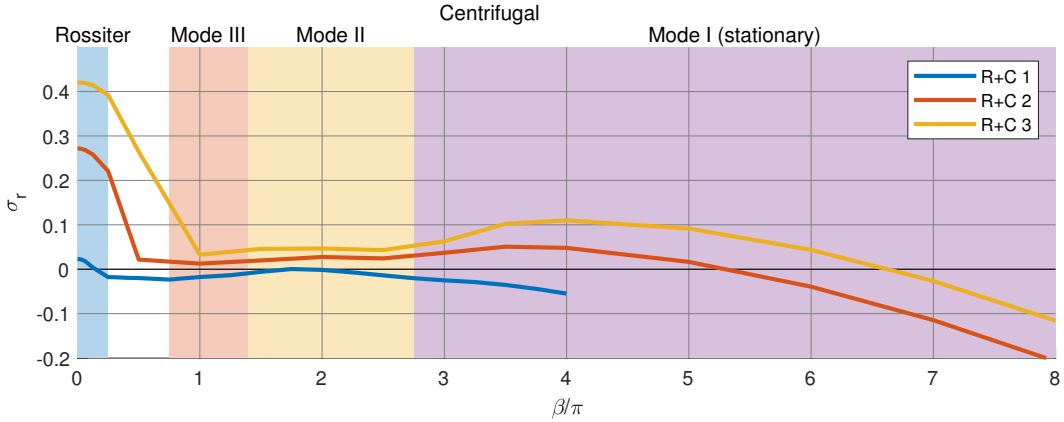

Figure 5.15 – Most unstable linear mode for cases `R+C 1`, `R+C 2` and `R+C 3` for various values of β.

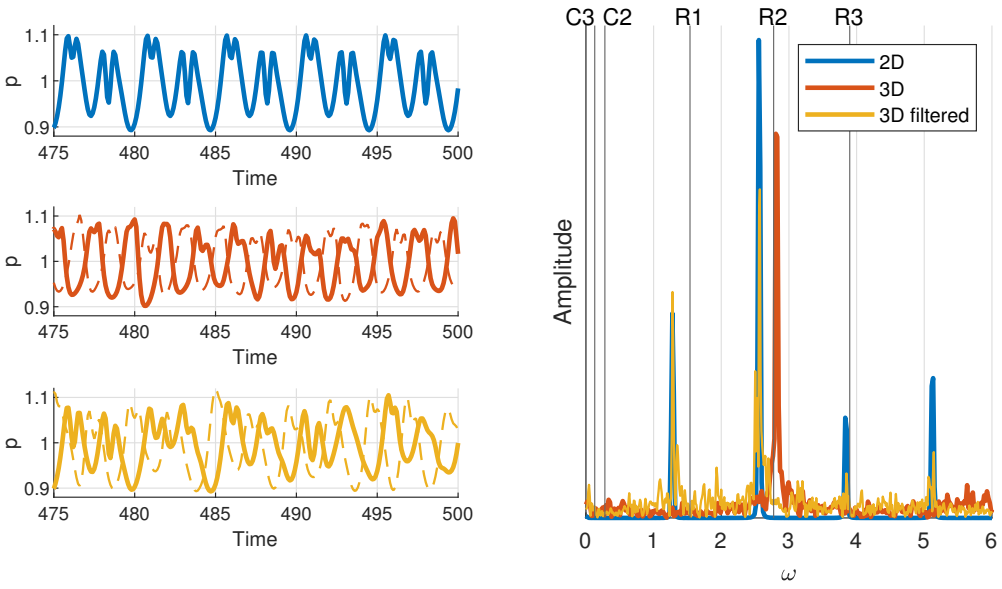

Figure 5.16 – Comparison between 2D and 3D simulations of case `R+C 3` ($Re_D = 1500$, $D/\theta = 100$, $L/D = 2$, $Ma = 0.5$). (Left) Time series of pressure at the trailing edge. The dashed lines were measured at another span-wise position. (Right) Spectrum. The vertical lines mark angular velocities predicted by the linear stability analysis for each Rossiter mode (R1 through R3).

mode 2, which is at $\sigma_{R2} = 0.41 \pm 2.8i$. Modes 1 and 4 are also unstable, but much less so, at $\sigma_{R1} = 0.12 \pm 1.5i$ and $\sigma_{R4} = 0.10 \pm 5.1i$, respectively. By looking at the spectrum of case `R+C 3` (figure 5.16), we observe that the flow is dominated by Rossiter mode 2, which is close to the prediction by the linear stability analysis. Unlike case `R+C 2`, the centrifugal modes were not visible in the spectrum. However, the 2D simulation of case `R+C 3` shows a different picture. Even though Rossiter mode 2 still dominates the flow, it is at a frequency different than that predicted by the linear stability analysis. Moreover, the spectrum shows a strong subharmonic, indicating that the flow is close to switching

to Rossiter mode 1. Figure 5.17 compares snapshots of wall-normal velocity for the 2D simulation of cases `R+C 2` and `R+C 3` and the 3D simulation of case `R+C 3`. Note that there is a single vortex in the cavity opening for the 2D simulation of case `R+C 2`, indicating that Rossiter mode 1 dominates the flow. Both 2D and 3D simulations of case `R+C 3` show two vortices in the cavity opening, indicating Rossiter mode 2 to be dominant.

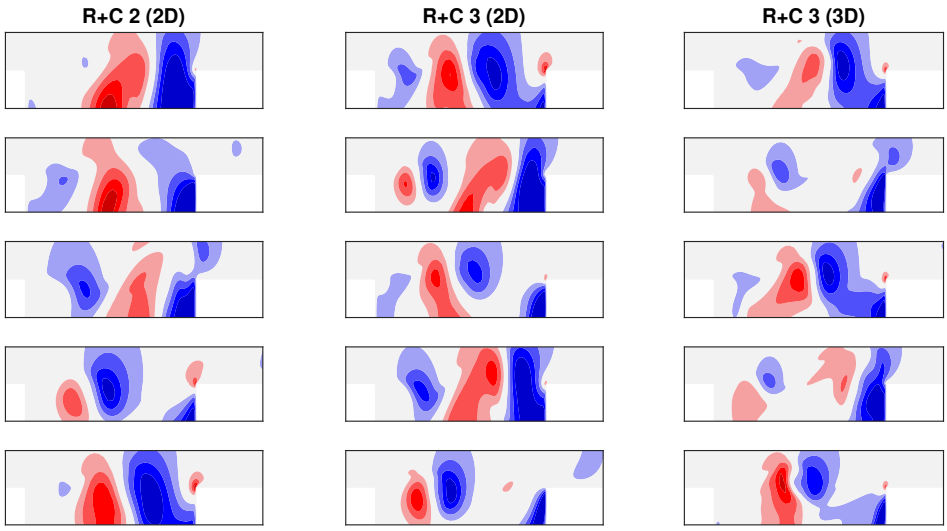

Figure 5.17 – Snapshots of wall-normal velocity for the 2D simulation of cases `R+C 2` and `R+C 3` and the 3D simulation of case `R+C 3`. The snapshots of the 3D simulation were taken at an arbitrary span-wise position.

For the `R+C 3` case, once more 3D simulations showed better agreement with LST than 2D simulations. To try and understand this observation, the following strategy was employed: There are two types of unstable three-dimensional modes in these flows: centrifugal modes and span-wise modulated Rossiter modes. We have artificially removed the centrifugal modes from the flow by using a span-wise mesh that is too course to resolve their high wave numbers. In this way, we can remove the effect of the centrifugal mode from the 3D simulation. Figure 5.16 also shows the resulting time series of this simulation as well as its spectrum. The dashed line in the left-hand side of the figure shows the pressure data for another span-wise position, which are different from the first probe, meaning that the flow still has three-dimensional effects. The spectrum of the 3D filtered case has peaks at the same frequencies as the 2D case.

From section 5.2.1, we know that one of the deciding factors for the selection of the Rossiter modes is the thickness of the mixing layer above the cavity. Thinner mixing layers are more unstable, relative to the cavity size, and favor Rossiter modes of higher order. Figure 5.18 (Middle) shows the thickness of the mixing layer for case `R+C 3` in four situations: the base flow, the mean flow of the 2D simulation, the mean flow of the 3D simulation and the mean flow of the filtered 3D simulation. The bottom part of this figure

shows the total spatial amplification for each case for a range of angular velocities ω, the angular velocities of Rossiter modes 1 through 3 are also marked in the figure.

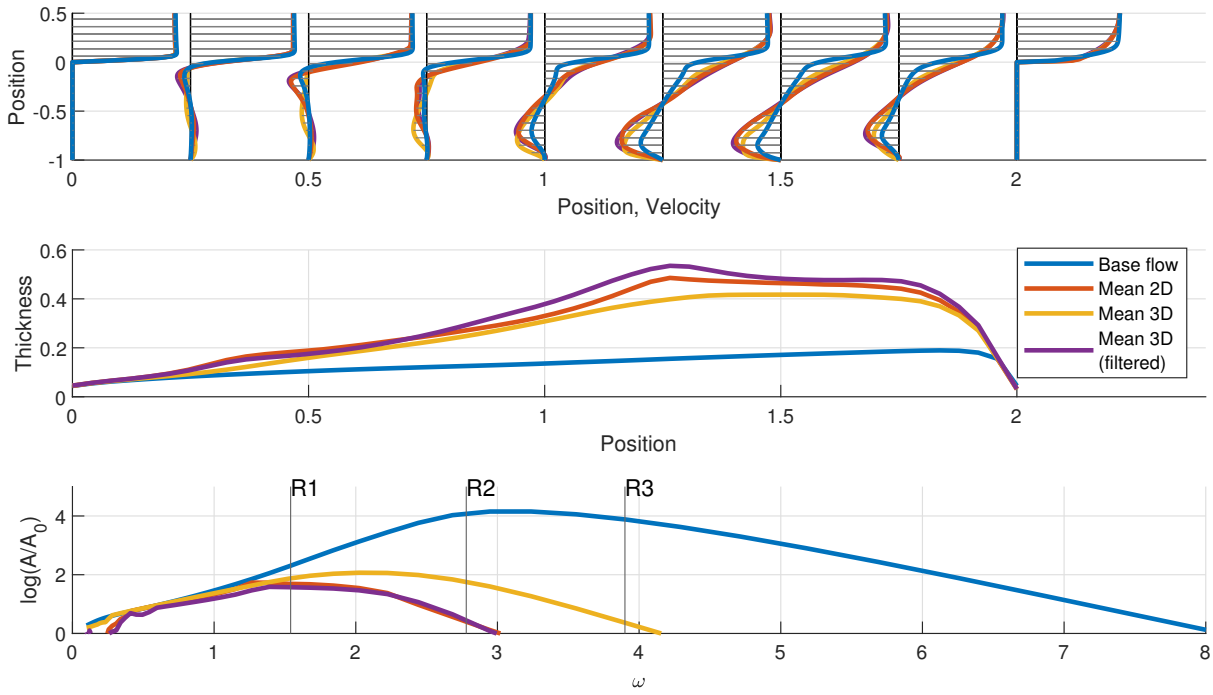

Figure 5.18 – (Top) Velocity profiles of the mean flow. (Middle) Mixing layer thickness for different situations of case `R+C 3` (Bottom) Total spatial amplification of each mixing layer as a function of ω.

For all mean flows, the mixing layer is considerably thicker than of the base flow. However, the 3D case has not thickened as much as the 2D case. Furthermore, the filtered 3D case is much closer to the 2D case than to the well-resolved 3D case. A similar conclusion can be reached by looking at the spatial amplification along the mixing layer for each scenario. The base flow clearly favors the frequencies of Rossiter modes 2 and 3, matching the global stability prediction. The 3D case has similar amplifications at the frequencies of Rossiter modes 1 and 2. The 2D and the 3D filtered cases clearly favor the first Rossiter mode, which explains the strong subharmonic of Rossiter mode 2 in the spectra, meaning that the flow is close to switching to Rossiter mode 1.

Further evidence of the effect of the centrifugal mode can be seen in figure 5.19, which shows the spectra of case `R+C 3` for the 2D, 3D and filtered 3D simulations as a function of time, which was obtained with the use of Hanning windows. The sampling frequency was set to 10 and each window was 1024 samples long, resulting in windows that are 102.4 time units long. The time series for this figure is the pressure at a probe at the cavity trailing edge at an arbitrary span-wise position. Once more, the strong subharmonic of the second Rossiter mode can be seen in the 2D and filtered 3D cases, albeit the latter does not have a spectrum as regular as the former. Figure 5.20 shows the same analysis, but this time the signal is from a probe of wall-normal velocity inside the cavity, at three

quarters of the length and half of the depth, which is much more suited for capturing centrifugal modes. This probe shows that the centrifugal modes are always present in the low end of the spectrum of the 3D case. In the filtered case, a signal appears sporadically, which may be an ill resolved version of the centrifugal mode. These centrifugal modes were not seen in the previous image because their eigenfunctions only have a very small projection of pressure at the trailing edge; most of these modes' fluctuation happen in the velocity field inside the cavity.

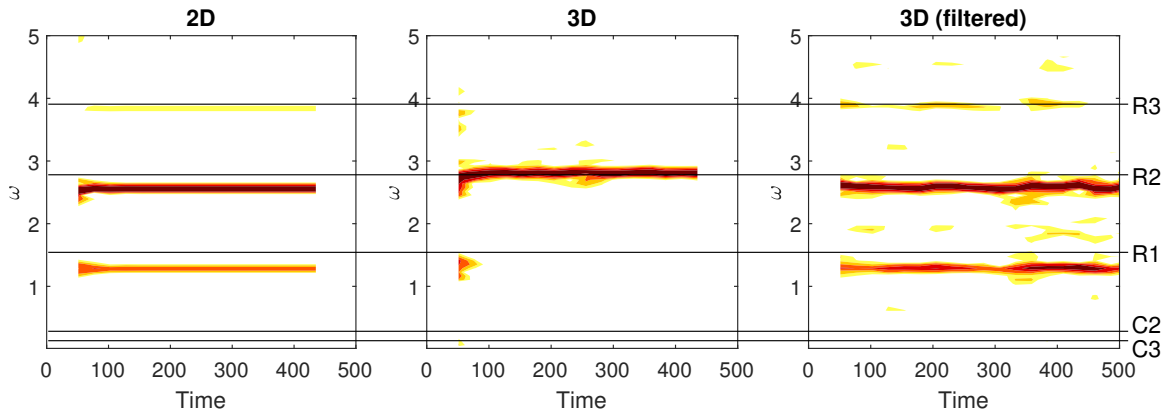

Figure 5.19 – Spectrum of pressure at the trailing edge as a function of time for case `R+C 3` ($Re_D = 1500$, $D/\theta = 100$, $L/D = 2$, $Ma = 0.5$) for (Left) the 2D simulation, (Center) the 3D simulation and (Right) the filtered 3D simulation. LST-predicted frequencies for Rossiter modes are also shown.

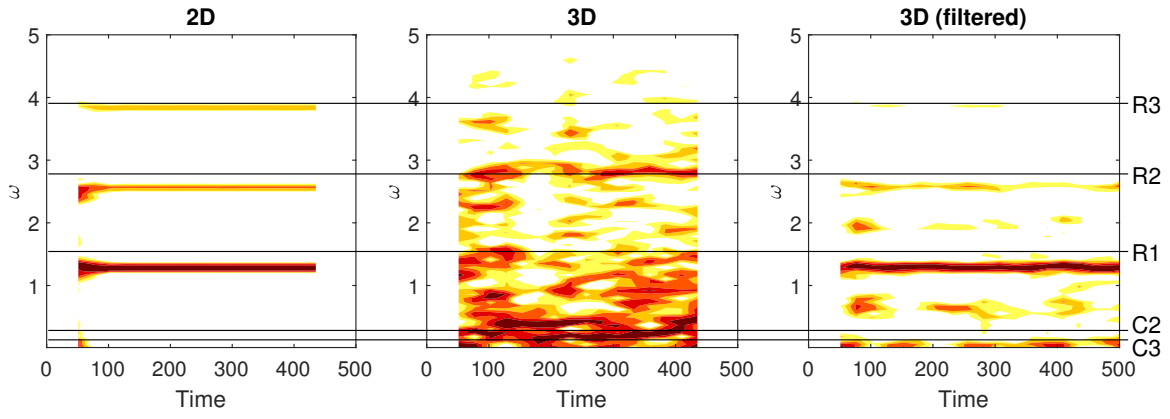

Figure 5.20 – Spectrum of wall-normal velocity inside the cavity as a function of time for case `R+C 3` ($Re_D = 1500$, $D/\theta = 100$, $L/D = 2$, $Ma = 0.5$) for (Left) the 2D simulation, (Center) the 3D simulation and (Right) the filtered 3D simulation. LST-predicted frequencies for Rossiter modes are also shown.

Figure 5.21 shows the time-series and spectra of case `R+C 3` for the 2D, 3D and filtered 3D simulations after the limit cycle was reached. This time, the wall-normal velocity inside the cavity was used for a better visualization of the centrifugal modes.

There is a small peak in the spectrum at $\omega = 0.21$, which is between the frequencies predicted for centrifugal modes II and III, at $\omega_{C2} = 0.28$ and $\omega_{C3} = 0.13$, respectively. Both these centrifugal modes were predicted as unstable by the linear stability analysis.

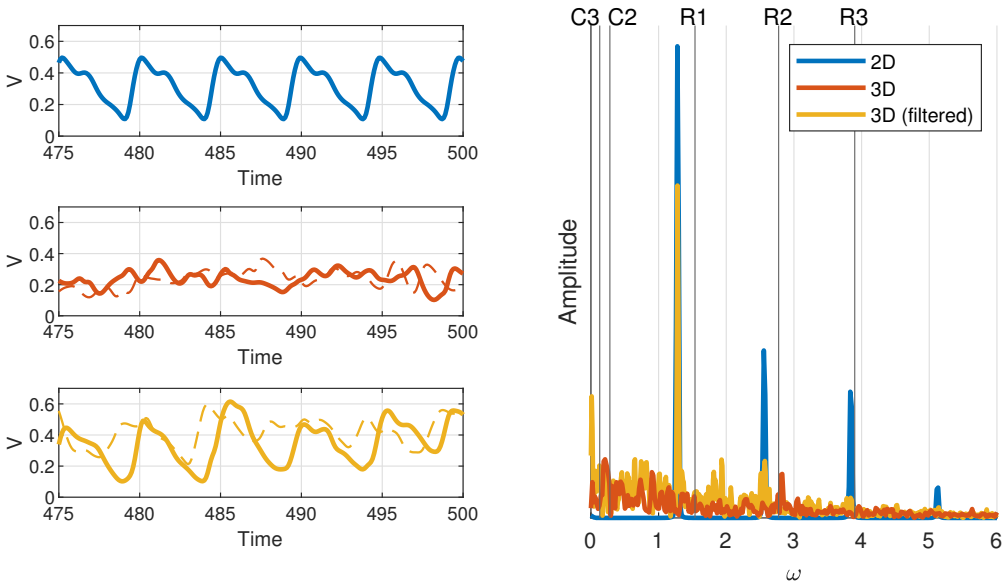

Figure 5.21 – Comparison between 2D and 3D simulations of case `R+C 3` ($Re_D = 1500$, $D/\theta = 100$, $L/D = 2$, $Ma = 0.5$). (Left) Time series of wall-normal velocity in the cavity. The dashed lines were measured at another span-wise position. (Right) Spectrum. The vertical lines mark angular velocities predicted by the linear stability analysis for each Rossiter mode (R1 through R3).

By taking the two-dimensional spectrum of the limit cycle of case `R+C 3`, in both time and span-wise direction, we can confirm the presence of centrifugal modes. Figure 5.22 shows the spectra of pressure at the cavity trailing edge and of wall-normal velocity inside the cavity. The pressure spectrum shows very little three-dimensional activity and has a very large peak, which corresponds to the second Rossiter mode. The velocity spectrum, on the other hand, is better suited to capture the centrifugal modes and shows no clear peak in the Rossiter mode frequency; however, there is energy at low frequency, especially between $\beta = 0.5\pi$ and $\beta = \pi$, including substantial energy at frequency $\omega = 0.21$, which corresponds to the LST prediction of centrifugal mode III.

To test the robustness of these results, we have taken a fully developed 2D simulation, converted it to 3D and added a small disturbance (white noise of RMS equals to 10^{-10}) to trigger the 3D instabilities. After some time, the dominant mode had switched from Rossiter mode 1 to mode 2. Later in this simulation (at $t = 250$), we have added a filter to damp out all three-dimensional oscillations, forcing the flow to become 2D again, which has caused Rossiter mode 1 to emerge once more. Figure 5.23 shows the spectrum of pressure (left) and velocity (right) for this case.

Finally, we wish to understand what the minimum span-wise domain length for an

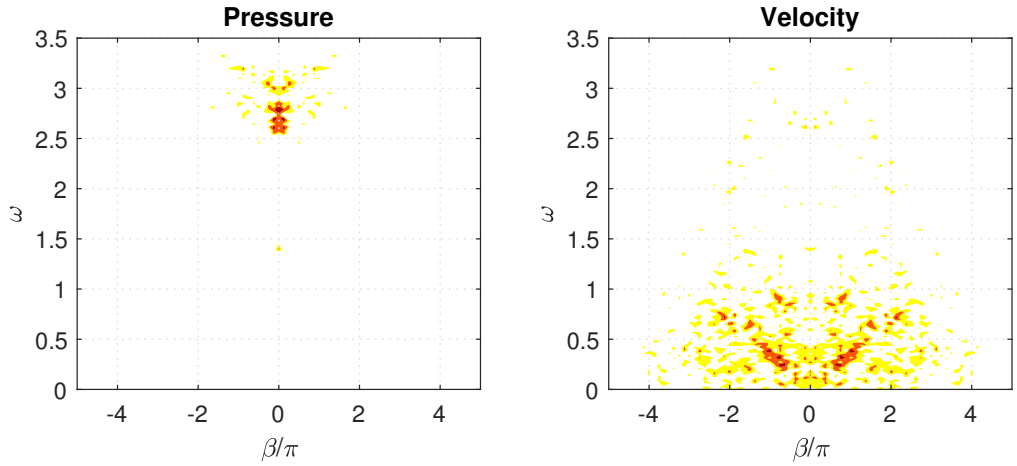

Figure 5.22 – Temporal and span-wise spectrum for the limit cycle of `R+C 3` ($Re_D = 1500$, $D/\theta = 100$, $L/D = 2$, $Ma = 0.5$). (Left) Pressure at the cavity trailing edge (Right) Wall-normal velocity inside the cavity.

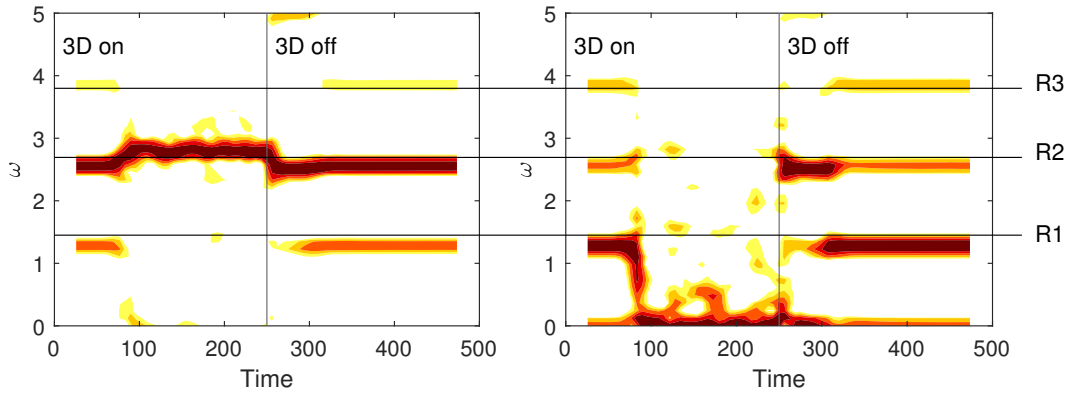

Figure 5.23 – Spectrum of (Left) pressure and (Right) velocity of case `R+C 3` ($Re_D = 1500$, $D/\theta = 100$, $L/D = 2$, $Ma = 0.5$), beginning with the 2D limit cycle, then with 3D effects turned on and off at $t = 0$ and $t = 250$, respectively. Expected frequencies for Rossiter modes are also shown.

accurate simulation is. According to figure 5.15, the maximum instability of a centrifugal mode happens at span-wise wave number $\beta = 4\pi$, which corresponds to a period length of half the cavity depth. Figure 5.24 shows the spectrum as a function of time for various span-wise wave numbers. In the figure, L_z corresponds to the period length of the most unstable centrifugal mode. The second frame, which corresponds to a domain that is too narrow for this mode, shows results very similar to those of the 2D case. The third frame, when the domain length is enough for just one period of this mode shows results that are already very similar to the larger domains, but still contains a considerable amplitude peak near the frequencies of the first Rossiter mode; furthermore, the peak corresponding to the second Rossiter mode is not fully formed in the velocity spectrum. The Rossiter 1 peak is only gone when the domain is large enough for four period lengths of this mode, when the

saturated flow state can be said to have become statistically independent on the span-wise domain. The last frame shows the spectrum for a domain that is 32 times the period size of the most unstable centrifugal mode, the reasoning behind such a large simulation is that we intended to use a domain that is large enough for the unstable 3D-modulated Rossiter modes to appear, so that we could check whether they would affect the flow in a significant manner; nonetheless, there are no considerable differences between this and the previous frame.

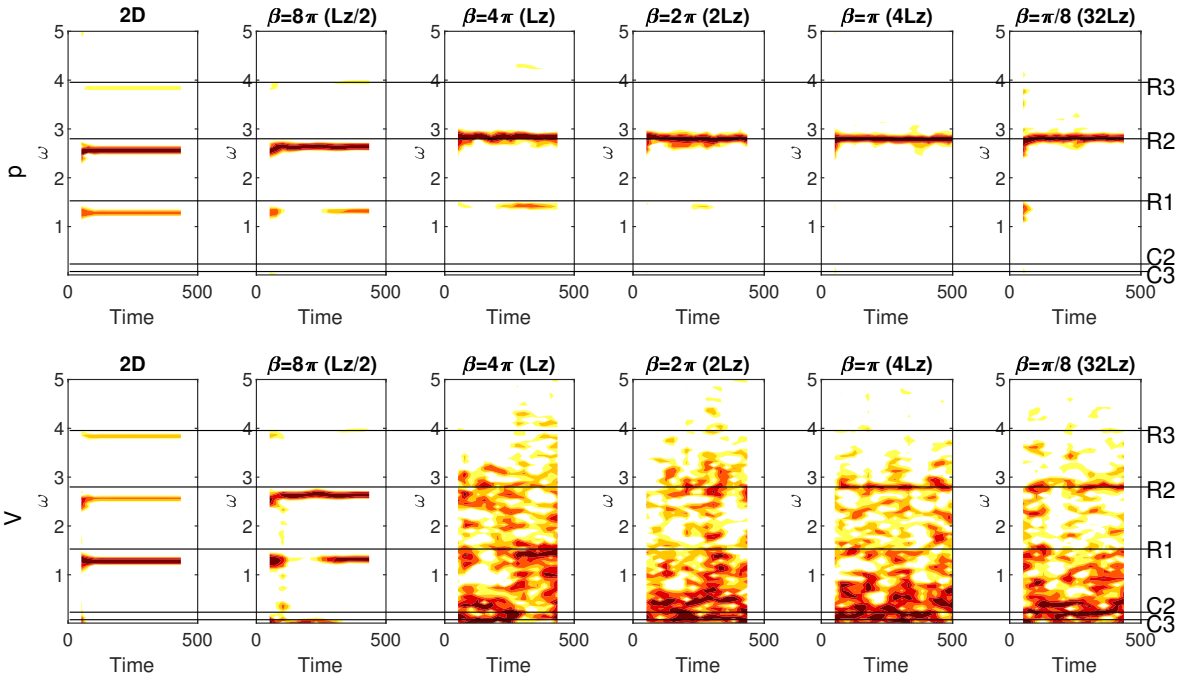

Figure 5.24 – Spectrum of (Top) pressure at the trailing edge and (Bottom) wall-normal velocity inside the cavity as a function of time for case `R+C 3` ($Re_D = 1500$, $D/\theta = 100$, $L/D = 2$, $Ma = 0.5$) for various span-wise domain lengths. Expected frequencies for Rossiter modes are also shown.

The same approach can help to further explore results from case `R+C 2`. Figure 5.25 shows a time series of wall-normal velocity inside the cavity, which is more adequate to capture centrifugal modes in the flow, as opposed to the time series of pressure shown in figure 5.11. There is a peak at $\omega = 0.25$, just below $\omega_{C2} = 0.29$, which was predicted by the linear analysis for centrifugal mode II. By looking at the spectrum as a function of time for this case, in figure 5.26, we can see that, when compared to case `R+C 3`, this time the centrifugal modes can be seen much more clearly.

The two-dimensional spectrum of case `R+C 2` is shown in figure 5.27. It is much clearer than that of case `R+C 3`. This time, the wall-normal velocity probes were able to capture both Rossiter and Centrifugal modes. The largest peak is at $\beta = 0$ and $\omega = 2.7$, corresponding to the second Rossiter mode. The lower frequency peaks, at $\beta = 2\pi$ correspond to centrifugal mode II.

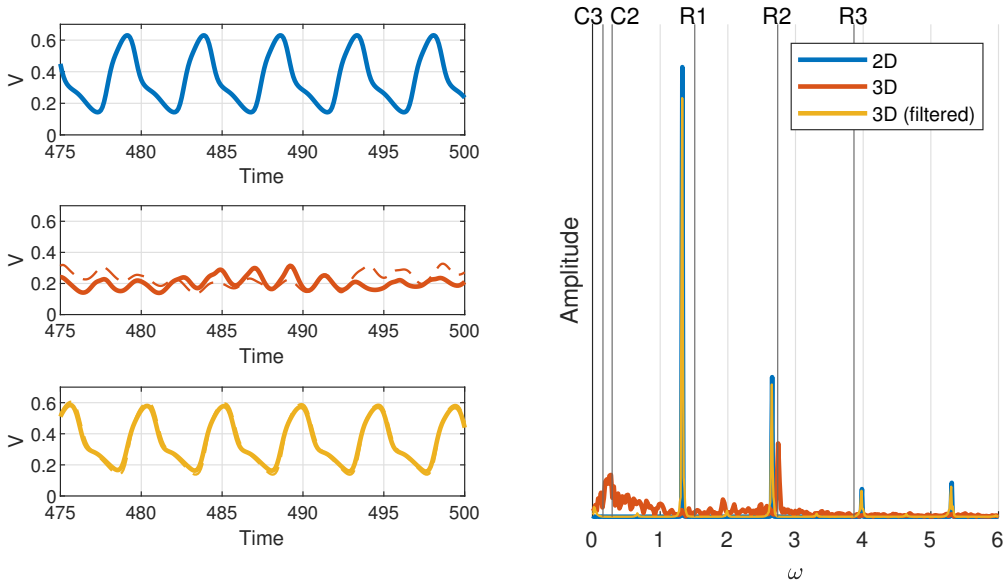

Figure 5.25 – Comparison between 2D and 3D simulations of case `R+C 2` ($Re_D = 1000$, $D/\theta = 100$, $L/D = 2$, $Ma = 0.5$). (Left) Time series of wall-normal velocity inside the cavity. The dashed lines were measured at another span-wise position. (Right) Spectrum. The vertical lines mark angular velocities predicted by the linear stability analysis for each Rossiter mode (R1 through R3) and centrifugal mode (C2 and C3).

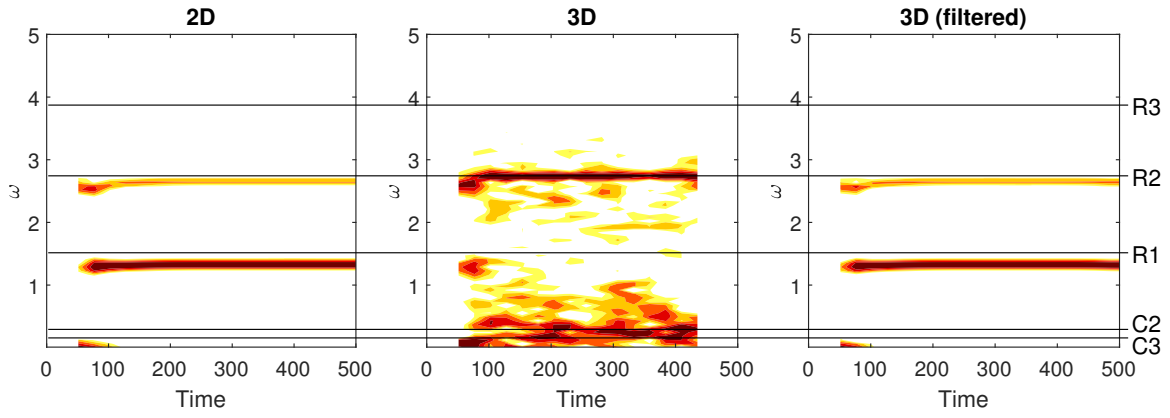

Figure 5.26 – Spectrum of wall-normal velocity inside the cavity as a function of time for case `R+C 2` ($Re_D = 1000$, $D/\theta = 100$, $L/D = 2$, $Ma = 0.5$) for (Left) the 2D simulation, (Center) the 3D simulation and (Right) the filtered 3D simulation. Expected frequencies for Rossiter modes are also shown.

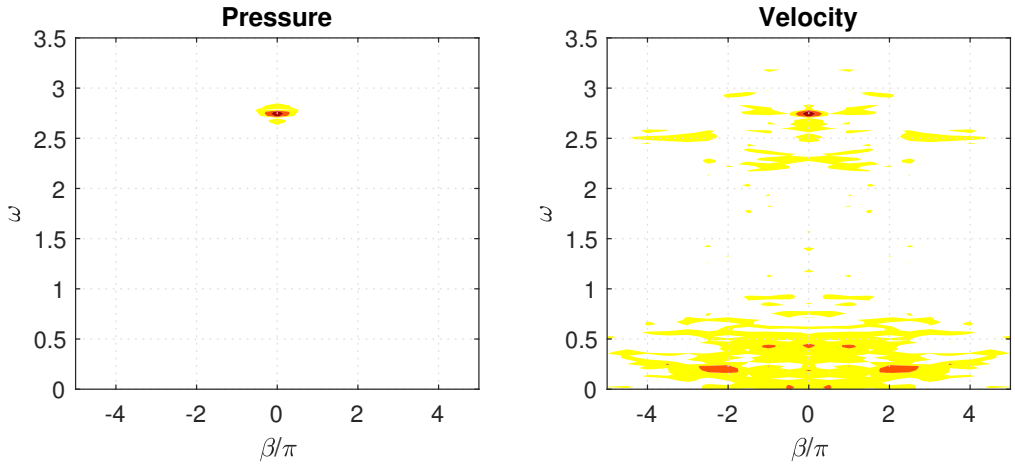

Figure 5.27 – Temporal and span-wise spectrum for the limit cycle of `R+C 2` ($Re_D = 1000$, $D/\theta = 100$, $L/D = 2$, $Ma = 0.5$). (Left) Pressure at the cavity trailing edge (Right) Wall-normal velocity inside the cavity.

5.5 Conclusion

Several parameters govern the flow in an open compressible cavity. Since we focused on Rossiter mode, we set the ratio L/D to 2 to avoid the wake modes that happen at large values of L/D. Our literature review shows that the incoming boundary layer thickness, defined here by D/θ, is often overlooked; only Yamouni, Sipp and Jacquin (2013) shows results for a sweep of this parameter, yet only briefly and used to select one D/θ to be used in their subsequent study. Here, we focus on near-critical conditions, where the global stability analysis is expected to be more meaningful, this also differs from Yamouni, Sipp and Jacquin (2013), who also used 2D LST but investigated very unstable conditions. Our analysis confirmed that the flow stabilizes as D/θ decreases, as expected from the instability of the mixing layer and noted by Yamouni, Sipp and Jacquin (2013). However, we went further to show that the Rossiter mode selection and its hierarchy are governed by the instability of the mixing layer. This was demonstrated by comparing the results of global instability with the results of linear spatial stability of the mixing layer. This explains why thicker mixing layers favor Rossiter modes of lower order, which display lower frequencies. Sarohia (1977) also investigated the possibility that the mixing layer controlled the frequency of the Rossiter mode. But their local analysis results were compared with nonlinear experiments. As will be seen here, this comparison can be misleading.

The analysis revealed that there were essentially two scenarios, one at low and another at high D/θ ratios. We chose a representative D/θ for each scenario and performed a Mach number sweep between 0.1 and 0.9. Yamouni, Sipp and Jacquin (2013) noticed an irregular effect of Mach and argued that this effect was due to the stabilizing effect of Mach number on the mixing layer competing with the destabilizing effect of resonances between Rossiter modes and standing acoustic wave modes. Their scenario corresponded more closely with that of large D/θ. In our work, we demonstrated another effect, which causes the Mach number to have a strong destabilizing effect at the low subsonic range: the increased acoustic emission at higher Mach numbers, which increase the efficiency of the feedback mechanism of Rossiter modes. In this study, we found that the energy transfer increases by about Ma^3 (see also (MATHIAS; MEDEIROS, 2021b)), consistent the cavity noise emission models that apply to this scenario (HOWE, 2004).

The three-dimensional linear stability results revealed two types of unstable three-dimensional modes: span-wise modulated Rossiter modes and centrifugal modes. Despite being essentially two-dimensional, Rossiter modes may also be unstable is slightly modulated in the span-wise direction. On the other hand, centrifugal modes reach their peak instability in smaller wave lengths.

Our non-linear simulations showed that both Rossiter and centrifugal modes may happen at the same time and interact, despite Rossiter modes being much more linearly

unstable and having much higher frequencies than centrifugal modes, under the flow conditions here studied. Under many circumstances, centrifugal modes are very small and difficult to identify but play a vital role in defining the resulting Rossiter modes and their frequencies. In both scenarios we tested in 2D and 3D (namely cases `R+C 2` and `R+C 3`), the 3D simulation remained closer to the predictions given by the linear stability analysis. By closer to the linear prediction, we mean that the dominant mode in the nonlinear simulation was the same as the linearly most unstable. It is interesting to observe that while the 2D mode is much more unstable, the 2D simulation fails to capture even the most elementary features of the flow, for example, the frequency of the oscillation.

A special 3D simulation was also prepared in which centrifugal modes were numerically filtered. This simulation resulted in a flow that is closer to the 2D simulations as opposed to the 3D ones; therefore, we could confirm that the centrifugal modes play an important role in selecting the dominant Rossiter mode. It was also shown that, in comparison with the 2D and the filtered case, the mean flow of the unfiltered 3D simulation was closer to the the base flow, which may partially explain the observation. Yet, LST predicts multiple unstable Rossiter modes (from R1 to R3) and with different dominant mode depending on the flow parameters. However, in the parameter space investigated, the 3D simulations always showed a dominant R2 mode.

Chapter 6

Effects of Gaps on Boundary Layer Transition

6.1 Introduction

We define a gap as a subset of open cavities in which its dimensions are of the same order of magnitude as the boundary layer thickness. In chapter 5, the open cavities were much larger than the boundary layer and ended up dominating the dynamics of the flow. In this chapter, cavities are much smaller and now represent small imperfections on a surface; therefore, we intend to understand the interaction between phenomena in the boundary layer with those of the gap (MATHIAS; MEDEIROS, 2019b; MATHIAS; MEDEIROS, 2021a). Moreover, due to the reduced D/θ ratio of gaps, we expect them to be more globally stable when compared to large cavities.

6.2 Mesh and domain independence

The mesh used in this chapter follows the guidelines presented in section 3.4. For $Re_{\delta_0^*} = 600$, $L = 10$, $D = 5$, $Ma = 0.5$, it contains 450 by 156 nodes in the stream-wise and wall-normal directions, respectively. The minimum spacing is $0.08\delta^*$ in both directions. The mesh is shown in figure 6.1. The top part shows the node spacing for stream-wise (left) and wall-normal (right) directions. The bottom part shows the relative spacing variation from one node to the next. The two valleys in X spacing at the top left figure correspond to the gap's leading and trailing edge.

Similarly to chapter 5, a 6th order spectral-like spatial differentiation is chosen for these simulations, while the time integration is done by the classical 4th order Runge-Kutta

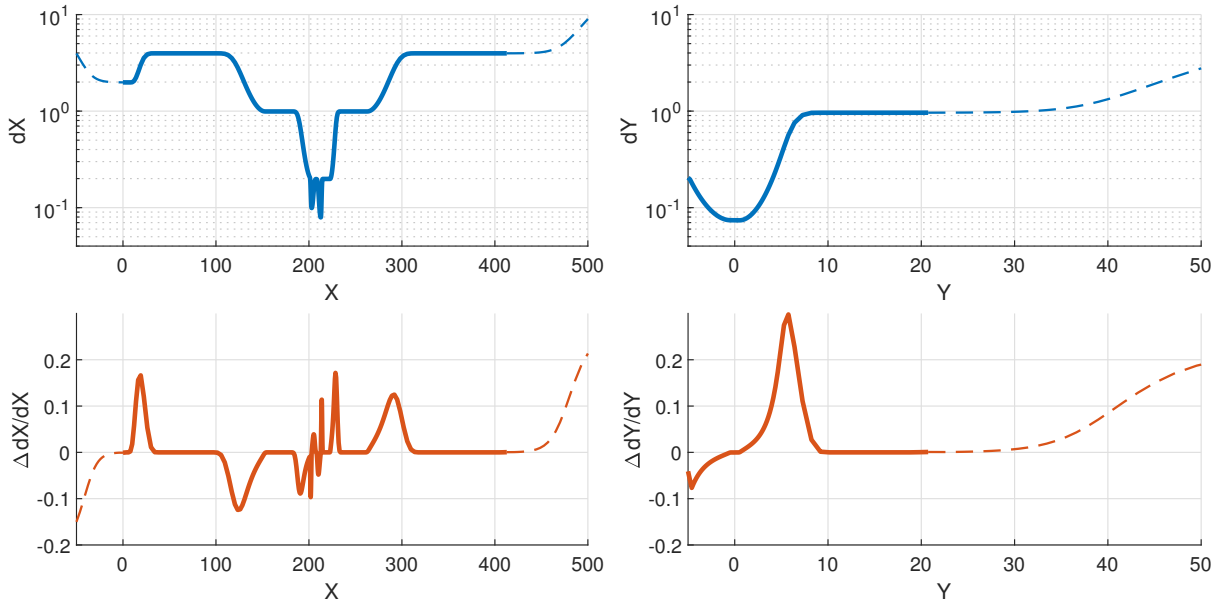

Figure 6.1 – Mesh for the gap simulation with $Re_{\delta_0^*} = 600$, $L/\delta_0^* = 10$, $D/\delta_0^* = 5$, $Ma = 0.5$.

scheme. The anti-aliasing filter coefficient is set to $\alpha = 0.49$ and it is turned off close to the open boundaries, while reduced order schemes, with smaller stencils, are used close to the walls.

All the base flows were obtained by using the techniques described in section 3.5. Figure 6.2 illustrates the base flow for the case mentioned above, while figure 6.3 shows the results of its global stability analysis. This is a stable case, with the first Rossiter mode close to critical stability, its eigenvalue is at $\sigma = -0.0066 \pm 0.02267$.

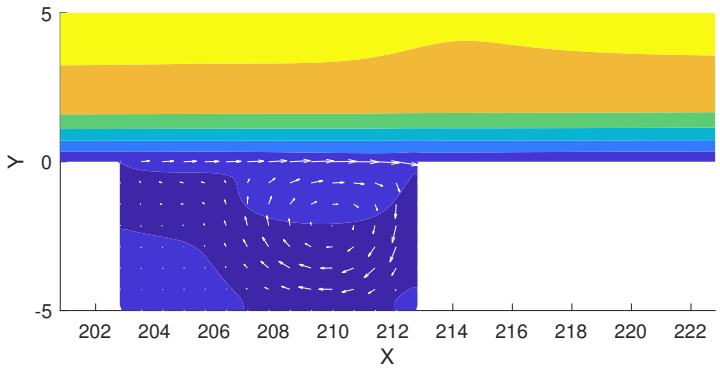

Figure 6.2 – Baseflow at the gap for $Re_{\delta_0^*} = 600$, $L/\delta_0^* = 10$, $D/\delta_0^* = 5$, $Ma = 0.5$. Each contour represents 20% of the free-flow velocity.

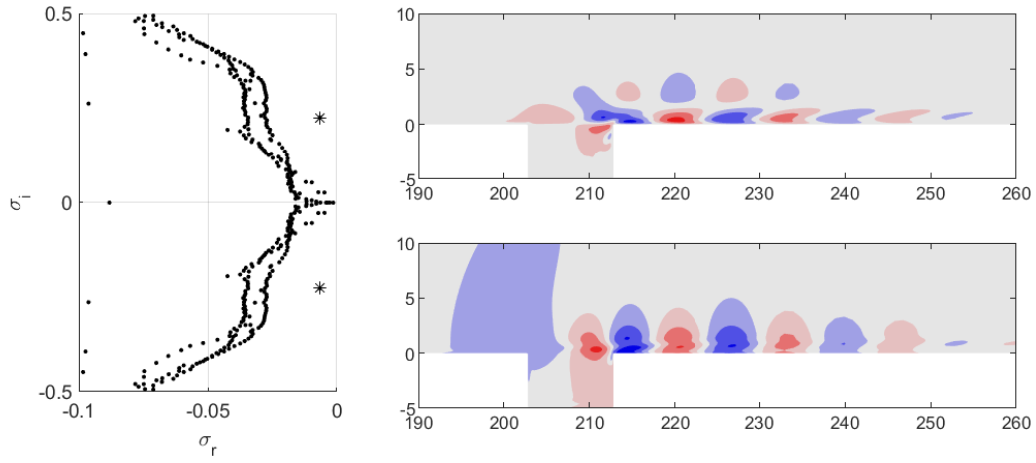

Figure 6.3 – Global stability results for $Re_{\delta_0^*} = 600$, $L/\delta_0^* = 10$, $D/\delta_0^* = 5$, $Ma = 0.5$. (Left) Eigenvalues map with the first Rossiter mode highlighted. (Right) Real part of the eigenfunctions of the first Rossiter mode: (Top) Stream-wise velocity and (Bottom) Density.

6.2.1 Mesh independence

A more refined mesh was constructed to test the solution's independence. The mesh was refined by a factor of two by adding an extra node between each pair of nodes in the original mesh, in both directions. The resulting mesh has roughly four times the number of nodes of the original, with 899×311 nodes. Figure 6.4 compares the eigenvalues of the original mesh to the refined mesh. The first Rossiter mode moves from $\sigma = -0.0066 \pm 0.02267$ to $\sigma = -0.0069 \pm 0.02269$. The difference in the real part was in the 4th decimal place, while the imaginary part has changed in the 5th decimal.

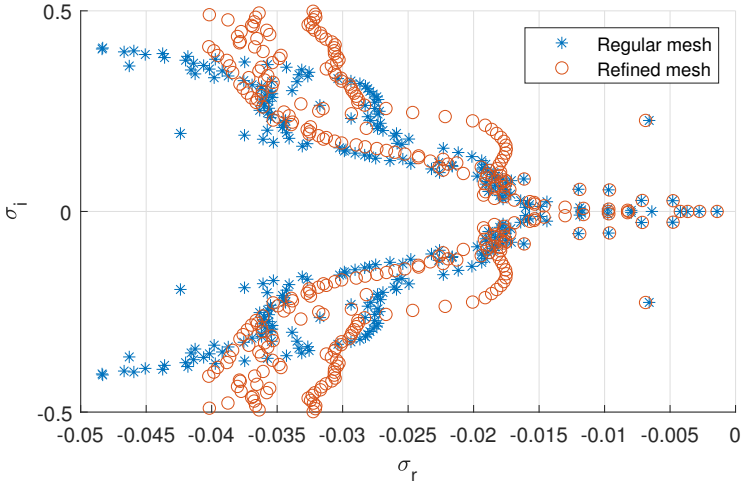

Figure 6.4 – Eigenvalues obtained with the regular mesh compared to those obtained with the refined mesh.

There is a branch of modes that appears in the results of the refined mesh in the region defined by $-0.02 \leq \sigma_r \leq -0.017$ and $0.1 \leq \sigma_i \leq 0.2$ but does not appear when the regular mesh was used. Upon closer inspection, these modes are related to the TS waves downstream from the gap. Capturing such modes is not relevant for this global instability analysis; therefore, this mesh was not required to accurately resolve them. Nonetheless, for the spatial stability analysis shown in this chapter, the mesh refinement in this area was increased according to the guidelines established in section 3.4 as these temporally stable modes may combine in such a way that forms a spatially unstable area (GASTER, 1965). Figure 6.5 exemplifies one of those modes, at $\sigma = -0.0175 \pm 0.155i$.

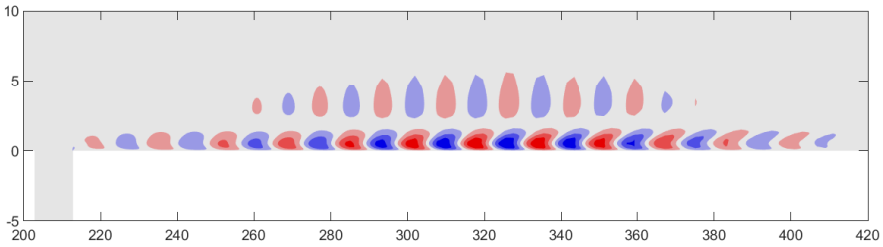

Figure 6.5 – Eigenfunction of stream-wise velocity of the mode at $\sigma = -0.0175 \pm 0.155i$.

6.2.2 Domain independence

Domain independence was tested by changing the SFD filter strength at the open boundaries. After a base flow is reached, this filter is turned on only at the buffer zones and Δ, the parameter which sets the period of the cut-off frequency, is set to infinity, with the intention of damping out all kinds of oscillations before they reach the open boundaries. χ, the parameter that sets the filter strength, must be chosen such that the filter is strong enough to damp incoming waves but not too strong as to reflect those waves. If the buffer zone is large enough, there is a range of χ that is between those two extremes that provides adequate damping for outgoing waves. Furthermore, if the physical domain is large enough, when χ is inside this adequate range, it should not affect the flow solution as well as its modes. Figure 6.6 shows the eigenvalues obtained with various values of χ.

In the range $0 \leq \chi \leq 10^{-3}$, non-physical unstable modes were retrieved by the global stability routine, they are seen in the figure at the $\sigma_r > 0$, $|\sigma_i| < 0.05$ region. The eigenfunction of those modes reveal that they are strongly related to reflections between the inlet and outlet boundaries. As χ increases, those non-physical modes are damped out and the cloud of non-physical modes moves to the left of the complex plane. At $\chi = 10^1$ and larger, the cloud of modes can be seen moving to the right of the complex plane again, indicating that the transition between physical domain and buffer zones became too sudden which causes reflections. It was not possible to run the routine with $\chi > 10^2$, as the buffer zone became too stiff and caused numerical instabilities.

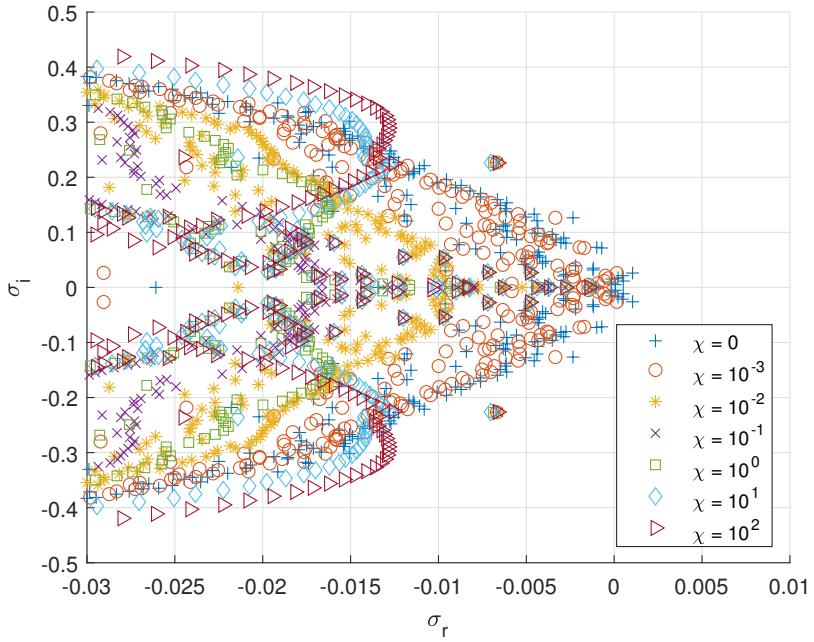

Figure 6.6 – Eigenvalues obtained with various values of χ in the SFD filter.

In the range $10^{-2} \leq \chi \leq 10^{0}$, the cloud of non-physical modes is well into the stable region, leaving only the physical modes, which are mostly unaffected by χ in this range. Therefore, we conclude that the result depends neither on the physical domain size nor on the filter strength used, as long as χ is in the range $10^{-2} \leq \chi \leq 10^{0}$. For the rest of this chapter, we use $\chi = 10^{-1}$.

6.3 Effects of the gap on the boundary layer momentum and displacement thicknesses and spatial stability

Figure 6.7 compares the boundary layer displacement (δ^*) and momentum (θ) thickness for the reference case with and without the gap, the flow parameters are $Re_{\delta_0^*} = 600$, $L = 10$, $D = 5$, $Ma = 0.5$, which correspond to $L/D = 2$, $D/\theta = 13$ and $Re_D = 3000$. The effect is mostly localized at the gap and immediately downstream, with a localized reduction of the displacement thickness and, consequently, the shape factor $H = \delta^*/\theta$. Further downstream, the effect on H is negligible and the only long-term effect of the gap is a slight downstream shift of $0.9\delta^*$ of both thickness profiles.

To measure the effect of the cavity on the spatial stability, we disturbed the flow with a wave packet, constructed in the same manner as done by Martinez and Medeiros (2016). 25 angular frequencies, linearly distributed in the range $0.02 \leq \omega \leq 0.5$ are used to build this wave packet, its amplitude being smaller than 10^{-6} to keep it in the linear

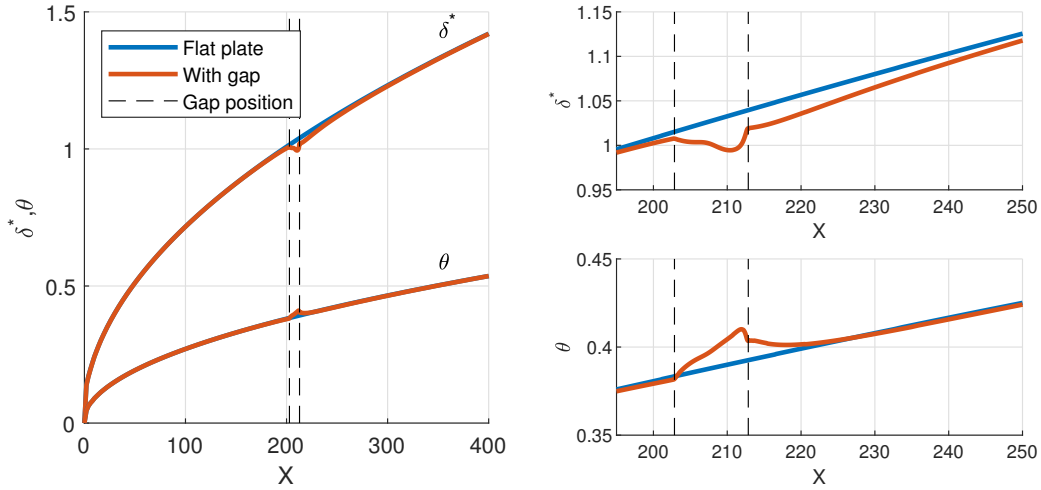

Figure 6.7 – Boundary layer displacement and momentum thickness with and without the gap for the following parameters: $Re_{\delta_0^*} = 600$, $L = 10$, $D = 5$, $Ma = 0.5$

regime.

Figure 6.8 (Left) shows the pressure at wall height at various points across the flat plate. x_c marks the gap leading edge and the distance from it is measured in terms of δ_0^*. It is possible to observe a very subtle increase in the amplitude downstream from the gap as well as a small change in phase.

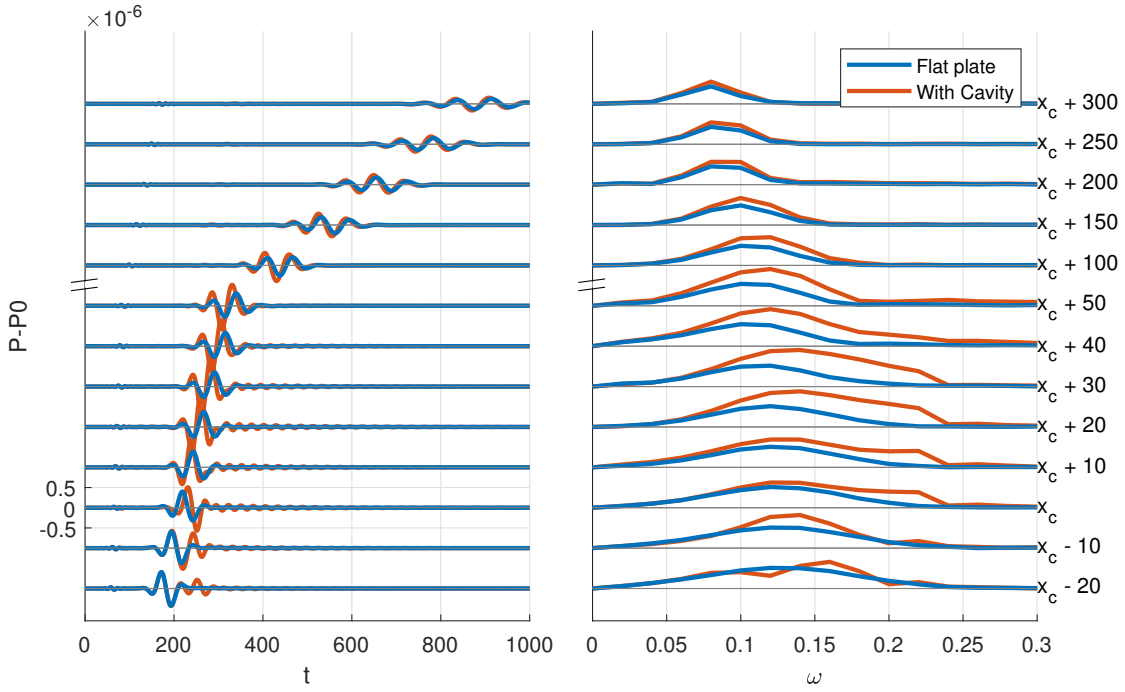

Figure 6.8 – (Left) Temporal evolution of the wave packet with and without the gap. (Right) Spectrum of the wave packet at each probe.

A spectral analysis of the wave packet at the various probes, shown in figure 6.8 (Right), revealed that, due to the spatial stability of the boundary layer, frequencies in the

range $0.05 \leq \omega \leq 0.2$ dominate the flow close to x_c, and that the gap has impacted mostly the higher end of this range. It is also possible to see that immediately downstream of the gap, there is a secondary peak at $\omega = 0.22$, which matches the least stable Rossiter mode revealed by the global stability analysis that will be shown in section 6.4. However, this secondary peak is quickly damped out due to being in the spatially stable range. Looking back at figure 6.8 (Left), the probes that are close to the gap keep showing high-frequency oscillations after the wave packet has passed. In the two probes that are placed upstream from the gap, we can also observe the wave packet was partially reflected by it, these probes also show the acoustic emission of the Rossiter modes, explaining the slight peak at $\omega = 0.22$ in their spectra. In the long-term, at $x_c + 300$, the dominant frequency was $\omega = 0.08$, at which the amplitude of the wave packet was 25% larger when the gap was present.

After the wave packet passed, the gap kept oscillating at the frequency of Rossiter mode 1, which was deemed the most unstable by the global stability analysis. Figure 6.9 shows filled contours of density (Top) and stream-wise velocity (Bottom) fluctuations at the gap. In the left-hand side, time $t = 250$ is shown, just when the wave packet is passing over the gap. In the right-hand side, $t = 500$ is shown, when the wave packet is well past the gap and the remaining oscillation can be seen. The black and white lines on the right-hand side images show positive and negative oscillations of both variables as predicted by the global stability analysis, which are remarkably similar to the oscillation that has remained in the gap after the wave packet has passed, including the acoustic emission. It is concluded that TS waves can excite modes in the gap.

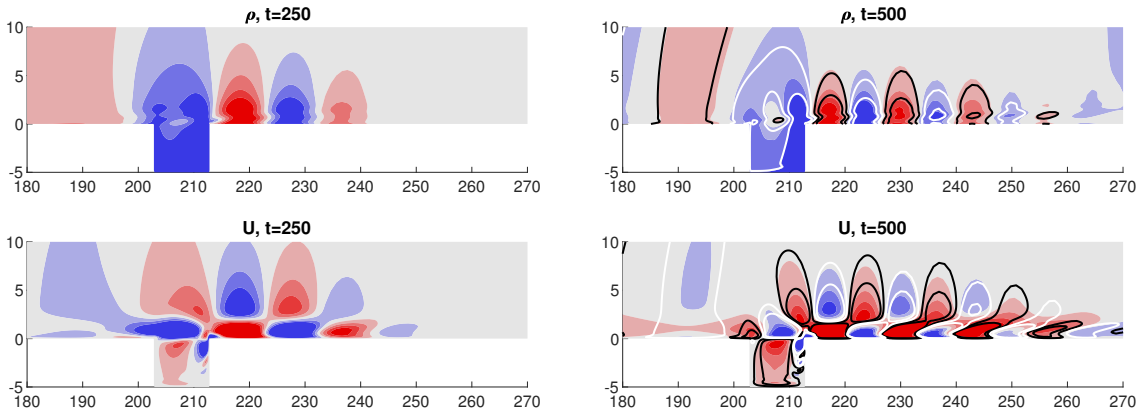

Figure 6.9 – Density (Top) and stream-wise velocity (Bottom) fluctuations at times $t = 250$ (Left) and $t = 500$ (Right). Red and blue areas represent positive and negative oscillations of the flow, respectively. Black and white lines represent the positive and negative oscillations predicted by the global stability analysis, note that the phase and levels were shifted to match the flow's.

6.4 Two-dimensional global stability

Considering the reference case above, we changed its parameters individually in order to observe the influence of each of them on the global stability. Special attention was given to the Mach number. Figure 6.10 (Left) shows the eigenvalues as the Mach number was increased from 0.3 up to 0.8 (Cases `Ma03` to `Ma08`). There is a peak in the stability at $Ma = 0.8$, similar to what was observed for larger cavities (MATHIAS; MEDEIROS, 2021b). Figure 6.10 (Right) shows the eigenvalues for variations in gap length, from 10 to 20 (Cases `L10` to `L20`). The flow becomes unstable for $L \geq 15$, when the second Rossiter mode has $\sigma_r > 0$. In chapter 5 and in (MATHIAS; MEDEIROS, 2021b), we have established that the mixing layer stability plays a very important role in selecting the most unstable Rossiter mode due to a preferred band of frequencies that has the greatest spatial amplification in the mixing layer. Another phenomenon that has a strong destabilizing effect on these modes is the resonance with standing wave modes in the gap (YAMOUNI; SIPP; JACQUIN, 2013; PLUMBLEE; GIBSON; LASSITER, 1962), also consistent with the results from large cavities.

The values of Re_{δ^*} just upstream of the gap indicate that the flow would remain laminar if not for the addition of the gap. In this scenario, increasing the values of Re_{δ^*}, which destabilizes the boundary layer, means that the ratio D/δ^* also increases, which stabilizes the global modes of the gap. A similar comparison can be made for the Mach number, which stabilizes the boundary layer (in the subsonic range used in this study) but destabilizes the flow in the gap.

In all scenarios presented in this chapter, it is possible to observe a trend that the most unstable Rossiter modes are always in the $0.2 \leq \sigma_i \leq 0.3$ range. These angular velocities are higher than the unstable range for TS waves.

Two other scenarios were tested for their global stability. When the Reynolds number, based on δ_0^* was increased from 600 to 1000, the flow has remained stable, but by a smaller margin, as the real part of the Rossiter mode eigenvalue changed from $\sigma_r = -0.0066$ to $\sigma_r = -0.0021$. On the other hand, increasing the gap depth from 5 to 10 δ_0^* has caused this mode to become slightly unstable ($\sigma_r = 0.0017$).

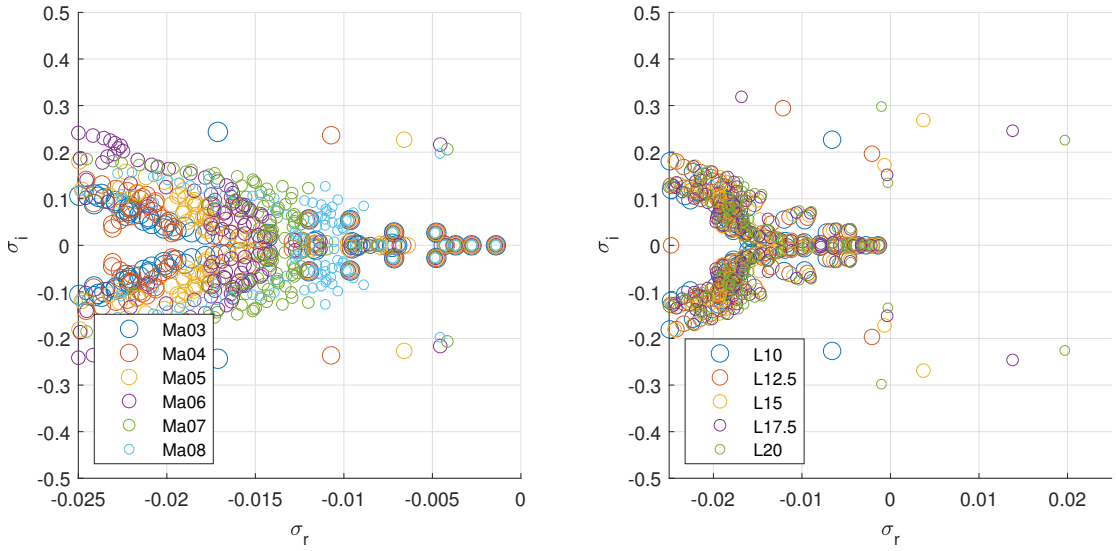

Figure 6.10 – (Left) Effect of the Mach number on the eigenmodes. (Right) Effect of gap length on the eigenmodes.

6.5 Three-dimensional global stability

Three-dimensional modes are also of concern in gaps, as they may cause oscillations that might eventually evolve into turbulence. We have used our LST routine to compute the global modes at various span-wise wave numbers ($\beta = 2\pi/L_Z$). The amplification rate of the most unstable mode at each value of β for three different Reynolds numbers is shown in figure 6.11. At $Re_{\delta^*} = 400$, the flow is stable. At $Re_{\delta^*} = 600$, the centrifugal mode II became unstable, at $\beta = 0.4\pi$. At $Re_{\delta^*} = 1000$, centrifugal mode I is also unstable. In all three cases, two-dimensional modes have remained stable.

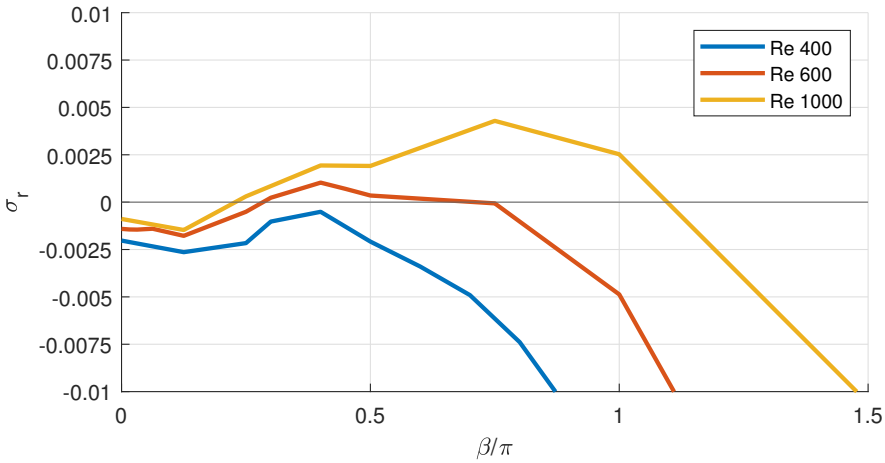

Figure 6.11 – Amplification rate of the leading mode for the parameters $L = 10$, $D = 5$, $Ma = 0.5$ and $Re_{\delta_0^*} = 400$, 600, 1000 at various span-wise wave numbers

The three types of centrifugal modes shown by Brès and Colonius (2008) can be

found in our results. At $Re_{\delta_0^*} = 1000$, $L = 10$, $D = 5$ and $Ma = 0.5$, for example, Mode I is the leading mode at $\beta = 3\pi/4$; its eigenvalue is $\sigma = -6 \times 10^{-5} \pm 0i$, which puts it very close to critical stability. At $\beta = \pi/2$, mode II leads the flow with $\sigma = 4 \times 10^{-4} \pm 0.016i$, making it slightly unstable. Mode III is leading at $\beta = \pi/4$, with $\sigma = -5 \times 10^{-4} \pm 0.007i$. The eigenfunctions of these modes are shown in figure 6.12.

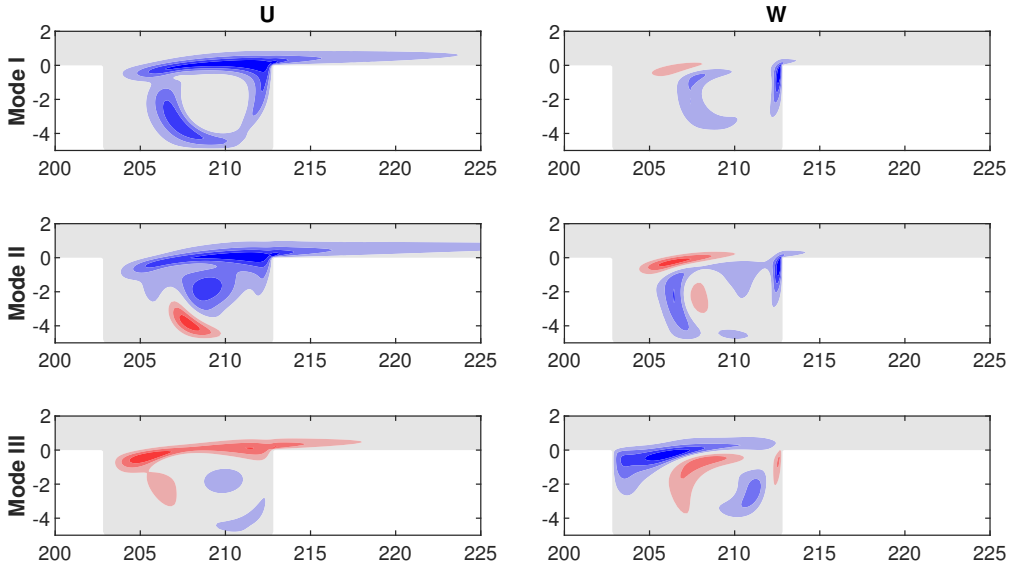

Figure 6.12 – Centrifugal modes I, II and III for $Re_{\delta_0^*} = 1000$, $L = 10$, $D = 5$ and $Ma = 0.5$. $\beta = 3/4\pi$, $\pi/2$ and $\pi/4$, respectively. (Left) Stream-wise velocity. (Right) Span-wise velocity.

We performed a sweep of gap sizes to access its impact on 2D and 3D instabilities. Reynolds number is fixed at $Re_{\delta_0^*} = 600$ and Mach number, at $Ma = 0.5$. Figure 6.13 shows the type of linear instabilities that appear for each combination of L and D. As Reynolds number based on boundary layer thickness is fixed, by increasing the ratios L/δ_0^* or D/δ_0^*, we also increase the Reynolds number based on gap length or depth, respectively. Generally, the flow becomes unstable for either $L/\delta_0^* \geq 7.5$ or $D/\delta_0^* \geq 3$. In the figure, each symbol represents that either 2D or 3D modes were found to be unstable at each point of the parametric space. The number besides the marker indicates which unstable centrifugal or Rossiter modes were found, in decreasing order of amplification rate.

Sarohia (1977) presents a similar diagram with experimental results of L and D that caused oscillations in the gap. He found that the cavity oscillates for $L\sqrt{Re_{\delta_0^*}}/\delta_0^* > 300$. In our analysis, at $Re_{\delta_0^*} = 600$, this limit corresponds to $L/\delta_0^* > 12.2$, which is approximately where both Rossiter and centrifugal modes become unstable. These results can also be compared to those of Beguet et al. (2017) and Crouch, Kosorygin and Sutanto (2020), shown in figure 2.7, in which they have found that bypass transition occurs for either $L/\delta_0^* > 18$ or $D/\delta_0^* > 2$. These figures are not directly comparable, due to different Reynolds and,

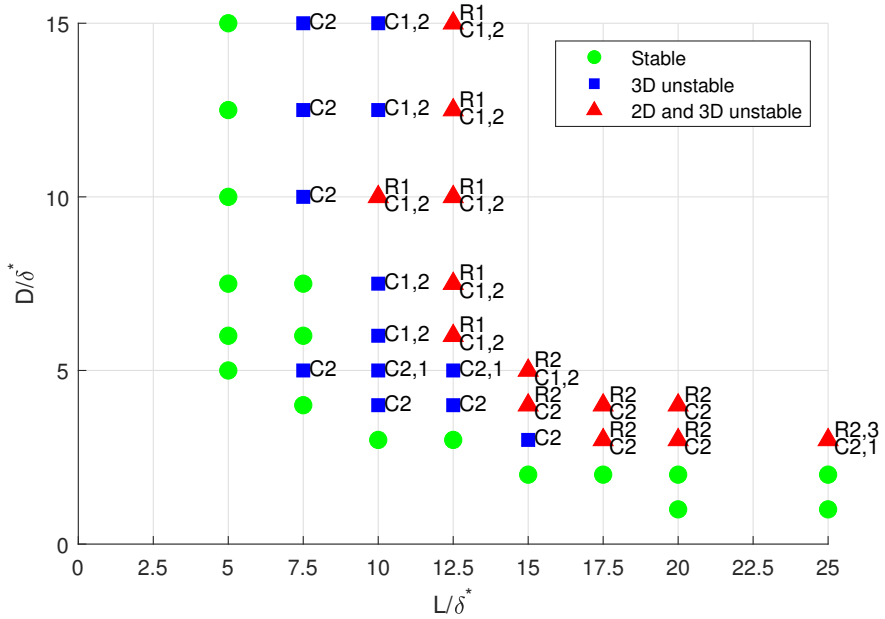

Figure 6.13 – Types of instabilities found for various combinations of gap length and depth, at $Re_{\delta_0^*} = 600$ and $Ma = 0.5$. The numbers beside the markers indicate which types of unstable centrifugal modes were found, in decreasing order of amplification rate.

especially, Mach numbers, which were much lower than 0.5 in their experiments.

By approaching the unstable region of the figure at a fixed value of D/δ_0^*, say 10, and increasing the value of L/δ_0^*, the first unstable mode that is encountered is C2. As L/δ_0^* is increased further, C1 then becomes unstable and may reach growth rates larger than those of C2. Finally, R1 becomes unstable. At much larger values of L/δ_0^*, R2 becomes the leading mode of the flow. This switch from R1 to R2 happens for the same reason we have noted in figure 6.10: The mixing layer selects modes with angular velocities in the range $0.2 \leq \omega \leq 0.3$, which corresponds to different Rossiter modes as L changes. This is due to this range of ω corresponding to vortices of a certain range of sizes, therefore, depending on the length of the cavity, different amounts of vortices will fit between the leading and the trailing edge.

On the other hand, if we fix the value of L/δ_0^*, say 20, and increase D/δ_0^*, both Rossiter and centrifugal modes become unstable at about the same value of D. The dominant Rossiter mode is dependent on the value of L, while centrifugal mode 2 was always dominant for the range of parameters we have used.

Larger gaps are usually more unstable, as can be expected by the greater Reynolds number with respect to either the gap's length or depth. One exception to this rule is the point at $L/\delta_0^* = 7.5$ and $D/\delta_0^* = 7.5$, which is stable, despite the unstable centrifugal mode found in point $L/\delta_0^* = 7.5$ and $D/\delta_0^* = 5$. The reason for this is still unclear but suggests that the ratio L/D also plays a role in this situation; nonetheless, both cases are very

close to the neutral stability. In our parametric space, no combinations of L and D were found to produce unstable 2D and stable 3D modes. However, this may not always be the case as, by increasing the Mach number, Rossiter modes destabilize, while centrifugal modes are mostly unaffected.

6.6 Direct Numerical Simulation of three-dimensional modes

As an example, we simulated the $Re_{\delta_0^*}$, $L = 10$, $D = 5$ and $Ma = 0.5$ case until the limit cycle was reached. This case has two types of unstable centrifugal mode. C2 has its peak instability at $\beta = 0.4\pi$, when $\sigma = 0.001 \pm 0.017i$; and C1 is most unstable at $\beta = 0.6$, with $\sigma = 6 \times 10^{-4} \pm 0i$. The simulation was done with a span-wise period of $L_Z = 20$, which is equivalent to $\beta = 0.1\pi$, therefore it is enough for four periods of C2 and six of C1. Figure 6.14 shows isosurfaces of stream-wise and span-wise velocity fluctuations in this case. Note that, for clarity, only a quarter of the span-wise domain is shown here. The angular velocity and span-wise wave numbers indicate that C2 was dominant in this case. The same conclusion can be reached by comparing the snapshots to the eigenmodes (see figures 6.11 and 6.12). The maximum velocity fluctuation in these snapshots was 3% of the free-stream velocity.

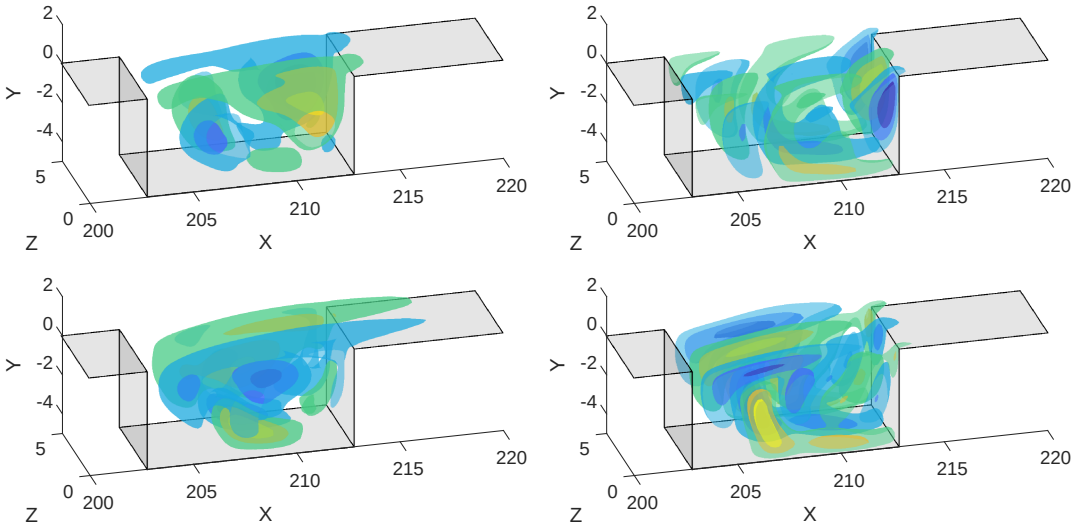

Figure 6.14 – Isosurfaces of (Left) stream-wise and (Right) span-wise velocity fluctuations at two different times (Top and Bottom) for the $Re_{\delta_0^*}$, $L = 10$, $D = 5$ and $Ma = 0.5$ case. Only a quarter of the span-wise domain is shown for clarity.

Figure 6.15 shows the time series of pressure at the trailing edge of the cavity at two different span-wise positions and the corresponding spectrum. The peak is at $\omega = 0.015$, slightly below the linearly predicted value of $\omega = 0.017$ for C2. The 2D spectrum can be seen in figure 6.16, it shows a very clear peak at $\omega = 0.015$, $\beta = 0.4\pi$, which corresponds

to C2, confirming the observations from figure 6.14. The other peaks in the spectrum are harmonics of the first peak.

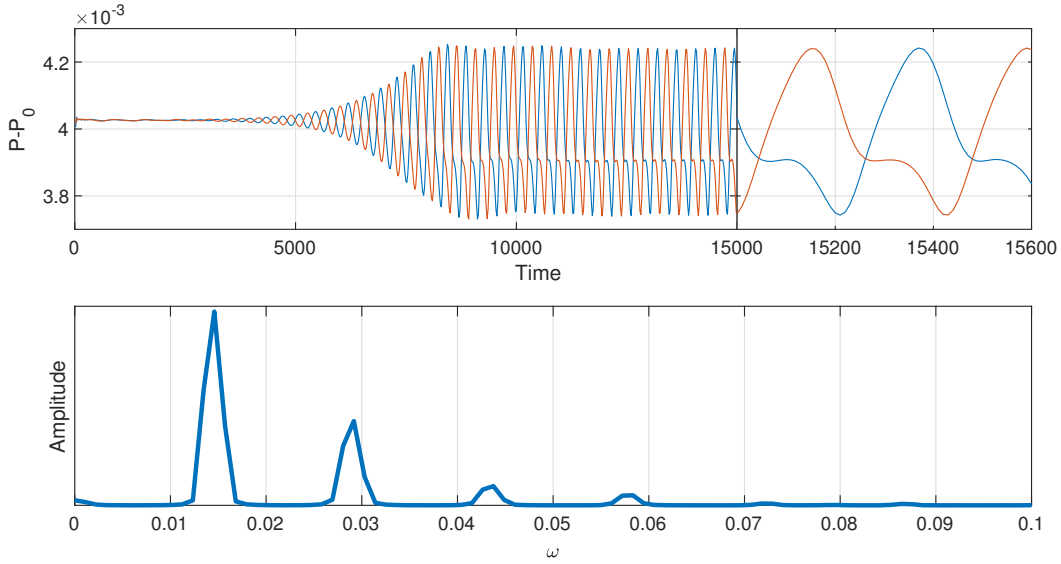

Figure 6.15 – (Top) Temporal series of pressure at the trailing edge of the gap at two different span-wise positions, at opposite phases for the $Re_{\delta_0^*}$, $L = 10$, $D = 5$ and $Ma = 0.5$ case. (Bottom) Spectrum of the limit cycle.

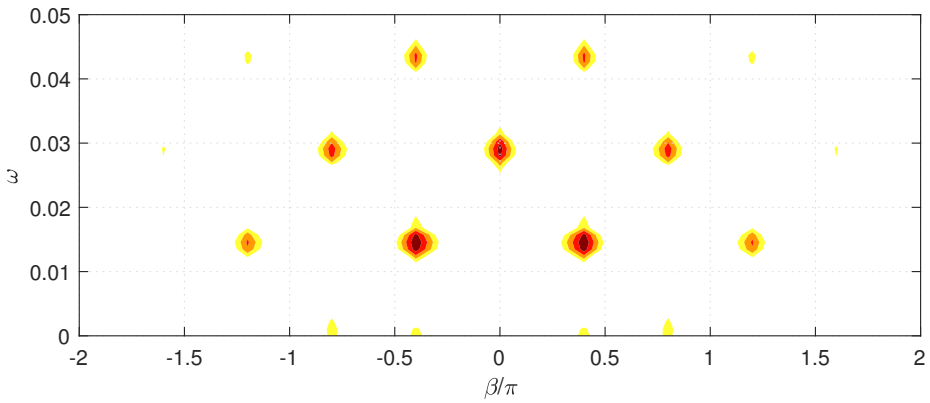

Figure 6.16 – Temporal and span-wise spectrum for the limit cycle of the $Re_{\delta_0^*}$, $L = 10$, $D = 5$ and $Ma = 0.5$ case.

In figure 6.17, we compare the boundary layer thickness of the base flow against the values obtained in the limit cycle. The yellow region represents the range of thickness values from both snapshots at all span-wise positions. The centrifugal modes had a greater effect on the displacement thickness, which, nonetheless, varied by less than 1% downstream of the gap. The mean flow, not shown in the figure, differs from the base flow by less than 0.1% after the gap.

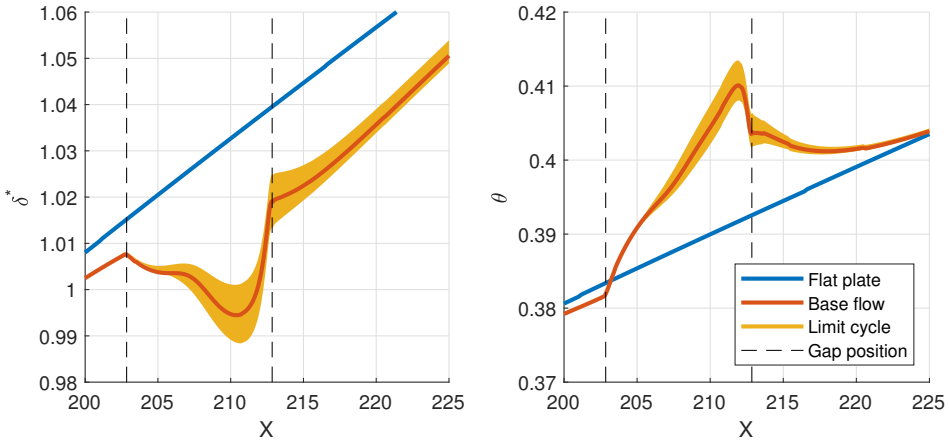

Figure 6.17 – Boundary layer displacement and momentum thickness of the base flow and of the limit cycle $Re_{\delta_0^*} = 600$, $L = 10$, $D = 5$, $Ma = 0.5$

6.7 Conclusion

We simulated gaps with various combinations of Reynolds and Mach numbers and different L/δ_0^* and D/δ_0^* ratios. If Reynolds and Mach numbers are sufficiently high, the flow becomes globally unstable and oscillates even when external disturbances cease.

In the stable cases, i.e., when no globally unstable modes are present, a static base flow was obtained, and the wave packets we have introduced in the simulation indicated that the boundary layer instability interacts with shallow cavities in a way that favors some frequencies. It is expected that the localized change in the boundary layer, shown by Worner, Rist and Wagner (2003) for small bumps, also plays a role for gaps. Another effect is the interaction with Rossiter modes, that can be excited by the passing wave packet and remain oscillating; however, if these modes are stable, they will eventually decay.

Globally unstable gaps can happen at values of Re_δ^* below critical stability for the TS waves. By moving the gap downstream, while keeping its dimensions constant, the value of Re_δ^* would increase, due to the growth of the boundary layer; however, the gap's global modes would also become more stable, due to the the stabilizing effect of decreasing L/δ_0^* and D/δ_0^* ratios. In a similar manner, decreasing the Mach number, which destabilizes the boundary layer, has the opposite effect on the gap, and causes it to become more stable.

When the flow is non-dimensionalized by the free-stream velocity and by δ_0^*, the most unstable Rossiter modes happen in the $0.2 \leq \omega \leq 0.3$ angular velocity range, which does not match the spatially unstable range of TS waves in our parametric space. Nevertheless, there may exist a flow that makes both frequency ranges overlap, increasing the potential interaction of the modes, perhaps by adding a pressure gradient or at a specific combination of Mach number and gap length. We leave this as a suggestion for

future works.

We performed a sweep of L/δ_0^* and D/δ_0^*, which indicate that there are maximum values of either parameter that keep the flow stable. Similarly, Beguet et al. (2017), Crouch, Kosorygin and Sutanto (2020) have found that there are thresholds of both L and D that when either one is crossed, the gap causes a bypass transition in the boundary layer. Further investigation is needed to determine the combination and the amplitude of modes that cause this bypass transition.

Chapter 7

Discussion and Final Remarks

In this thesis, we have implemented and used computational tools to analyze the stability characteristics of open cavities in a subsonic, compressible flow. Such geometry can be used as a simple representation of multiple types of real-world scenarios. Understanding the stability characteristics of a flow in such geometries is of fundamental importance to improve the aerodynamic performance of new aircraft or other vehicles.

7.1 Direct Numerical Simulation

Two main computational routines are used in this work: a Direct Numerical Solver (DNS) and a Linear Stability Theory routine (LST). In chapter 3, our Direct Numerical Simulation code was presented. It was based on the previous code used by the research group, but completely rewritten. Matlab® and Fortran were used to combine the strengths of each language. The preprocessing is completely done in Matlab®, which allows for great flexibility when setting up each case for simulation. The flow simulation is done by the Fortran part of the code, which is parallelized by MPI. Its modularity was always kept in mind, which allowed the code to be adapted and used by the rest of the research group in their own simulations. Compared to the previous code, the computational cost was reduced in half.

7.2 Linear Stability Analysis

In chapter 4, we show the implementation of our Linear Stability Theory routine, which is of the time-stepping type. This routine is able of computing the global stability modes of a flow without directly using its Jacobian matrix. Instead, the algorithm uses

the flow solver itself to build a reduced order approximation of the Jacobian matrix. In our literature review, there was very little in terms of guidelines for the parameters that must be chosen when setting up the method.

We developed equations to predict the effect of grid dimension, DNS noise floor, order of the Fréchet derivative approximation, disturbance magnitude, and integration time on the error. This includes the following sources of error: discretization of the solver, truncation of the Fréchet derivative approximation, and nonlinearities. We developed equations and guidelines for optimal selection of parameters and showed that they change substantially with grid size and solver accuracy. We concluded that, under optimal conditions, first order accurate Fréchet derivative approximation may be all that is needed for reasonable precision. This is particular true with open flow instability studies because the effect of different implementation of equally sound representations of a boundary condition at infinity may easily lead to variations of 10^{-3} in eigenvalue estimates (OHMICHI; SUZUKI, 2016). Moreover, optimal parameters for accuracy also lead to lowest cost for a given accuracy. Under optimal conditions, the total computational cost scales linearly with the Krylov span dimension, M; super-linear costs are negligible and progressively smaller as the grid increases, such as for three-dimensional cases. Optimal parameters for most accurate eigenvalues also lead to most accurate eigenfunctions.

7.3 Cavities

We have used our global stability code to access the instability of both Rossiter and centrifugal modes at different combinations of parameters such as incoming boundary layer thickness, free-flow Mach number and domain span-wise length. Then, we used our DNS to simulate these flows in 2 and 3 dimensions to compare the nonlinear results to linear predictions.

For 2D cavities, close to the critical conditions, increasing the ratio D/θ destabilizes the flow. We observed two scenarios, one with low and another with high D/θ ratios, which result in different Rossiter modes dominating the flow. The dominating Rossiter mode is selected by the mixing layer.

The Mach number has a, predominantly, destabilizing effect on both D/θ scenarios, which is associated to an increased acoustic emission. This destabilizing effect is more pronounced at lower Mach numbers and the amplification rates have saturated around $Ma = 0.5$ in our parametric space. Some higher-order Rossiter modes have an irregular relation with the Mach number, which is due to interaction with standing acoustic waves in the cavity.

Rossiter modes are essentially 2D and have amplification rates much higher than

centrifugal modes, which are 3D. Therefore, it would be reasonable to assume that a 2D simulation might be adequate in this scenario. Nevertheless, in general, 3D simulations may differ considerably from 2D ones. In 3D simulations, the frequency and the dominant modes tend agree better with the LST. We observed that the 2D and 3D simulations modify the base flow in different ways, resulting in distinct mixing layers, which ultimately may select different dominant modes. Still, not all modes predicted by the LST were seen, as all our simulations were dominated by a single Rossiter mode at a time.

7.4 Gaps

For gaps dimensions that can be observed on a wing, there are Rossiter and centrifugal modes that become unstable at Re_θ values that are remarkably low and still well into the laminar region of the boundary layer. They possibly cause bypass transition (there is evidence from experiments by Crouch, Kosorygin and Sutanto (2020) and simulations in the group), but the transition itself was not the scope of this study. The destabilizing effect of Mach number is also observed in gaps, with important implications, as airplanes fly at higher Mach numbers, and the current approach in industry apparently does not take that into account.

LST reveals that both Rossiter and centrifugal can be unstable in gaps. By sweeping L and D, a boundary of instability appeared and was consistent with experimental observations of transition in low-speed wind tunnels ($Ma < 0.1$). A sharp boundary of instability at $L/\delta_0^* = 7.5$ and $D/\delta_0^* = 3$ was observed in close correspondence with low-speed experiments. (SAROHIA, 1977; BEGUET et al., 2017; CROUCH; KOSORYGIN; SUTANTO, 2020)

The study showed different hierarchies of instability with different Rossiter and centrifugal modes becoming dominant. The hierarchy was very sensitive to the L/D ratio. By reaching the L/δ_0^* threshold, centrifugal modes became unstable before Rossiter modes, while at the D/δ_0^* threshold, both modes became unstable at the same time.

7.5 Suggestion for future works

Regarding the interaction of Rossiter and centrifugal modes, it is possible that the instability of the mean flow in time and span is not enough to capture all the physics, therefore analyzing the stability of Rossiter modes at different phases of the centrifugal mode cycle may improve our understanding of this phenomenon.

For more unstable flows, it is progressively more difficult to identify the centrifugal mode, but within our parameter space they play a very important role even if they are

only marginally unstable. Analysis such as a Spectral Proper Orthogonal Decomposition (SPOD) might shed a light on which modes are present when the flow is fully developed. (SCHMIDT; COLONIUS, 2020)

There are many geometric aspects of gaps that can be further explored, such as asymmetry in the leading and trailing edge heights. Moreover, by further increasing the gap length, its behavior may change, as wake modes should start to dominate the flow instead of Rossiter modes.

Finally, we also suggest that the simulation domain could be increased as to also contain the transition. This way, it would be possible to measure how much the existence of unstable Rossiter or centrifugal modes could impact the actual transition to turbulence.

Bibliography

ÅKERVIK, E. et al. Steady solutions of the Navier-Stokes equations by selective frequency damping. **Physics of Fluids**, v. 18, n. 6, p. 68–102, 2006. ISSN 10706631. Available from Internet: <http://scitation.aip.org/content/aip/journal/pof2/18/6/10.1063/1.2211705>.

ARNOLDI, W. E. The principle of minimized iterations in the solution of the matrix eigenvalue problem. **Quarterly of Applied Mathematics**, v. 9, n. 1, p. 17–29, 1951.

BAGHERI, S.; ÅKERVIK, E.; BRANDT, L.; HENNINGSON, D. S. Matrix-Free Methods for the Stability and Control of Boundary Layers. **AIAA Journal**, v. 47, n. 5, p. 1057–1068, may 2009. ISSN 0001-1452. Available from Internet: <https://arc.aiaa.org/doi/10.2514/1.41365>.

BARKLEY, D.; BLACKBURN, H. M.; SHERWIN, S. J. Direct optimal growth analysis for timesteppers. **International Journal for Numerical Methods in Fluids**, v. 57, n. 9, p. 1435–1458, jul 2008. ISSN 02712091. Available from Internet: <http://doi.wiley.com/10.1002/fld.1824>.

BEGUET, S.; PERRAUD, J.; FORTE, M.; BRAZIER, J.-P. Modeling of Transverse Gaps Effects on Boundary-Layer Transition. **Journal of Aircraft**, v. 54, n. 2, p. 794–801, 2017. ISSN 0021-8669. Available from Internet: <https://arc.aiaa.org/doi/10.2514/1.C033647>.

BERGAMO, L. F.; GENNARO, E. M.; THEOFILIS, V.; MEDEIROS, M. A. Compressible modes in a square lid-driven cavity. **Aerospace Science and Technology**, Elsevier Masson SAS, v. 44, p. 125–134, jul 2015. ISSN 12709638. Available from Internet: <https://linkinghub.elsevier.com/retrieve/pii/S1270963815001030>.

BLOCK, P. J. W. **Noise response of cavities of varying dimensions at subsonic speeds**. [S.l.], 1976. 1–36 p.

BRÈS, G. A.; COLONIUS, T. Three-dimensional instabilities in compressible flow over open cavities. **Journal of Fluid Mechanics**, v. 599, p. 309–339, mar 2008. ISSN 0022-1120. Available from Internet: <http://www.journals.cambridge.org/abstract_S0022112007009925>.

BRYNJELL-RAHKOLA, M.; SHAHRIARI, N.; SCHLATTER, P.; HANIFI, A.; HENNINGSON, D. S. Stability and sensitivity of a cross-flow-dominated Falkner–Skan–Cooke boundary layer with discrete surface roughness. **Journal of Fluid Mechanics**, v. 826, p. 830–850, sep 2017. ISSN 0022-1120. Available from Internet: <https://www.cambridge.org/core/product/identifier/S0022112017004669/type/journal_article>.

CARVALHO, A. E. B. de; MATHIAS, M. S.; MEDEIROS, M. A. F. A study on three-dimensional and isolated roughness induced transition. In: **Proceedings of the 12th ABCM Spring School on Transition and Turbulence**. Blumenau, Brazil: ABCM, 2020.

CATTAFESTA, L. N.; WILLIAMS, D. R.; ROWLEY, C. W.; ALVI, F. S. Review of Active Control of Flow-Induced Cavity Resonance. **33rd AIAA Fluid Dynamics Conference**, p. 1–20, 2003.

CHIBA, S. Global Stability Analysis of Incompressible Viscous Flow. **Journal of Japan Society of Computational Fluid Dynamics**, v. 7, n. 1, p. 20–48, 1998.

COLONIUS, T. An overview of simulation, modeling, and active control of flow/acoustic resonance in open cavities. In: **39th Aerospace Sciences Meeting and Exhibit**. Reno, NV, USA: [s.n.], 2001. p. 1 – 12. Available from Internet: <http://arc.aiaa.org/doi/abs/10.2514/6.2001-76>.

CROUCH, J.; KOSORYGIN, V.; NG, L. Modelling the Effects of Steps on Boundary-Layer Transition. In: **IUTAM Symposium on Laminar-Turbulent Transition**. Dordrecht: Kluwer Academic Publishers, 2006. p. 37–44. ISBN 978-1-4020-4159-4. Available from Internet: <http://link.springer.com/10.1007/1-4020-4159-4_4>.

CROUCH, J. D.; KOSORYGIN, V. S.; SUTANTO, M. I. Modeling Gap Effects on Transition Dominated by Tollmien-Schlichting Instability. In: **AIAA AVIATION 2020 FORUM**. Reston, Virginia: American Institute of Aeronautics and Astronautics, 2020. p. 1–8. ISBN 978-1-62410-598-2. Available from Internet: <https://arc.aiaa.org/doi/10.2514/6.2020-3075>.

CROUCH, J. D.; NG, L. L. Variable N-Factor Method for Transition Prediction in Three-Dimensional Boundary Layers. **AIAA Journal**, v. 38, n. 2, p. 211–216, feb 2000. ISSN 0001-1452. Available from Internet: <https://arc.aiaa.org/doi/10.2514/2.973>.

DAVIS, G. J.; MOLER, C. B. Sensitivity Of matrix eigenvalues. **International Journal for Numerical Methods in Engineering**, v. 12, n. 9, p. 1367–1373, 1978. ISSN 0029-5981. Available from Internet: <https://onlinelibrary.wiley.com/doi/10.1002/nme.1620120905>.

DIX, R. E.; BAUER, R. C. **Experimental and Theoretical Study of Cavity Acoustics**. [S.l.], 2000.

EAST, L. Aerodynamically induced resonance in rectangular cavities. **Journal of Sound and Vibration**, v. 3, n. 3, p. 277–287, may 1966. ISSN 0022460X. Available from Internet: <https://linkinghub.elsevier.com/retrieve/pii/0022460X66900964>.

EDWARDS, W.; TUCKERMAN, L.; FRIESNER, R.; SORENSEN, D. Krylov Methods for the Incompressible Navier-Stokes Equations. **Journal of Computational Physics**, v. 110, n. 1, p. 82–102, jan 1994. ISSN 00219991. Available from Internet: <https://linkinghub.elsevier.com/retrieve/pii/S0021999184710072>.

ERIKSSON, L. E.; RIZZI, A. Computer-aided analysis of the convergence to steady state of discrete approximations to the euler equations. **Journal of Computational Physics**, v. 57, n. 1, p. 90–128, jan 1985. ISSN 00219991. Available from Internet: <https://linkinghub.elsevier.com/retrieve/pii/0021999185900543>.

GAITONDE, D. V.; VISBAL, M. R. **High-Order Schemes for Navier-Stokes Equations: Algorithm and Implementation Into FDL3DI**. [S.l.], 1998.

GASTER, M. A note on the relation between temporally-increasing and spatially-increasing disturbances in hydrodynamic stability. **Journal of Fluid Mechanics**, v. 14, n. 2, p. 222–224, oct 1962. ISSN 0022-1120. Available from Internet: <http://www.journals.cambridge.org/abstract_S0022112062001184https://www.cambridge.org/core/product/identifier/S0022112062001184/type/journal_article>.

_____. On the generation of spatially growing waves in a boundary layer. **Journal of Fluid Mechanics**, v. 22, n. 3, p. 433–441, jul 1965. ISSN 0022-1120. Available from Internet: <https://www.cambridge.org/core/product/identifier/S0022112065000873/type/journal_article>.

_____. Understanding the Effects of Surface Roughness on the Growth of Disturbances. In: **46th AIAA Fluid Dynamics Conference**. Reston, Virginia: American Institute of Aeronautics and Astronautics, 2016. p. 3–11. ISBN 978-1-62410-436-7. Available from Internet: <http://arc.aiaa.org/doi/10.2514/6.2016-4384>.

GENNARO, E. M.; RODRÍGUEZ, D.; MEDEIROS, M. A. F.; THEOFILIS, V. Sparse Techniques in Global Flow Instability with Application to Compressible Leading-Edge Flow. **AIAA Journal**, v. 51, n. 9, p. 2295–2303, sep 2013. ISSN 0001-1452. Available from Internet: <https://arc.aiaa.org/doi/10.2514/1.J051816>.

GLOERFELT, X. **Cavity noise**. Paris: Citeseer, 2009. v. 3. 1–169 p. ISBN 9780511546143.

GOLDHIRSCH, L.; ORSZAG, S. A.; MAULIK, B. K. An efficient method for computing leading eigenvalues and eigenvectors of large asymmetric matrices. **Journal of Scientific Computing**, v. 2, n. 1, p. 33–58, mar 1987. ISSN 0885-7474. Available from Internet: <http://link.springer.com/10.1007/BF01061511>.

GOLDSTEIN, M. E. **Aeroacoustics**. [S.l.]: McGraw-Hill International Book Company, 1976. ISBN 9780070236851.

GÓMEZ, F.; GÓMEZ, R.; THEOFILIS, V. On three-dimensional global linear instability analysis of flows with standard aerodynamics codes. **Aerospace Science and Technology**, Elsevier Masson SAS, v. 32, n. 1, p. 223–234, jan 2014. ISSN 12709638. Available from Internet: <http://linkinghub.elsevier.com/retrieve/pii/S1270963813001879>.

GÓMEZ, F.; PÉREZ, J. M.; BLACKBURN, H. M.; THEOFILIS, V. On the use of matrix-free shift-invert strategies for global flow instability analysis. **Aerospace Science and Technology**, v. 44, p. 69–76, jul 2015. ISSN 12709638. Available from Internet: <http://linkinghub.elsevier.com/retrieve/pii/S1270963814002284>.

HELLER, H. H.; HOLMES, D. G.; COVERT, E. E. Flow-induced pressure oscillations in shallow cavities. **Journal of Sound and Vibration**, v. 18, n. 4, p. 545–553, 1971. ISSN 10958568.

HIMENO, F. H. T.; MATHIAS, M. S.; MEDEIROS, M. A. F. DNS of a small roughness immersed in a boundary layer: body-fitted and approximated methods comparison. In: **Proceedings of the Ibero-Latin-American Congress on Computational Methods in Engineering**. Foz do Iguaçu, Brazil: [s.n.], 2020. Available from Internet: <https://www.cilamce.com.br/arearestrita/apresentacoes/196/7756.pdf>.

HIMENO, F. H. T.; MATHIAS, M. S.; MEDEIROS, M. A. F. de. Direct Numerical Simulation of Wave Packets Over a Rough Flat Plate. In: **Proceedings of the 25th International Congress of Mechanical Engineering**. ABCM, 2019. Available from Internet: <http://abcm.org.br/anais-de-eventos/COB2019/1154>.

HOUGHTON, E. L.; CARPENTER, P. W.; COLLICOTT, S.; VALENTINE, D. **Aerodynamics for Engineering Students**. Elsevier Science, 2012. ISBN 9780080966335. Available from Internet: <https://books.google.com.br/books?id=rA6mIXaF69kC>.

HOWE, M. Mechanism of sound generation by low Mach number flow over a wall cavity. **Journal of Sound and Vibration**, v. 273, n. 1-2, p. 103–123, may 2004. ISSN 0022460X. Available from Internet: <http://linkinghub.elsevier.com/retrieve/pii/S0022460X03006448>.

HOWE, M. S. Edge, cavity and aperture tones at very low Mach numbers. **Journal of Fluid Mechanics**, v. 330, p. 61–84, jan 1997. ISSN 0022-1120. Available from Internet: <https://www.cambridge.org/core/product/identifier/S0022112096003606/type/journal_article>.

INGEN, J. L. van. A suggested semi-empirical method for the calculation of the boundary layer transition region. In: TECHNISCHE HOGESCHOOL. **Second European Aeronautical Congress, Scheveningen, Netherlands**. Delft, Nederlands, 1956.

JUNIPER, M. P.; HANIFI, A.; THEOFILIS, V. Modal Stability Theory. **Applied Mechanics Reviews**, v. 66, n. 2, p. 021004, mar 2014. ISSN 0003-6900. Available from Internet: <https://asmedigitalcollection.asme.org/appliedmechanicsreviews/article/doi/10.1115/1.4026604/395150/Modal-Stability-TheoryLecture-notes-from-the>.

KLEBANOFF, P. S.; TIDSTROM, K. D. Mechanism by Which a Two-Dimensional Roughness Element Induces Boundary-Layer Transition. **Physics of Fluids**, v. 15, n. 7, p. 1173–1188, 1972. ISSN 00319171. Available from Internet: <http://scitation.aip.org/content/aip/journal/pof1/15/7/10.1063/1.1694065>.

KNOLL, D.; KEYES, D. Jacobian-free Newton–Krylov methods: a survey of approaches and applications. **Journal of Computational Physics**, v. 193, n. 2, p. 357–397, jan 2004. ISSN 00219991. Available from Internet: <https://linkinghub.elsevier.com/retrieve/pii/S0021999103004340>.

KOLMOGOROV, A. N. **The Local Structure of Turbulence in Incompressible Viscous Fluid for Very Large Reynolds Numbers**. 1991. 9–13 p.

KOOK, H.; MONGEAU, L. Analysis of the periodic pressure fluctuations induced by flow over a cavity. **Journal of Sound and Vibration**, v. 251, n. 5, p. 823–846, apr 2002. ISSN 0022460X. Available from Internet: <http://linkinghub.elsevier.com/retrieve/pii/S0022460X01940131>.

KRISHNAMURTY, K. **Acoustic Radiation from Two-dimensional Rectangular Cutouts in Aerodynamic Surfaces**. Washington, 1956. 1 – 36 p.

LEHOUCQ, R. B.; SORENSEN, D. C. Deflation Techniques for an Implicitly Restarted Arnoldi Iteration. **SIAM Journal on Matrix Analysis and Applications**, v. 17, n. 4, p. 789–821, 1996. ISSN 0895-4798.

LELE, S. K. Compact finite difference schemes with spectral-like resolution. **Journal of Computational Physics**, v. 103, n. 1, p. 16–42, nov 1992. ISSN 00219991. Available from Internet: <https://linkinghub.elsevier.com/retrieve/pii/002199919290324R>.

LI, N.; LAIZET, S. 2DECOMP and FFT-A Highly Scalable 2D Decomposition Library and FFT Interface. **Cray User Group 2010 conference**, p. 1–13, 2010.

LIEPMANN, H. W. Investigations on Laminar Boundary-Layer Stability and Transition on Curved Boundaries. **NACA Wartime Report W107 (ACR3H30)**, n. Naca Wartime Report - W109, p. 68, 1943. Available from Internet: <http://hdl.handle.net/2060/19930093709>.

LIU, Q.; GÓMEZ, F.; THEOFILIS, V. Linear instability analysis of low- incompressible flow over a long rectangular finite-span open cavity. **Journal of Fluid Mechanics**, v. 799, p. R2, jul 2016. ISSN 0022-1120. Available from Internet: <https://www.cambridge.org/core/product/identifier/S0022112016003918/type/journal_article>.

LOISEAU, J.-C.; BUCCI, M. A.; CHERUBINI, S.; ROBINET, J.-C. **Computational Modelling of Bifurcations and Instabilities in Fluid Dynamics**. Cham: Springer International Publishing, 2019. v. 50. 33–73 p. (Computational Methods in Applied Sciences, v. 50). ISBN 978-3-319-91493-0. Available from Internet: <http://link.springer.com/10.1007/978-3-319-91494-7>.

LOISEAU, J.-C.; ROBINET, J.-C.; CHERUBINI, S.; LERICHE, E. Investigation of the roughness-induced transition: global stability analyses and direct numerical simulations. **Journal of Fluid Mechanics**, v. 760, p. 175–211, dec 2014. ISSN 0022-1120. Available from Internet: <https://www.cambridge.org/core/product/identifier/S0022112014005898/type/journal_article>.

MACK, C. J.; SCHMID, P. J. A preconditioned Krylov technique for global hydrodynamic stability analysis of large-scale compressible flows. **Journal of Computational Physics**, v. 229, n. 3, p. 541–560, feb 2010. ISSN 00219991. Available from Internet: <https://linkinghub.elsevier.com/retrieve/pii/S0021999109005117>.

MAREC, J. P. Drag Reduction: a Major Task for Research. In: THIEDE, P. (Ed.). **Aerodynamic Drag Reduction Technologies Proceedings of the CEAS/DragNet European Drag Reduction Conference**. Potsdam, Germany: Springer, 2001. p. 17–27. ISBN 354041911X. Available from Internet: <http://www.springer.com/de/book/9783540419112>.

MARTINEZ, A. **Towards natural transition in compressible boundary layers**. 2016. Tese (PhD. thesis) — University of São Paulo, 2016.

MARTINEZ, A.; MEDEIROS, M. F. Direct numerical simulation of a wavepacket in a boundary layer at Mach 0.9. In: **46th AIAA Fluid Dynamics Conference**. Reston, Virginia: American Institute of Aeronautics and Astronautics, 2016. v. 414, p. 1–33. ISBN 978-1-62410-436-7. ISSN 00221120. Available from Internet: <http://arc.aiaa.org/doi/10.2514/6.2016-3195>.

MATHIAS, M. S.; MEDEIROS, M. A. F. Direct Numerical Simulation of a Compressible Flow and Matrix-Free Analysis of its Instabilities over an Open Cavity. **Journal of Aerospace Technology and Management**, v. 10, p. 1–13, jul 2018. ISSN 2175-9146.

Available from Internet: <http://www.jatm.com.br/ojs/index.php/jatm/article/view/949>.

_____. Comparison Between Two and Three-Dimensional Direct Numerical Simulations of Rossiter Modes in Open Cavity Flow. In: **Proceedings of the 25th International Congress of Mechanical Engineering**. ABCM, 2019. Available from Internet: <http://abcm.org.br/anais-de-eventos/COB2019/0712>.

_____. Global instability analysis of a boundary layer flow over a small cavity. In: **AIAA Aviation 2019 Forum**. Reston, Virginia: American Institute of Aeronautics and Astronautics, 2019. p. 1–13. ISBN 978-1-62410-589-0. Available from Internet: <https://arc.aiaa.org/doi/10.2514/6.2019-3535>.

_____. Interaction between Rossiter and Görtler modes in the compressible flow in an open cavity. In: **AIAA AVIATION 2020 FORUM**. Reston, Virginia: American Institute of Aeronautics and Astronautics, 2020. v. 1 PartF, p. 1–6. ISBN 978-1-62410-598-2. Available from Internet: <https://arc.aiaa.org/doi/10.2514/6.2020-3074>.

_____. Spatial instability of boundary layers over small cavities and comparison to global modes. In: **AIAA AVIATION 2021 FORUM**. Reston, Virginia: American Institute of Aeronautics and Astronautics, 2021. ISBN 978-1-62410-610-1. Available from Internet: <https://arc.aiaa.org/doi/10.2514/6.2021-2931>.

_____. The effect of incoming boundary layer thickness and Mach number on linear and nonlinear Rossiter modes in open cavity flows. **Theoretical and Computational Fluid Dynamics**, may 2021. ISSN 0935-4964. Available from Internet: <https://link.springer.com/10.1007/s00162-021-00570-2>.

MCGREGOR, O. W.; WHITE, R. A. Drag of rectangular cavities in supersonic and transonic flow including the effects of cavity resonance. **AIAA Journal**, v. 8, n. 11, p. 1959–1964, nov 1970. ISSN 0001-1452. Available from Internet: <https://arc.aiaa.org/doi/10.2514/3.6032>.

MESEGUER-GARRIDO, F.; VICENTE, J. de; VALERO, E.; THEOFILIS, V. On linear instability mechanisms in incompressible open cavity flow. **Journal of Fluid Mechanics**, v. 752, p. 219–236, aug 2014. ISSN 0022-1120. Available from Internet: <https://www.cambridge.org/core/product/identifier/S0022112014002535/type/journal_article>.

MORKOVIN, M. V.; RESHOTKO, E.; HERBERT, T. Transition in open flow systems - a reassessment. **Bulletin of the American Physical Society**, v. 39:1882, 1994.

NEGI, P. S.; HANIFI, A.; HENNINGSON, D. S. On the linear global stability analysis of rigid-body motion fluid–structure-interaction problems. **Journal of Fluid Mechanics**, v. 903, p. A35, nov 2020. ISSN 0022-1120. Available from Internet: <https://www.cambridge.org/core/product/identifier/S0022112020006850/type/journal_article>.

OHMICHI, Y.; SUZUKI, K. Assessment of global linear stability analysis using a time-stepping approach for compressible flows. **International Journal for Numerical Methods in Fluids**, v. 80, n. 10, p. 614–627, apr 2016. ISSN 02712091. Available from Internet: <https://onlinelibrary.wiley.com/doi/10.1002/fld.4166>.

ORR, W. M. F. The Stability or Instability of the Steady Motions of a Perfect Liquid and of a Viscous Liquid. Part II: A Viscous Liquid. **Proceedings of the Royal Irish Academy. Section A: Mathematical and Physical Sciences**, v. 27, p. 69–138, 1909.

OWEN, T. B. **Techniques of pressure fluctuation measurements**. [S.l.], 1958. 1 – 75 p.

PAULA, I. B. de; WÜRZ, W.; MENDONÇA, M. T.; MEDEIROS, M. A. F. Interaction of instability waves and a three-dimensional roughness element in a boundary layer. **Journal of Fluid Mechanics**, v. 824, p. 624–660, aug 2017. ISSN 0022-1120. Available from Internet: <https://www.cambridge.org/core/product/identifier/S0022112017003627/type/journal_article>.

PLOGMANN, B.; WÜRZ, W.; KRÄMER, E. On the disturbance evolution downstream of a cylindrical roughness element. **Journal of Fluid Mechanics**, v. 758, p. 238–286, nov 2014. ISSN 0022-1120. Available from Internet: <https://www.cambridge.org/core/product/identifier/S0022112014004996/type/journal_article>.

PLUMBLEE, H. E.; GIBSON, J. S.; LASSITER, L. W. **Theoretical and Experimental Investigation of The Acoustic Response of Cavities In An Aerodynamic Flow**. [S.l.], 1962. 1–167 p.

PRANDTL, L. Motion of Fluids with Very Little Viscosity. In: **Internationalen Mathematiker-Kongresses**. Heidelberg: [s.n.], 1904. p. 1–8.

QADRI, U. A.; SCHMID, P. J. Frequency selection mechanisms in the flow of a laminar boundary layer over a shallow cavity. **Physical Review Fluids**, v. 2, n. 1, p. 013902, jan 2017. ISSN 2469-990X. Available from Internet: <https://link.aps.org/doi/10.1103/PhysRevFluids.2.013902>.

RAYLEIGH, J. W. S. On the stability, or instability, of certain fluid motions. **Proceedings of the London Mathematical Society**, x, p. 57–72, 1879. ISSN 0024-6115. Available from Internet: <http://onlinelibrary.wiley.com/doi/10.1112/plms/s1-11.1.57/epdf>.

RENEAUX, J. Overview on drag reduction technologies for civil transport aircraft. In: **European Congress on Computational Methods in Applied Sciences and Engineering (ECCOMAS)**. Jyväskylä: [s.n.], 2004. p. 1–18. Available from Internet: <http://echo.onera.fr/daap/reduction-trainee-civil/drag-reduction-technologies-for-civil-transport-aircraft-reneaux.pdf>.

REYNOLDS, O. An Experimental Investigation of the Circunstances Which Determine Whether the Motion of Water Shall Be Direct or Sinuous, and of the Law of Resistance in Parallel Channels. **Proceedings of the Royal Society of London**, v. 35, p. 84–99, 1883.

_____. On the Dynamical Theory of Incompressible Viscous Fluids and the Determination of the Criterion. **Proceedings of the Royal Society of London**, 1894.

ROCKWELL, D.; NAUDASHER, E. Self Sustained Oscillations of Impinging Free Shear Layers. **Ann. Rev. Fluid Mech.**, v. 11, p. 67–94, 1979.

RODRIGUES, S. B. Improving the IMEX method with a residual balanced decomposition. **eprint arXiv**, p. 1–19, may 2017. Available from Internet: <http://arxiv.org/abs/1705.04870v3>.

ROSHKO, A. **Some Measurements of Flow in a Rectangular Cavity**. [S.l.], 1955. 1 – 22 p.

ROSSITER, J. E. **Wind-tunnel experiments on the flow over rectangular cavities at subsonic and transonic speeds**. London, 1964. 1 – 36 p. Available from Internet: <http://repository.tudelft.nl/view/aereports/uuid:a38f3704-18d9-4ac8-a204-14ae03d84d8c/>.

ROWLEY, C. W.; COLONIUS, T.; BASU, A. J. On self-sustained oscillations in two-dimensional compressible flow over rectangular cavities. **Journal of Fluid Mechanics**, v. 455, p. 315–346, mar 2002. ISSN 0022-1120. Available from Internet: <https://www.cambridge.org/core/product/identifier/S0022112001007534/type/journal_article>.

ROWLEY, C. W.; WILLIAMS, D. R. Dynamics and Control of High-Reynolds-Number Flow Over Open Cavities. **Annual Review of Fluid Mechanics**, v. 38, n. 1, p. 251–276, jan 2006. ISSN 0066-4189. Available from Internet: <https://www.annualreviews.org/doi/10.1146/annurev.fluid.38.050304.092057>.

SAAD, Y. **Iterative Methods for Sparse Linear Systems**. Society for Industrial and Applied Mathematics, 2003. ISBN 978-0-89871-534-7. Available from Internet: <http://epubs.siam.org/doi/book/10.1137/1.9780898718003>.

SANTOS, P. H. R.; MATHIAS, M. S.; HIMENO, F. H. T.; MEDEIROS, M. A. F. On the receptivity of acoustic waves over localized roughness in compressible boundary layers. In: **Proceedings of the 18th Brazilian Congress of Thermal Sciences and Engineering**. [S.l.]: ABCM, 2020.

SAROHIA, V. Experimental Investigation of Oscillations in Flows Over Shallow Cavities. **AIAA Journal**, v. 15, n. 7, p. 984–991, jul 1977. ISSN 0001-1452. Available from Internet: <http://arc.aiaa.org/doi/10.2514/3.60739>.

SCHLICHTING, H. Laminare Strahlausbreitung. **Z. angew. Math. Mech.**, v. 13, p. 260–263, 1933.

SCHLICHTING, H.; GERSTEN, K. **Boundary Layer Theory**. 8th. ed. [S.l.]: Springer-Verlag Berlin Heidelberg, 2000.

SCHMIDT, O. T.; COLONIUS, T. Guide to Spectral Proper Orthogonal Decomposition. **AIAA Journal**, v. 58, n. 3, p. 1023–1033, mar 2020. ISSN 0001-1452. Available from Internet: <https://arc.aiaa.org/doi/10.2514/1.J058809>.

SCHUBAUER, G.; SKRAMSTAD, H. Laminar boundary-layer oscillations and transition on a flat plate. **Journal of Research of the National Bureau of Standards**, v. 38, n. 2, p. 251, feb 1947. ISSN 0091-0635. Available from Internet: <https://nvlpubs.nist.gov/nistpubs/jres/38/jresv38n2p251_A1b.pdf>.

SILVA, H. G.; SOUZA, L. F.; MEDEIROS, M. A. F. Verification of a mixed high-order accurate DNS code for laminar turbulent transition by the method of manufactured solutions. **International Journal for Numerical Methods in Fluids**, v. 64, n. 3, p. 336–354, sep 2010. ISSN 02712091. Available from Internet: <https://onlinelibrary.wiley.com/doi/10.1002/fld.2156>.

SIPP, D.; LEBEDEV, A. Global stability of base and mean flows: a general approach and its applications to cylinder and open cavity flows. **Journal of Fluid Mechanics**, v. 593, p. 333–358, dec 2007. ISSN 0022-1120. Available from Internet: <https://www.cambridge.org/core/product/identifier/S0022112007008907/type/journal_article>.

SOMMERFELD, A. Ein Beitrag zur hydrodynamischen Erklaerung der turbulenten Fluessigkeitsbewegungen. In: **Proceedings of the 4th International Congress of Mathematicians**. [S.l.: s.n.], 1908. p. 116–124.

SOUZA, L. F.; MENDONÇA, M. T.; MEDEIROS, M. A. F. The advantages of using high-order finite differences schemes in laminar-turbulent transition studies. **International Journal for Numerical Methods in Fluids**, v. 48, n. 5, p. 565–582, 2005. ISSN 02712091.

SUN, Y.; TAIRA, K.; CATTAFESTA, L. N.; UKEILEY, L. S. Spanwise effects on instabilities of compressible flow over a long rectangular cavity. **Theoretical and Computational Fluid Dynamics**, p. 1–11, nov 2016. ISSN 0935-4964. Available from Internet: <http://link.springer.com/10.1007/s00162-016-0412-y>.

_____. Biglobal instabilities of compressible open-cavity flows. **Journal of Fluid Mechanics**, v. 826, p. 270–301, sep 2017. ISSN 0022-1120. Available from Internet: <https://www.cambridge.org/core/product/identifier/S0022112017004165/type/journal_article>.

TAIRA, K. et al. Modal Analysis of Fluid Flows: An Overview. **AIAA Journal**, v. 55, n. 12, p. 4013–4041, dec 2017. ISSN 0001-1452. Available from Internet: <https://arc.aiaa.org/doi/10.2514/1.J056060>.

TAM, C. The acoustic modes of a two-dimensional rectangular cavity. **Journal of Sound and Vibration**, v. 49, n. 3, p. 353–364, dec 1976. ISSN 0022460X. Available from Internet: <https://linkinghub.elsevier.com/retrieve/pii/0022460X76904260>.

TEMPERTON, C. Algorithms for the solution of cyclic tridiagonal systems. **Journal of Computational Physics**, v. 19, n. 3, p. 317–323, nov 1975. ISSN 00219991. Available from Internet: <https://linkinghub.elsevier.com/retrieve/pii/0021999175900819>.

TEZUKA, A.; SUZUKI, K. Three-Dimensional Global Linear Stability Analysis of Flow Around a Spheroid. **AIAA Journal**, v. 44, n. 8, p. 1697–1708, aug 2006. ISSN 0001-1452. Available from Internet: <https://arc.aiaa.org/doi/10.2514/1.16632>.

THEOFILIS, V. Advances in global linear instability analysis of nonparallel and three-dimensional flows. **Progress in Aerospace Sciences**, v. 39, n. 4, p. 249–315, may 2003. ISSN 03760421. Available from Internet: <https://linkinghub.elsevier.com/retrieve/pii/S0376042102000301>.

_____. Global Linear Instability. **Annual Review of Fluid Mechanics**, v. 43, n. 1, p. 319–352, jan 2011. ISSN 0066-4189. Available from Internet: <https://www.annualreviews.org/doi/10.1146/annurev-fluid-122109-160705>.

THEOFILIS, V.; COLONIUS, T. An Algorithm for the Recovery of 2- and 3D BiGlobal Instabilities of Compressible Flow Over 2D Open Cavities. In: **33rd AIAA Fluid Dynamics Conference and Exhibit**. Reston, Virigina: American Institute of Aeronautics and Astronautics, 2003. ISBN 978-1-62410-095-6. Available from Internet: <https://arc.aiaa.org/doi/10.2514/6.2003-4143>.

TIETJENS, O. Beiträge zur Entstehung der Turbulenz. **Z. angew. Math. Mech.**, v. 5, p. 200–217, 1925.

TINOCO, E. N. et al. Summary Data from the Sixth AIAA CFD Drag Prediction Workshop: CRM Cases. **Journal of Aircraft**, v. 55, n. 4, p. 1352–1379, jul 2018. ISSN 0021-8669. Available from Internet: <https://arc.aiaa.org/doi/10.2514/1.C034409>.

TOLLMIEN, W. Über die Entstehung der Turbulenz. In: **Nachrichten der Gesellschaft der Wissenschaften zu Göttingen**. Göttingen: [s.n.], 1929. p. 21–44.

_____. **The production of turbulence**. Washington, 1932. v. 609.

VICENTE, J. de; BASLEY, J.; MESEGUER-GARRIDO, F.; SORIA, J.; THEOFILIS, V. Three-dimensional instabilities over a rectangular open cavity: from linear stability analysis to experimentation. **Journal of Fluid Mechanics**, v. 748, p. 189–220, 2014. ISSN 0022-1120. Available from Internet: <http://www.journals.cambridge.org/abstract_S0022112014001268>.

WANG, Y. X.; GASTER, M. Effect of surface steps on boundary layer transition. **Experiments in Fluids**, v. 39, n. 4, p. 679–686, oct 2005. ISSN 0723-4864. Available from Internet: <http://link.springer.com/10.1007/s00348-005-1011-7>.

WILLIAMS, D.; ROWLEY, C. Recent Progress in Closed-Loop Control of Cavity Tones. In: **44th AIAA Aerospace Sciences Meeting and Exhibit**. Reston, Virigina: American Institute of Aeronautics and Astronautics, 2006. ISBN 978-1-62410-039-0. Available from Internet: <https://arc.aiaa.org/doi/10.2514/6.2006-712>.

WORNER, A.; RIST, U.; WAGNER, S. Humps/Steps Influence on Stability Characteristics of Two-Dimensional Laminar Boundary Layer. **AIAA Journal**, v. 41, n. 2, p. 192–197, feb 2003. ISSN 0001-1452. Available from Internet: <https://arc.aiaa.org/doi/10.2514/2.1960>.

YAMOUNI, S.; SIPP, D.; JACQUIN, L. Interaction between feedback aeroacoustic and acoustic resonance mechanisms in a cavity flow: a global stability analysis. **Journal of Fluid Mechanics**, v. 717, p. 134–165, feb 2013. ISSN 0022-1120. Available from Internet: <https://www.cambridge.org/core/product/identifier/S0022112012005630/type/journal_article>.